DEVELOPMENT OF LOW-NOISE DIRECT-CONVERSION X-RAY AREA DETECTORS FOR PROTEIN MICROCRYSTALLOGRAPHY

A Dissertation

Presented to the Faculty of the Graduate School

of Cornell University

in Partial Fulfillment of the Requirements for the Degree of

Doctor of Philosophy

by

Katherine Sato Shanks

May 2014

DEVELOPMENT OF LOW-NOISE DIRECT-CONVERSION X-RAY AREA DETECTORS FOR PROTEIN MICROCRYSTALLOGRAPHY

Katherine Sato Shanks, Ph.D.

Cornell University 2014

Protein microcrystallography is an active field of study in the synchrotron community, due to the fact that many proteins of scientific interest produce only small, weakly-diffracting crystals. New detectors must be developed to improve data quality and facilitate new experimental protocols, such as low-flux single-shot diffraction from microcrystals. The pioneering work in microcrystallography has been done primarily with phosphor-coupled CCDs and, more recently, with photon-counting pixel array detectors. However, both technologies have drawbacks that inhibit further development of the field. Phosphor-coupled CCDs have a large point spread function and relatively low signal-to-noise ratio (on the order of 0.5-1) for single x-ray photons. Photon-counting pixel array detectors have superior noise performance, but suffer from large pixel size and detector systematics which deserve consideration.

To fill the need for a detector with small pixels and low x-ray equivalent noise, a deep-depletion CCD has been developed with 24 μm $\times$ 24 μm pixels and a point spread < 50 μm FWHM. This device is based on the direct detection of x-rays in silicon, which yields a large number of charge carriers per stopped x-ray, such that the signal from a single x-ray photon far outweighs the detector read noise. The design of this device will be described, along with characterization and initial protein crystallographic measurements.

BIOGRAPHICAL SKETCH

Katherine Shanks (née Green) was born in Ypsilanti, Michigan in 1985. She received her B.S. in physics from the University of Michigan in May 2007 and started graduate studies in physics at Cornell University the following fall.

To my family.

ACKNOWLEDGEMENTS

As an adviser, Sol has demonstrated boundless patience and good humor. I appreciate his guidance, willingness to listen, and support during times when various projects were going less-than-smoothly. Mark Tate has been a second adviser to me, as he has been for many of my predecessors. His advice and assistance have been invaluable, and his skills and intuition as a scientist are an (occasionally daunting) inspiration. Hugh Philipp has been a helpful teacher and co-worker. Thanks for vetting my ASIC and PCB designs, and for enduring the bus ride back from the SRI 2012 banquet with me.

My co-workers, past and present, in the Gruner lab are a wonderful group of people, and all of them have taught me something. Lucas Koerner was a fantastic mentor and role model during my first three years in the lab. The mantra "what would Lucas do?" has served me well in the course of this dissertation work. Chae Un Kim's perspectives on life as well as science are always intriguing and useful, and he was a great help during the protein crystallography experiments described in this work. Jeney Wierman's enthusiasm and energy are incredible. She has been a good influence both at work and in my athletic life, being responsible for getting me to sign up for my first marathon in 2012, thereby fulfilling a major life goal. Joel Weiss has been helpful from day one, and deserves recognition for his unfailingly positive attitude. Prafull Purohit and Marianne Hromalik deserve thanks for their help with FPGA design and troubleshooting. Darol Chamberlain and Marty Novak have both provided essential technical support and advice.

Professors Veit Elser and Alyssa Apsel deserve thanks for serving on my committee, and for teaching me quantum mechanics and analog circuit design, respectively. Detector development in the Gruner lab was supported by DOE

grants FG02-97ER62443 and DE-FG02-10ER46693, and by the Keck Foundation. This dissertation is based partly on research conducted at the Cornell High Energy Synchrotron Source (CHESS), which is supported by the National Science Foundation and the National Institutes of Heath/National Institute of General Medical Sciences under NSF award DMR-0936384, and using the Macromolecular Diffraction at CHESS (MacCHESS) facility, which is supported by award GM-103485 from the National Institute of General Medical Sciences, National Institutes of Health.

Many MacCHESS scientists helped me with the experiments using the STA3200 CCD at the F1 beamline. Marian Szebenyi deserves particular recognition as my primary contact, for taking care of interfacing the new detector with the beamline, and for performing the crystallographic analysis. She was instrumental in the success of the crystallography experiments. Bill Miller and Scott Smith were incredibly helpful from the technical side and are always fun and easy to work with. I also appreciate all of the CHESS operators who helped me scrounge up oscilloscopes and other equipment, sometimes in the middle of the night, all without batting an eye.

I have been privileged to work with a wide range of wonderful collaborators, on detector experiments too numerous and varied to fit into this dissertation. Adrian Mancuso and Klaus Giewekemeyer of the European XFEL have been model MMPAD users and a joy to work with. Klaus has had a particular impact on how I keep my lab notebook organized, the importance of which cannot be overstated. David Vine and Ian McNulty were very helpful and easy to work with during multiple iterations of ptychography experiments on APS beamline 2ID-B. Todd Hufnagel and his army of graduate students and post-docs are always fun to work with. Todd was the PI on first synchrotron experiment I ever

worked on, and I've appreciated his willingness to continue to put his experiments, even to a small extent, in my hands. CHESS scientists Arthur Woll, Darren Dale and Richard Gillilan have all been great to work with over the past six years.

At Ypsilanti High School, my calculus teacher Steve MacGregor and physics teacher Annette Jones played a major role in encouraging me to pursue a career in science. Many thanks are due to both of them. I had many excellent physics professors at the University of Michigan, especially Meigan Aronson, who supervised my senior thesis, and Tim McKay, who supervised my first undergraduate research project and remained a friend and mentor throughout my undergraduate career.

I thank my family for all their support and love. My dad, mom and stepdad have always enthusiastically supported my various academic, athletic, artistic and personal pursuits, and gave me the foundation needed to succeed. My grandmother Kazi passed away two years ago and would have been thrilled to see me walk at commencement with my "funny hat" in May. The memory of her encouragement and determination kept me plugging away at this dissertation through many rough patches.

Last but not least, endless thanks to my husband, Jim, for his support, love, patience, and for encouraging me to email Sol in the first place six years ago.

TABLE OF CONTENTS

LIST OF TABLES

LIST OF FIGURES

LIST OF ABBREVIATIONS

ADC	Analog-to-digital converter
ADSC	Area Detector Systems Corporation
AGIPD	Adaptive Gain Integrating Pixel Detector
APS	Advanced Photon Source
AS	Australian Synchrotron
ASG	Max Planck Advanced Study Group
ASIC	Application-specific integrated circuit
CCD	Charge-coupled device
CHESS	Cornell High Energy Synchrotron Source
CMOS	Complimentary metal-oxide-semiconductor
CNT	Carbon nanotube
CS-PAD	Cornell-SLAC PAD
CTE	Charge transfer efficiency
DQE	Detective quantum efficiency
ERL	Energy recovery linac
ESR	Edge spread response
ESRF	European Synchrotron Radiation Facility
FLASH	Free Electron Laser in Hamburg
FWHM	Full-width at half maximum
GPCR	G-protein coupled receptor
KB mirrors	Kirkpatrick Baez mirrors
LBNL	Lawrence Berkeley National Laboratory
LCLS	Linac Coherent Light Source
LSR	Line spread response
MacCHESS	Macromolecular Diffraction Facility at CHESS

MMPAD	Mixed-Mode PAD
MOS	Metal-oxide-semiconductor
PAD	Pixel array detector
PDB	Protein Data Bank
PSF	Point spread function
PTC	Photon transfer curve
SACLA	SPring-8 Angstrom Compact Free Electron Laser
SAXS	Small-angle x-ray scattering
SDD	Silicon drift detector
SLS	Swiss Light Source
SNR	signal-to-noise ratio
SPring-8	Super Photon Ring
SSRL	Stanford Synchrotron Radiation Light Source
XFEL	X-ray free electron laser

LIST OF SYMBOLS

CHAPTER 1

INTRODUCTION

Protein microcrystallography is an area of major interest in the x-ray science community. This is due to the fact that many proteins of scientific interest are difficult to crystallize and may only produce small crystals with characteristic dimension 20 μm or less, or, alternatively, large crystals that are only well-ordered over a similar range. This category includes G-protein coupled receptors (GPCRs), proteins that mediate biological processes across cell walls. GPCRs are of interest to the biological and pharmacuetical communities, as they are involved in many human diseases and are the targets for a large fraction of modern drugs [1].

While conventional x-ray crystallography has been successful in dealing with larger, well-ordered crystals (on the order of 50 μm or larger), data collection from microcrystals is extremely challenging. Instrumentation development for protein microcrystallography is an active field, with significant efforts towards the production of microbeams, background reduction techniques, radiation damage mitigation, sample handling, and data processing. With so much effort expended towards optimizing the experiment, new detectors must be developed to keep pace and record the diffraction patterns from small, weakly-diffracting crystals as faithfully as possible.

This dissertation work focuses on detector development and optimization for protein microcrystallography. Calibration of detector systematics will also be addressed in detail. The results of a prototype direct-detection charge-coupled device (CCD) with a measured point spread $\leq$ 40 μm and low x-ray equivalent noise will be presented. This device has some promising qualities

as a candidate for use in protein microcrystallography. Characterization studies presented here will lay the foundations for potential improvements to the device.

1.1 Protein crystallography

1.1.1 Interaction of x-rays with matter

The x-rays scattered from a sample carry information about the electron density of the sample. This information can be used to determine the structure of the sample ideally at the atomic level. In the experiments described here, the sample of interest is a protein molecule. A single protein molecule does not scatter x-rays strongly. The incident radiation would damage it beyond the point of usefulness before scattered signal sufficient to yield structural information could be collected by conventional methods. If the molecules are organized into an ordered crystalline array, the x-rays scattered by individual molecules add constructively under certain conditions. These rays form diffraction spots which can be recorded by a detector and used for structure determination. X-rays scattered from a crystal can be visualized as being reflected from sets of parallel planes, as illustrated in Figure 1.1. Bragg's law states that waves diffracting from planes separated by distance d interfere constructively if

$$2d \sin\theta = n\lambda \tag{1.1}$$

where θ is half the angle between the incoming and outgoing waves, λ is the x-ray wavelength and n is an integer. From this we can see that higher diffraction angles are associated with smaller values of d. To determine atomic-level struc-

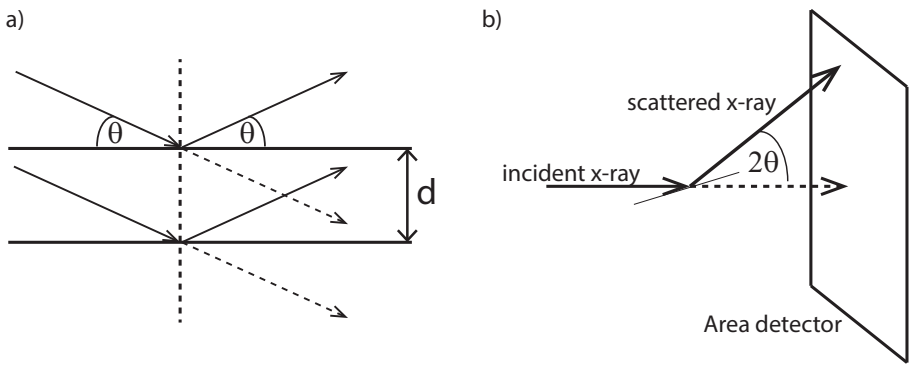

Figure 1.1: Reflection from crystal lattice planes. a) Incident rays scattering from adjacent planes at the atomic level. b) The same process shown in the context of a typical diffraction experiment.

ture it is necessary that the area detector span a sufficiently large solid angle to capture the high-resolution diffraction spots.

Diffraction spots are not infinitely sharp but have finite size determined by the incident beam size and the divergence of the scattered beam. The latter is determined by two factors: the divergence of the beam incident on the crystal, and the mosaic spread of the crystal. The divergence of the incident beam depends on the quality of the x-ray source and on the focusing technique. Current focusing techniques typically produce beam divergences in the range of <1 mrad [2]. The mosaic spread is a measure of the long-range internal disorder of the crystal. For protein crystals, mosaicity is typically around 4-9 mrad [3]. It has been proposed that in cases where large crystals suffer from high mosaicity, microcrystals may provide lower disorder and better-quality diffraction [4].

1.1.2 Conventional instrumentation and techniques

Before delving into the instrumentation and techniques being developed for microcrystallography, a few words on the instrumentation and data collection techniques used in conventional protein crystallography.

Sample preparation and handling

The canonical experiment begins with crystallization of the protein from solution. This by itself is a challenging problem that can take years of experimentation for difficult proteins. Once crystals of adequate quality are obtained, they are often cryocooled prior to data collection, which significantly reduces the rate of radiation damage. This may involve soaking the crystals in a cryo-protectant, in preparation for flash-cooling in liquid nitrogen. Alternatively, a more sophisticated cooling protocol, such as high-pressure cryocooling [5] may be used to avoid the use of a chemical cryo-protectant, which can degrade the crystal and/or data quality.

Next, the crystal is mounted in some apparatus suitable for installation on a goniometer. Frequently a flexible nylon loop is used, and the crystal is held within a droplet of liquid within the loop. Alternatively, a capillary filled with the crystallization solution may be used.

Data collection

Once mounted on the x-ray beamline, the crystal is exposed to x-rays and the resulting diffraction is recorded on an area detector. In the past, film was used,

but at present, electronic area detectors are by far the most common detector technology used in crystallography. An electronic area detector consists of an x-ray stopping medium coupled to electronics which record the signal produced by incident x-rays and reads the information out to a computer for storage. Specific area detector technologies will be described in Section 1.3.

There are two primary modes of data collection: the oscillation method, and Laue diffraction. In the Laue diffraction method, a polychromatic beam is used to probe a stationary sample. Compared to monochromatic data collection, using a polychromatic beam results in a higher flux incident on the sample, since the energy bandpass is larger. This makes Laue diffraction more suitable for time-resolved studies. Additionally, compared to monochromatic data collection, a greater number of lattice planes contribute to a single diffraction frame. Laue diffraction is therefore a promising technique for room-temperature data collection, in which crystals become radiation damaged beyond the point of usefulness after only one or a handful of frames. However, most of the work presented here will focus on monochromatic data collection using the oscillation method.

In the oscillation method the x-ray energy is fixed, with a very small bandpass (typically $\frac{d\lambda}{\lambda} = 10^{-4}$ at a synchrotron beamline), and the crystal is rotated through a user-specified angle during exposure (somewhat confusingly referred to as an "oscillation"; the crystal moves in one direction at a fixed angular velocity during exposure). 1° per oscillation is typical. Detectors with fast readout enable fine ϕ-slicing, i.e. data collection with much smaller angle per oscillation. This technique has been shown to improve structure determination, compared to data collection with larger per-oscillation angles, since the Bragg spot profiles

are effectively measured in three dimensions [6]. While fine ϕ-slicing could in principle be done with a slow-readout detector, the overhead required to accomodate the extra readout time makes this impractical.

In the oscillation method, the number of frames that must be collected depends on the angle per oscillation and on the symmetry of the crystal. For highly symmetric crystals data collection over a total oscillation angle of 90° is typical; a larger total range is required for crystals with lower symmetry. The integration time per frame is dictated by the scattering power of the crystal. Integration times of 1-30 seconds are common in coventional protein crystallography. The integration time should be long enough to collect strong signal, especially from high-resolution spots, but not so long that a significant number of spots are saturated on the detector. The threshold at which saturation occurs, called the detector full well, depends on the specific detector used.

1.1.3 The need for microcrystallography

Many proteins of scientific interest are difficult to crystallize or naturally form only microcrystals. As mentioned, GPCRs and other membrane proteins fall into this category. Other examples are virus polyhedra, large proteins that enclose and protect insect viruses [7], and amyloid fibrils, fibrous proteins that are asociated with diseases such as Alzheimer's disease [8]. In an internal study conducted at the Macromolecular Diffraction Facility at the Cornell High Energy Synchrotron Source (MacCHESS)[1], 50% of proteins screened with a standard protocol formed only microcrystals.

[1]With additional support from the Hauptman-Woodward Institute.

Protein microcrystallography has reached several milestones in the past 10 years. The structure of bovine rhodopsin, a protein involved in vision, was solved in 2004, using data collected from needle-like crystals 10 μm in diameter [9]. This was the first GPCR structure to be solved. In 2007, the first structure of a human, non-rhodopsin GPCR was solved [10]. The structure of autotaxin, an enzyme implicated in tumor growth and metastasis in mammals, was solved in 2010 using data collected from plate-like crystals only 1 μm thick [11]. However, additional work in instrumentation and data processing is needed to realize the full potential of the technique. In particular, standard x-ray detectors are not fully optimized to microcrystallographic data collection.

1.1.4 Experimental challenges for microcrystallography

Background reduction

The intensity scattered into a diffraction spot is governed by Darwin's law [3, 12]:

$$I \propto I_0 \frac{V_{xtal}}{V_{cell}^2} \tag{1.2}$$

in which I is the intensity of a diffraction spot (photon/spot), I_0 is the intensity of the incident beam (photons/s/m), V_{xtal} is the crystal volume (m^3), and V_{cell} is the unit cell volume (m^3). From this it can be seen that a small crystal with large unit cell, as is found for macromolecular proteins, diffracts weakly. The diffraction intensity will be further reduced by disorder within the crystal, and by the relatively large solvent content, which is typically about 50% for protein crystals. Background scatter must be reduced as far as possible in order not to mask the weak diffraction signal from the protein crystal.

Matching the beam size to the crystal size naturally reduces background scatter by limiting the amount of extraneous material hit by the direct beam. The production of low-divergence microbeams will be discussed below. The sample environment can be tailored to further reduce background scatter, by systematically removing potential scatterers from the path of the direct beam. Air scatter can be reduced by limiting the volume of air through which the direct beam travels; for example, by placing the beamstop very close to the sample, or through the use of vacuum or helium flight paths. Scatter from vacuum windows can be reduced by using ultrathin, low-density window materials, such as thin (100 nm) silicon nitride film. Microfabricated polyimide mounts can be used in place of nylon loops to mount small crystals [13]. These sample mounts produce low background scatter themselves compared to nylon loops, and also limit the amount of liquid surrounding the crystal. Single- or few-layer graphene has also recently shown promise as a mounting material [14].

Traditionally, crystallographers have attempted to reduce the background scatter incident on the detector by moving the detector farther away from the sample. In general, this tends to improve the signal-to-background ratio, because the background scatter falls off approximately as $\frac{1}{r^2}$ whereas the Bragg peaks may fall off more slowly (the exact scaling depends on the upstream optics and on the crystal mosaicity). Moving the detector back also reduces the solid angle spanned per pixel, thus increasing the per-pixel angular resolution. Additionally, diffraction spots separated by a small angular distance are better-separated on the detector face if the detector is far away. However, there are drawbacks to increasing the sample-to-detector distance that must be considered. The solid angle spanned by the detector is reduced, which works against the goal of collecting high-resolution data. If the diffraction spots are highly-

divergent, they will spread considerably and, if spread over too many detector pixels, could be lost within background scatter or read noise.

Low-divergence microbeams

As indicated above, microbeams are an essential tool for protein microcrystallography. Micro-focusing serves two purposes: to maximize the diffraction signal by maximizing the flux incident on the crystal, and to reduce background scatter by minimizing the flux incident on everything else. Ideally, the divergence of the microbeam should be as low as possible, to reduce the divergence of the diffraction spots and thereby increase the angular resolution of the recorded diffraction pattern. Compromises can usually be made in other parts of the experiment to deal with highly-divergent beams.

Several focusing technologies exist for creating microbeams of <20 μm diameter, including Fresnel zone plates, focusing capillaries, compound refractive lenses, and Kirkpatrick Baez (KB) mirrors. Typical spot sizes and divergences are listed for various microfocusing optics in Table 1.1, following [15]. A microfocusing optic can be used in tandem with slits in a variety of configurations to produce a microfocused beam at the sample position. A review of these techniques as they are applied to microcrystallography has recently been published [2], from which Table 1.2 has been adapted to list major synchrotron microcrystallography beamlines with beam parameters as well as the standard detectors used.

Of these techqniues, single-bounce monocapillaries deserve special attention, because they are a primary microfocusing element used at the Cornell

Microfocusing optic	Spot size (μm)	Divergence
Fresnel zone plate	0.03-30	0.1 mrad - 20°
Single-bounce monocapillary	0.25-100	1-10 mrad
Compound refractive lens	0.25-30	0.1-10 mrad
KB mirror	$\geq$ 0.09	0.1 mrad - a few degrees

Table 1.1: Typical beam size and divergence for different types of microfocusing optics.

High Energy Synchrotron Source (CHESS) and were used in the crystallgraphy experiment described in Chapter 5. CHESS has capillary optics capable of producing beams down to 1 μm in diameter, with 20 μm being more typical; however, the resultant beam has relatively high divergence, typically between 1 and 10 mrad. For comparison, divergences in the range 0.5-1.5 mrad for spot sizes down to 1 μm represent the lower limit on what is currently achievable at undulator beamlines with highly-optimized microfocusing setups [2]. Diffraction spots produced by a capillary-focused beam have a distinct profile that, due to the divergence, expands considerably by the time the diffracted spots hit the detector face.

Beamline	Beam size	Energy range	Standard detectors
APS			
23ID-B	5, 10, 20 μm	3.5 - 20 keV	Rayonix MX-300
23ID-D	5, 10, 20 μm	5-20 keV	Rayonix MX-300
17ID-B	10, 20 μm	6-20 keV	Pilatus 6M
19ID	5, 10, 20 μm	6-17 keV	ADSC Q315
24ID-E	5-20 μm	12.66 keV	ADSC Q315
31ID	20 μm	9-13.8 keV	MAR165 CCD
AS			
MX2	10 μm	5.5-28 keV	ADSC Q315r
CHESS			
A1	$<$ 20 μm	12.68 keV	ADSC Q210
F1	$<$ 20 μm	13.5 keV	ADSC Q270
F2	$<$ 20 μm	7-16 keV	PILATUS 100K
Diamond			
I02	20 μm	5-25 keV	PILATUS 6M
I03	20 μm	5-25 keV	PILATUS 6M
I04	2 μm$\times$8 μm	13.1, 7.15 keV	PILATUS 6M
I24	7-10 μm	6.5-18 keV	PILATUS 6M
ESRF			
ID13	1 μm	5-17 keV	Maxipix, MAR165
ID23-2	10 μm	14.2 keV	Rayonix MX-225
ID29	10, 20 μm	6-20 keV	PILATUS 6M
Photon Factory			
BL-17A	20 μm	5.9-13.8 keV	ADSC Q315r, Q270
BL-1A	10 μm	2.7-3.0 keV	PILATUS 2M
SPring-8			
BL32XU	1-10 μm	8.5-20 keV	Rayonix MX-225 HE
BL41XU	10 μm	6.5-35 keV	Rayonix MX-225 HE
SLS			
X06SA	15 μm$\times$5 μm	5.7-17.5 keV	PILATUS 6M
SSRL			
12-2	7, 10, 20 μm	6.7-17.2 keV	PILATUS 6M, ADSC Q315r, Rayonix MX-325

Table 1.2: Major synchrotron protein microcrystallography beamlines. APS: Advanced Photon Source, Argonne, IL, USA. AS: Australian Synchrotron, Melbourne, Australia. CHESS: Cornell High Energy Synchrotron Source, Ithaca, NY, USA. Diamond: Diamond Light Source, South Oxfordshire, UK. ESRF: European Synchrotron Radiation Facility, Grenoble, France. SPring-8: Super Photon Ring, Hyōgo Prefecture, Japan. SLS: Swiss Light Source, Villigen PSI, Switzerland. SSRL: Stanford Synchrotron Radiation Lightsource, Menlo Park, CA, USA. Beam characteristics are current as of 2012 [2]; detector listing as of May 2013.

Sample handling

Microcrystals are difficult to see and manipulate. Crystals must be located in their crystallization solution, scooped into a mounting aparatus, mounted on the beamline and aligned with the path of the x-ray beam. Once aligned, if held in a drop of liquid, they may drift out of the beam, which presumably is also small, exacerbating the problem. To combat these problems, a variety of crystal handling and visualization techniques are under development. In many cases, rather than visually aligning the crystal using an optical microscope, low-dose diffraction patterns are collected in order to locate and align the microcrystal.

The detector can aid in this process primarily by having a fast readout. A short readout time reduces the dead time during the alignment process. Low noise and high x-ray sensitivity is also beneficial, since lower dose can be used to collect the alignment diffraction patterns, avoiding unnecessary damage to the crystal.

Radiation damage

Protein crystals are highly susceptible to radiation damage. For cryocooled crystals, the damage rate is proportional only to the total dose, regardless of the dose rate [16]. As a general rule, for structure determination the total dose limit is 10 MGy per angstrom of resolution [17]. For room-temperature crystals, the damage rate does depend on the dose rate, with most studies suggesting reduced damage at high dose rates [18]. A detector with fast readout would facilitate high-dose-rate experiments by enabling rapid data collection. Again, good single-photon signal-to-noise ratio (SNR) aids in the detection of weak

diffraction spots, which could allow for data collection at lower total dose.

Solving structure from partial datasets

Many data collection schemes proposed to solve structures from protein microcrystals will require the merging of mutliple partial datasets. Merging multiple datasets has been shown to be not only feasible but in some cases beneficial [19], since diffraction spots with poor statistics in any given dataset can then be thrown out.

An extreme example of a multiple-dataset experiment is single-shot crystallography, in which each crystal yields only one diffraction frame before being damaged beyond the point of usefulness. This is expected to be the case for extremely small crystals, which will also tend to diffract very weakly. A single frame could potentially include only a handful of diffracted photons. Reconstruction of a two-dimensional image has recently been experimentally verified using a low-noise photon-integrating pixel array detector with single-pixel point spread [20]. This type of dataset requires, again, that the detector used have a fast readout, to make the collection of thousands of frames feasible, and good single-photon SNR, so that the weak, sparse signal of interest is not lost.

1.2 X-ray light sources

As of June 2013, 88% of the protein structures solved and deposited in the Protein Data Bank (PDB) were solved using data gathered via x-ray crystallography. Early work in x-ray crystallography was done using home labora-

tory sources, in which x-rays are generated by bombarding a metal target with electrons. The electrons are decelerated within the material and release braking radiation, or bremsstrahlung, along with characteristic lines of higher intensity at specific energies determined by the atomic energy levels of the target. However, the spectral brightness of such sources is limited to around 10^5 photons/s/mrad^2/mm^2/0.1% bandwidth. Synchrotron sources, and other new accelerator-based light sources, provide signficiantly higher brightness, with modern synchrotron sources approaching 10^{20} photons/s/mrad^2/mm^2/0.1% bandwidth [21]. Since the intensity of the diffracted or scattered signal is directly proportional to the incident beam intensity, brightness is an important quantity.

1.2.1 Synchrotron sources

A synchrotron source is based on a circular accelerator called a storage ring. X-rays are produced by positions or electrons (e+/e-) as they are accelerated through magnetic fields within the ring. The particles circulate the ring in bunches about 10-100 ps long and with inter-bunch separation typically on the order of 100 ns. The x-rays entering an experimental hutch therefore have an inherently pulsed time structure. In many experiments, the pulse separation is short enough that the light source is considered to be continuous. However, the pulse structure can be used to perform time-resolved experiments. For example, single-pulse Laue diffraction has been performed at the Advanced Photon Source (APS) to track the dynamics of the protein myoglobin during the uptake of carbon dioxide with 150 ps time resolution [22].

The characteristics of the x-ray beam delivered to a synchrotron beamline endstation are determined by the quality of the particle beam within the ring, the type of magnetic device used to accelerate the particle beam, and the optics used to focus the x-ray beam to the desired size, as discussed in Section 1.1.4. The particle beam can be characterized by its emittance, which goes as the product of the beam size and beam divergence. The brightness of the x-ray beam is inversely proportional to the product of the vertical and horizontal emittance. In most storage rings, the horizontal emittance is several orders of magnitude larger than the vertical emittance, owing to constraints in ring design that do not affect the latter. A low-emittance particle beam is required in order to produce the low-divergence x-ray microbeams required for many experiments, including protein microcrystallography.

The type of magnetic device used at a given beamline determines the spectral distribution of the x-ray beam, and affects its brightness and coherence. The magnetic device may be a bending magnet, a wiggler, or an undulator, shown conceptually in Figure 1.2. Bending magnets are simply dipoles which deflect the particle beam along an arc. Bending magnet radiation is incoherent, with a broad spectrum and brightness typically 10^{13} photons/s/mrad^2/mm^2/0.1% bandwidth [23]. Wigglers and undulators are periodic magnetic structures in which the particle beam is oscillated back and forth over short distances. Wigglers produce x-ray beams with brightness up to 10^{15} photons/s/mrad^2/mm^2/0.1% bandwidth [23]. Undulators have a shorter period and radiation from separate charged particles adds coherently, producing a beam that is more intense and more focused than that produced by a wiggler, up to around 10^{20} photons/s/mrad^2/mm^2/0.1% [21]. Most beamlines used for protein microcrystallography are undulator beamlines, with the exception of

the relevant CHESS beamlines (F1, F2 and A1), which have wiggler sources.

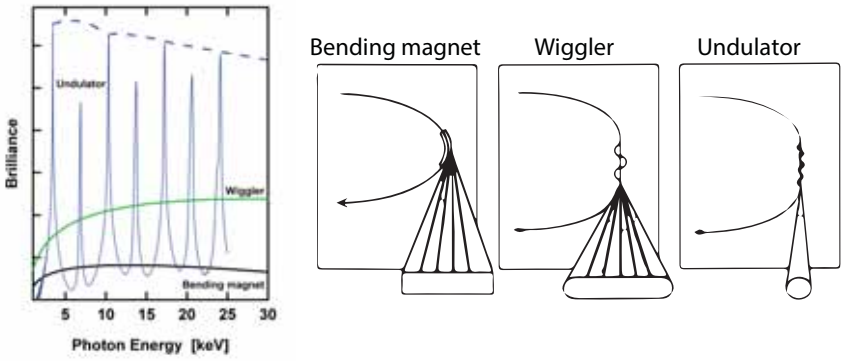

Figure 1.2: Illustration of the differences in spectral output and beam profile between bending magnets, wigglers and undulators. Adapted from images courtesy of DESY.

1.2.2 Beyond synchrotrons: emerging light sources

X-ray light source development is beginning to diversify, though upgrades to major synchrotron facilities and advances in storage ring design ensure that these sources will remain active and relevant for the near future. Two distinct light source types are currently in development: x-ray free electron lasers and energy recovery linacs.

X-ray free electron lasers

An x-ray free electron laser (XFEL) uses charge injected from a linear accelerator into a long undulator to produce coherent, high-intensity and ultra-short x-ray pulses. Typical pulse duration is about 100 fs, with 10^{12} photons per pulse,

giving an instantenous flux of 10^{25} photons/s per pulse. The extremely short, intense pulses allow the experimenter to collect the diffraction pattern from a sample before radiation damage has time to occur. This could enable data collection from small crystals and biological samples too sensitive for normal data collection at a synchrotron. However, these pulses are inherently destructive to many samples, so many copies of the sample must be used to build up a dataset. Additionally, XFELs have been found to have significant timing jitter and energy uncertainty, which complicates data collection and analysis [24].

XFELs have begun commissioning and operation in the past 10 years. Currently operating sources are the Linac Coherent Light Source (LCLS) at Stanford, the Free Electron Laser in Hamburg (FLASH), and SPring-8 Angstrom Compact Free Electron Laser (SACLA) in Japan. Planned sources include the European XFEL in Hamburg, Germany, and the Los Alamos XFEL, which will specialize in x-ray energies above 50 keV. With the exception of the European XFEL, which will have a 5 MHz repetition rate, most XFELs run at repetition rates around 100-120 Hz. At present, XFELs are strong drivers of detector development, particularly in terms of frame rate and tolerance of high instantaneous flux.

Energy recovery linacs

Energy recovery linacs (ERLs) are still in the development phase, but show promise for creating bright, coherent x-ray pulses without the destructive nature or timing jitter of XFELs. In the proposed Cornell ERL, electron bunches are generated at a rate of 1.3 GHz and injected into a linear accelerator. They then travel around an accelerator ring once, producing x-rays as they pass through undulators along the way. After a single pass through the ring, each electron

bunch returns its energy to the accelerating field within the linear accelerator and is subsequently dumped.

A key feature of an ERL is that the horizontal and vertical emittances are nearly equal, and extremely small, down to about 10 pm [25], which will allow for the production of high brightness micro- and nanobeams with low divergence. After even a single pass around the ring, the emittance of each electron bunch begins to relax to a larger equilibrium value. Therefore, the single-pass design is an important factor in producing stable micro- and nanobeams. ERLs will produce x-rays with time-averaged brightness equal to that of XFELs [26], but because of the higher repetition rate, individual pulses are less intense and will not obliterate most samples. Additionally, the time structure will more closely resemble that of synchrotron sources, so that users unconcerned with the pulse structure will be able to consider the beam to be more or less continuous in time. It is possible to conceive of using the gigahertz rate pulse structure for single-pulse experiments, but this would require significant detector development [27].

1.3 Detectors

The field of protein crystallography is dominated by phosphor-coupled CCDs and, since their introduction in 2006, photon-counting pixel array detectors (PADs). Figure 1.3 plots the number of structures deposited in the PDB per year for the three major area detector manufacturers: Area Detector Systems Corporation (ADSC) and Rayonix (formerly Mar), both of which produce phosphor-coupled CCDs, and Dectris, which produces photon-counting PADs. There are

other manufacturers and other classes of detectors (such as image plates and CMOS imagers), but these three product lines dominate the field. The focus of

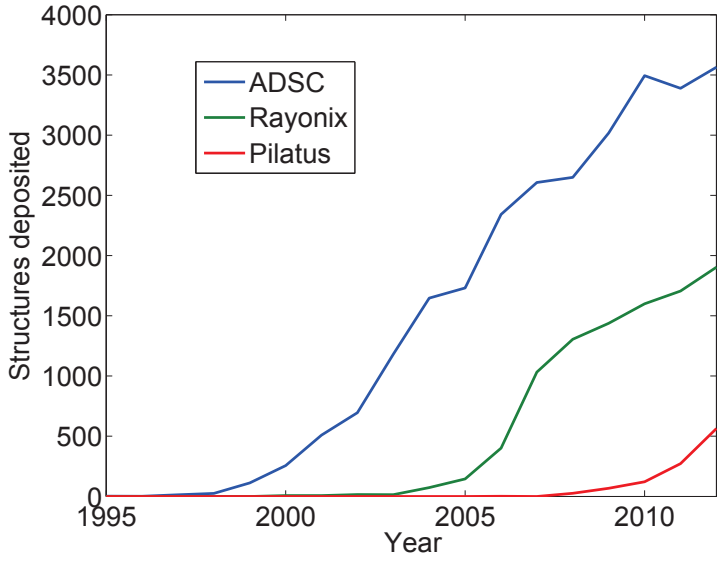

Figure 1.3: Protein Data Bank (PDB) structures deposited per year for the three major manufacturers. The Rayonix data includes detectors sold under the Mar brand, as the companies are merged.

this work is on evaluating detector technologies in terms of their suitability for protein microcrystallography. In particular, direct-detection photon-integrating detectors (both PADs and CCDs) will be addressed. Detailed architectures will be discussed in Chapter 2. For now, these detector families will be described briefly to give a sense of the state of the field.

1.3.1 Phosphor-coupled CCDs

A CCD is an electronic area detector in which photo-generated charge is collected and held in pixels, defined by localized wells of electric potential. After the exposure is finished, the photo-generated charge is transferred from pixel

to pixel towards a readout amplifier, which converts the charge into a voltage to be amplified and read out. This inherently serial readout mechanism limits the minimum read time achievable. Most phosphor-coupled CCDs require a second or more to read out, as seen in Table 1.3.

A conventional CCD is fabricated on thin silicon that does not have sufficient x-ray stopping power to serve as an efficient x-ray sensor. However, a conventional CCD can serve as an x-ray detector if the x-rays are converted into visible light. This is the principle behind a phosphor-coupled CCD. As shown in Figure

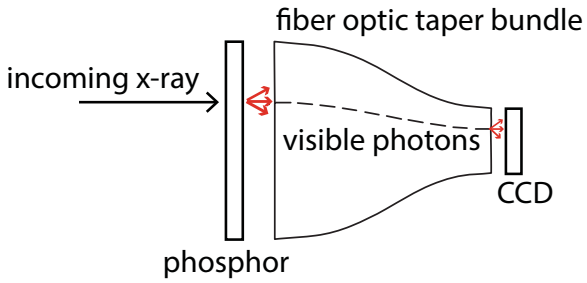

Figure 1.4: Basic phosphor-coupled CCD structure. Image courtesy of ADSC.

1.4, a settled phosphor powder is coupled via a fiber optic taper bundle to a conventional CCD. X-rays are stopped in the phosphor and converted into visible light, which is directed onto the CCD by the fiber optic taper. The read noise of conventional CCDs is very low in terms of number of electrons, with 1 electron noise being possible and 10 electrons being typical. However, the charge yield per x-ray is itself on the order to 10 electrons, so the signal-to-noise ratio for a single x-ray photon is not high - typically on the order of 1/2 to 2. The transfer of light through the phosphor and fiber optic taper also leads to inherent lateral spreading of the signal on the order of 80-100 μm.

Table 1.3 lists the specifications for phosphor-coupled CCDs used as standard detectors at the microcrystallography beamlines listed in Table 1.2.

Detector	Pixel pitch	Format	Read noise	Read time	Full well
ADSC					
Q210	51.2 μm	4096×4096	1.85 ph.†	1.10 s	27400 ph.†
Q315	51.2 μm	6144×6144	1.85 ph.†	1.10 s	27400 ph.†
Q210r	51.2 μm	4096×4096	1.53 ph.†	0.9 s	27800 ph.†
Q315r	51.2 μm	6144×6144	1.53 ph.†	0.9 s	27800 ph.†
Q270	64.8 μm	4168×4168	0.55 ph.	1.10 s	23636 ph.
Rayonix					
MX-225*	73 μm	4096×4096	1.67 ph.	1.0 s	60,000 ph.
MX-300*	73 μm	4096×4096	1.67 ph.	1.0 s	60,000 ph.
MX-325*	79 μm	4096×4096	1.67 ph.	1.0 s	60,000 ph.
MX-225 HE*	73 μm	3072×3072	0.7 ph.	1.0 s	31,800 ph.
MAR 165	40 μm	4096×4096	1.1 ph.	3.5 s	45000 ph.

Table 1.3: Summary of phosphor-coupled CCDs primarily used at microcrystallography beamlines. Quantities quoted in units of photons refer to 12 keV photons, except where marked by †, where 12.5 keV photons are used. *Specifications listed are for 2×2 pixel binning.

1.3.2 Direct-detection CCDs

With the development of thick, high-resistivity silicon, efficient direct x-ray detection in silicon has become possible in recent years. When an x-ray photon is stopped in silicon, a large number of charge carriers are generated (one electron-hole pair for every 3.6 eV deposited). Additionally, it is possible to constrain the lateral spread of the charge carriers to be less that 50 μm, offering an improvement over the spatial resolution seen in phosphor-coupled devices.

A CCD fabricated on high-resistivity silicon with high x-ray stopping power is called a direct-detection CCD. These detectors were initially developed for

infrared astronomy, and have since been adopted for x-ray use. Two representative examples of direct-detection x-ray CCD development efforts are the pn-CCD developed by the Max Planck Advanced Study Group (ASG) [28] and the 1K Frame Store CCD developed at Lawrence Berkeley National Laboratory (LBNL). The characteristics of these devices are listed in Tables 1.4 and 1.5. Both detectors were designed with a large number of readout amplifiers, to increase the maximum frame rate in both cases to 200 Hz.

Quantity	Value
Pixel pitch	75 μm
Format	1024 × 1024 and 2048 × 2048
Read noise	20 e- (low gain), 2 e- (high gain)
Read time	5 ms (for 1024 x 1024 format)
Full well	5×10^5 e- (180 10-keV x-rays)
Depletion layer thickness	450 μm

Table 1.4: Characteristics of the pn-CCD developed by the ASG for XFEL use [28].

Quantity	Value
Pixel pitch	30 μm
Format	1092 × 960 (960 × 960 in frame-store mode)
Read noise	25 e-
Read time	5 ms (for frame-store mode)
Full well	1×10^5 e- (36 10-keV x-rays)
Depletion layer thickness	200 μm

Table 1.5: Characteristics of the LBNL direct-detection 1K Frame Store CCD [29]. Full well was reported in [30].

So far, the application of direct-detection CCDs to x-ray science has been relatively limited, due to difficulty in fabrication, small active areas, and limited pixel full well. If these difficulties could be overcome, the small pixel sizes, high spatial resolution and low x-ray equivalent noise woud make them attractive x-ray detectors. Characterization of a direct-detection CCD forms a major part

of this dissertation work.

1.3.3 Photon-counting pixel array detectors

Most detector development using direct detection of x-rays in silicon has focused on hybrid pixel array detectors (PADs). These PADs are devices in which a thick silicon sensor is bonded pixel-by-pixel to a readout application-specific integrated circuit (ASIC), as shown in Figure 1.5. This parallel architecture provides a way around the serial readout bottleneck of CCDs. Depending on the

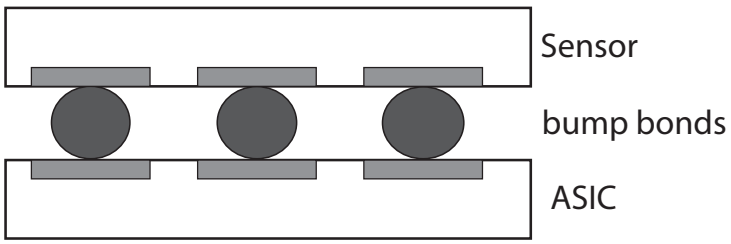

Figure 1.5: Basic pixel array detector hybrid structure (not drawn to scale). A readout ASIC is bump-bonded to a sensor, typically high-resistivity silicon.

pixel electronics, a PAD may be photon-integrating or photon-counting. At present, the only PADs that are widely available are the PILATUS family of photon-counting PADs, developed at the Swiss Light Source and sold by the spin-off company Dectris. The other major photon-counting PAD effort is the Medipix collaboration at CERN. This family of detectors includes the Maxipix PAD, which has been used in protein microcrystallography, and is distinguished from the PILATUS family by its smaller pixel size, 55 μm $\times$ 55 μm. Table 1.6 lists the specifications for photon-counting PADs used as standard detectors at the

Detector	Pixel pitch	Format	Read time	Full well
PILATUS 6M	172 μm	2463 $\times$ 2527	0.95 ms	1048575 ph.
PILATUS 2M	172 μm	1475 $\times$ 1679	0.95 ms	1048575 ph.
PILATUS 100K	172 μm	487 $\times$ 195	2.3 ms	1048575 ph.
Maxipix	55 μm	1280 $\times$ 256	0.29 ms	11180 ph.

Table 1.6: Summary of photon-counting PADs primarily used at microcrystallography beamlines.

microcrystallography beamlines listed in Table 1.2.

In a photon-counting PAD, each photon stopped in the sensor produces a current pulse on the input node of an integrating amplifier. The pulse is registered and recorded as one hit in an in-pixel counter if the stopped x-ray energy exceeds a user-defined threshold. This imposes a count rate limitation; photons arriving faster than the front-end can process and count them are lost. The PILATUS detectors are limited to about 10^6 photons/pixel/s. Since the pixel read noise is much smaller than the typical energy thresholds used, the read noise is suppressed. This can be very effective in the low-flux regime, and has lead to these detectors being advertised as "noiseless". However, detector systematics are still observed, as will be discussed in Chapter 6.

1.3.4 Photon-integrating pixel array detectors

In a photon-integrating PAD, incoming photo-generated current is integrated onto a feedback capacitor, then read out and digitized at the end of the integration period. Because the read noise in most photon-integrating PADs is much lower than the signal generated by a single x-ray, these detectors also exhibit single-photon sensitivity. Read noise equivalent to 1.3 keV deposited energy

Detector	Pixel pitch	Format	Read time	Read noise	Full well
MMPAD	150 μm	128×128	860 μs	0.16 ph.	$3{\times}10^7$ ph.
Keck PAD	150 μm	128×128	8 ms	1.07 ph.	1880 ph.
CS-PAD (LG)	110 μm	185×194	8 ms	0.46 ph.	2500 ph.
CS-PAD (HG)				0.16 ph.	300 ph.

Table 1.7: Summary of photon-integrating PADs developed by the Cornell detector group. Because multiple small-scale tiled configurations have been or are being built for each detector listed, the "format" column refers to that of a single-chip module. Quantities quoted in units of photons refer to 8 keV photons. The MMPAD has tiled into a 2×3 module format [31]. The Keck PAD was initially developed as a 16×16 pixel prototype [27]; a 2×3 tiled unit with 128×128 pixels per module is currently being built. The read time for the Keck PAD is the time required to read out 8 in-pixel frame storage capacitors from each pixel in the array. The CS-PAD [32] has been adapted as a 2.3 megapixel tiled detector at LCLS. The CS-PAD has low- and high-gain settings, denoted as LG and HG, respectively.

has been demonstrated in the Mixed-Mode PAD (MMPAD) [31] and in the CS-PAD [32]. Because charge is simply collected and integrated, there is generally no instantaneous count rate limitation, as with photon-counting PADs. Low-flux data can be thresholded during post-processing to cast the resulting image in units of number of photons, and to reject dark current and single-photon fluorescence hits, if relevant to the experiment in question. The read time of a photon-integrating PAD is comparable to that of a photon-counting PAD.

Photon-integrating x-ray PADs for synchrotron applications have been pioneered by the Cornell detector group, and are now being developed in Europe for the European XFEL. Photon integrating, as opposed to counting, is an absolute necessity at an XFEL source due to the high instantaneous flux rate inherent to the source.

1.3.5 CMOS imagers

A CMOS imager is an electronic area detector in which readout electronics are fabricated in each pixel of a silicon sensor. This stands in contrast to hybrid PADs in which the sensor and readout ASIC are physically separate layers. CMOS imagers are less expensive than CCDs or PADs, and have begun to replace CCDs in many consumer applications, such as digital cameras.

A scientific CMOS imager with 100 μm $\times$ 100 μm pixels has recently been applied to protein crystallography [33]. The x-ray stopping medium is a scintillator plate; direct-detection CMOS imagers have not yet been developed for x-ray science. Six modules were tiled with no inter-module gaps to form an active area of 28.2 cm x 29.5 cm. This detector demonstrated performance comparable to that of a phosphor-coupled CCD in conventional protein crystallography experiments. Because the imager can be framed continuously at 20 Hz, it is can be used for shutterless fine-ϕ slicing. However, the detector uses a rolling readout, in which individual rows are read out while the rest of the array is exposed. This allows for continuous framing, but can pose some difficulties in data analysis, since each row samples a different window in time. Depending on the experiment and the integration times used, this can pose a significant problem.

1.3.6 Image plates

An image plate is a phosphor plate in which color centers are formed upon exposure to x-rays. These are excited electron states that remain trapped in the phosphor crystal lattice until the plate is scanned with a red laser. The laser light causes the excited electrons to relax to the ground state, emitting blue visi-

ble light in the process. This emitted light is detected by a photomultiplier tube and recorded along with the scan position along the plate. In this way the x-ray image is read out and stored. The image plate can be erased by application of an intense flood field. While image plates are occasionally used for protein crystallography, the time required to scan and read out the image is typically on the order of minutes, which is prohibitively slow for most protein crystallography experiments at synchrotron sources.

1.3.7 Detector summary

The two classes of detectors most commonly used for protein microcrystallography, phosphor-coupled CCDs and photon-counting PADs, each have drawbacks. Phosphor-coupled CCDs have large active areas and relatively small pixels; however, the read time for large arrays is typically around 1 s, the spatial resolution is degraded by the point spread function to about 100 μm, and the read noise is around the level of a single x-ray photon. Photon-counting PADs have very low read noise which is supressed via energy thresholding, and can be read out quickly. However, their pixels are often large and, despite read-noise suppression, the detector systematics imposed by the photon-counting architecture are not negligible and deserve investigation.

Photon-integrating PADs have been proposed as detectors for protein crystallography. This application was the initial science case for development of the MMPAD [34]. Another photon-integrating PAD has recently been used to reconstruct images from extremely low-flux datasets with an average of 2.5 photons per frame [20]. This experiment was an analogue of the types of experiments

proposed for structure determination from microcrystals and single molecules at XFELs. Yet existing photon-integrating PADs suffer from similarly large pixel sizes as photon-counting PADs. Photon-integrating PADs also have yet to be built in large tiled format.

Direct-detection CCDs are promising candidates due to their small pixel sizes and tight spatial resolution. As previously mentioned, some modern CCDs are approaching read times close to those of PADs, although this is not yet common practice. However, three major roadblocks exist. First, designs must be developed that tile multiple modules together to create large-area detectors. Second, the limited well depth must be improved. Third, fabrication problems must be overcome in order to make these devices routinely available.

1.4 Document organization

Chapter 2 will cover the basic physics of x-ray detection in silicon. This lays the foundation for understanding the behavior and limitations of the detectors described in this dissertation. Chapter 3 describes area detector characterization methods. Chapter 4 describes the STA3200 direct-detection CCD, a prototype detector developed to meet the needs of protein microcrystallography. Characterization measurements have demonstrated a point spread of 22-40 μm full-width half maximum (FWHM) and read noise equivalent to 1/10 of a 13.5 keV photon. Chapter 5 describes a protein crystallography experiment performed at CHESS comparing the performance of the STA3200 to that of a standard phosphor-coupled CCD. These measurements have demonstrated that the STA3200 outperforms a standard phosphor-coupled CCD in the context

of conventional protein crystallography, despite significant design flaws. Chapter 6 describes home laboratory measurements comparing the performance of the STA3200 prototype for a range of well-controlled spot sizes and intensities, designed to simulate the types of signals expected in a microcrystallography experiment. The performance expected from a re-designed version of the STA3200 will be compared to that of a photon-counting PAD through simulation. Chapter 7 summarizes the work and draws conclusions regarding the relative merits of CCDs and pixel array detectors for protein microcrystallography.

CHAPTER 2

REVIEW OF X-RAY DETECTOR FOUNDATIONS

This dissertation is focused on x-ray detectors featuring direct detection of x-rays in silicon, a semiconductor. In order to understand the characteristics of a silicon-based detector, it is necessary to first understand the physics of semiconductors and, in particular, how charge is created and moves within the material under different conditions. Although silicon will be the focus, much of this material is applicable to other semiconductors. Following a review of the fundamentals of semiconductor physics, the detector architectures of CCDs and PADs will be described, along with the primary challenges currently facing the detector community.

2.1 Semiconductor physics

There are several general texts on semiconductor physics as applied to radiation detectors; in particular, the interested reader is directed towards Chapters 1-5 of [35], which will be cited frequently here.

2.1.1 The p-n junction

Semiconductors are classified as p- or n-type depending on the species of majority charge carriers in the material (holes or electrons, respectively). In practice, silicon is doped with electron acceptors (typically boron) or electron donors (typically phosphorous) to provide control over the majority carrier polarity and

concentration. Semiconductor wafers are frequently specified by their bulk resistivity ρ, which is related to the donor or acceptor density $N_{D,A}$ via

$$\rho = \frac{1}{q\mu_{n,p}N_{D,A}} \tag{2.1}$$

where q is the elementary charge and $\mu_{n,p}$ is the electron or hole mobility, respectively. The charge carrier mobility scales with temperature as $T^{-2.42}$ for electrons and $T^{-2.20}$ for holes, with room temperature values $\mu_n = 1500$ cm^2/V·s and $\mu_p = 500$ cm^2/V·s in silicon [36].

With the use of photolithographic masks, localized regions can be selectively doped with either species. The junction between adjacent p- and n-type regions behaves as a diode, i.e. current is conducted only in one direction. If no bias is applied to the junction, free carriers from either side diffuse across the junction. As free carriers diffuse, they leave behind a region with only fixed, immobile charge carriers, called the self-depletion region. The self-depletion region grows until the electric field across the region balances the free carrier diffusion, typically a few tens of microns wide in silicon. Due to the local charge polarization across the junction, the self-depletion region has a built-in voltage V_{bi}, typically around 0.5 V in silicon, given by

$$V_{bi} = \frac{k_B T}{q} \ln \frac{N_A N_D}{n_i^2}. \tag{2.2}$$

where k_B is the Boltzmann constant, T is temperature, and n_i is the intrinsic carrier density of the material (1.45×10^{10} cm^{-3} in silicon).

An external bias can be applied across the junction. If the p-type side is at a higher voltage than the n-type side, the diode is forward-biased and conducts current. If the p-type side is at a lower voltage than the n-type side, the diode is reverse-biased. The reverse bias pulls more free charge carriers out of the

diode, widening the depletion region. The only current conducted across the depletion region is due to charge carriers generated thermally or through the absorption of radiation. The thermally-generated current, called leakage current, increases with the depletion region volume, temperature, and concentration of non-dopant impurities, such as transition metals.

To create an efficient x-ray sensor, a thick depleted volume capable of stopping a high fraction of incident x-rays is required. For x-ray energies in the range 2-20 keV, as used in protein crystallography, a silicon sensor some hundreds of microns thick is desired, as illustrated in Figure 2.1. Ideally, the full sensor volume should be depleted, so that the photo-generated charge is collected efficiently; that is, with minimal spatial spreading and signal loss from charge carrier recombination.

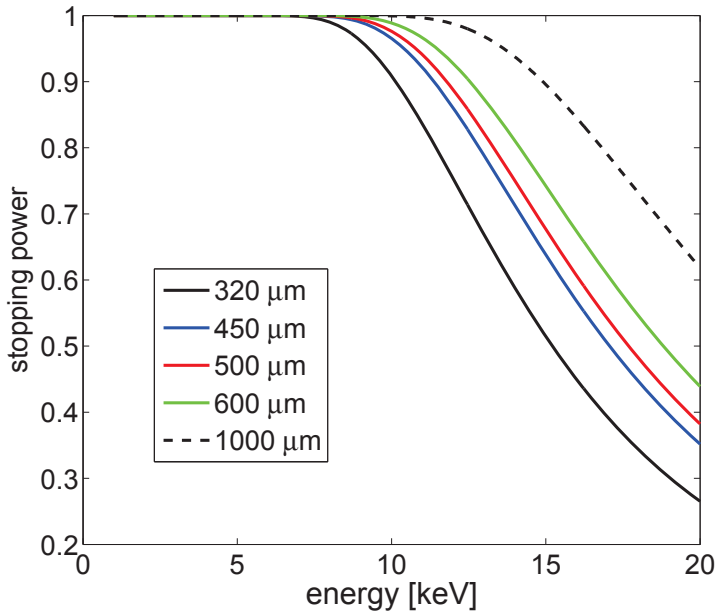

Figure 2.1: Silicon sensor stopping power as a function of energy for various sensor thicknesses. The PILATUS detectors use a standard sensor thickness of 320 μm; 450 μm and 1000 μm sensors are also offered. Most of the recent Cornell detector group PADs have used a 500 μm sensor. The STA3200 direct-detection CCD uses a 600 μm sensor.

To achieve this, a thick slab of lightly-doped (i.e., high-resistivity) silicon is used. To create a p-n junction, a heavily-doped layer of the opposite polarity to the bulk is fabricated on one side. In an asymmetric junction such as this, the depletion region width is given by [35]

$$d = \sqrt{\frac{2\epsilon\epsilon_0}{qN_{D,A}}(V_{bi} - V_{ext})} \tag{2.3}$$

where ϵ is the dielectric constant of the material (ϵ_{Si} = 11.8), ϵ_0 is the dielectric constant of free space, and V_{ext} is the external bias (note that V_{ext} is negative for reverse bias). If the built-in voltage is small compared to the external voltage, equation 2.3 can be approximated as

$$d = \sqrt{\frac{2\epsilon\epsilon_0}{qN_{D,A}}|V_{ext}|}. \tag{2.4}$$

This equation illustrates the importance of using high-resistivity (i.e., low $N_{D,A}$) silicon in x-ray sensors. For a given sensor thickness and resistivity, Equation 2.4 can be used to determine the minimum external voltage required to achieve full depletion, as illustrated in Figure 2.2. A larger reverse bias will over-deplete the sensor, imposing a large transverse electric field that sweeps the photo-generated charge carriers efficiently towards the pixel collection nodes.

2.1.2 Photon conversion in silicon

At the photon energies of interest here, charge carriers are generated in the sensor via the photoelectric effect. When a photon is absorbed, it creates a shower of free electron-hole pairs. The average number of charge carrier pairs generated is given by the ratio of the deposited energy to energy required to gen-

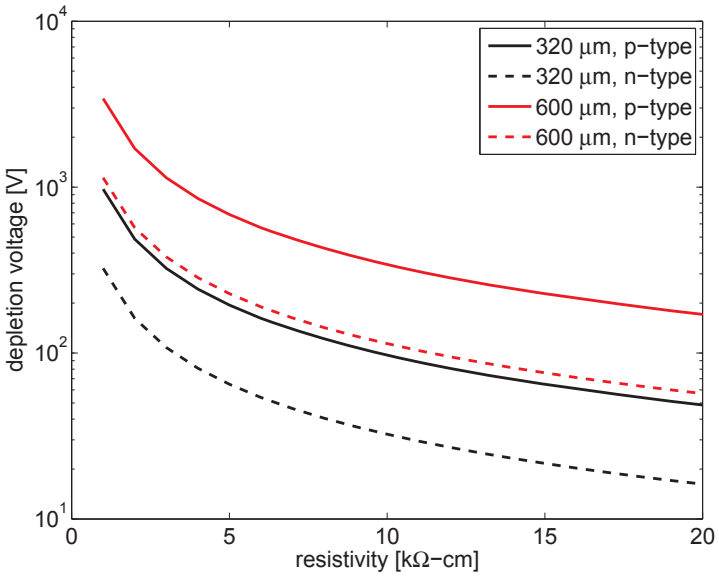

Figure 2.2: Depletion voltage vs. resistivity for 320 μm and 600 μm thick silicon sensors.

erate one electron-hole pair (3.6 eV in silicon). Thus, thousands of charge carriers are created by the absorption of a single x-ray photon. While one might expect such a process to follow Poisson statistics, because there are limited channels into which the absorbed x-ray energy can go (i.e., the production of each charge carrier pair is not independent) the uncertainty in the number N of charge carrier pairs generated is better than $\sqrt{N}$. Instead, the variance is given by $< \Delta N^2 >= FN$, where F is the Fano factor. The value of the Fano factor is a characteristic of the specific semiconductor material and is equal to 0.1 for silicon [35].

2.1.3 Charge transport in silicon

In the absense of an external electric field, charge carriers diffuse freely with diffusion constant $D = \frac{k_B T}{q} \mu_{n,p}$. Since the absorption of an x-ray creates a cloud

of charge carriers, we will usually consider the behavior of the cloud, rather than that of individual carriers. It can be shown that under diffusion the charge carrier cloud expands after time t in a Gaussian profile with width [35]

$$\sigma = \sqrt{2Dt}. \tag{2.5}$$

In the presense of an external electric field $\mathbf{E}$, charge carriers drift with equation of motion

$$\begin{aligned} \mathbf{v_n} &= -\mu_n \mathbf{E} \\ \mathbf{v_p} &= \mu_p \mathbf{E} \end{aligned} \tag{2.6}$$

for electrons and holes, respectively. This relation holds until the saturation velocity is reached. The saturation velocity at room temperature is approximately 1×10^7 cm/s for electrons and 8.4×10^6 cm/s for holes.

These equations provide the framework for understanding charge transport in two relevant cases: an underdepleted and an overdepleted sensor.

Transport in an overdepleted sensor

As mentioned above, for efficient x-ray detection, an overdepleted diode is desired. We approximate this scenario as having a purely transverse electric field, with no lateral component. Charge carriers are swept towards the pixel electrodes with velocity determined by Equation 2.6. It is possible to use Equation 2.6, along with the electric field profile across the diode, to derive the charge collection time for specific sensor configurations (i.e., sensor thickness, external bias, temperature, and charge carrier polarity). For a 500 μm planar silicon sensor, charge collection times around 10 ns are reasonably achievable. Shorter

collection times, approaching 100s of ps, have been calculated for 3D silicon sensors using internal trench electrodes as collection nodes [37].

As charge carriers are swept across the diode by the overbias field, they simultaneously undergo diffusive motion in the lateral plane, where we have assumed no electric field component. The charge cloud expands to a width given by Equation 2.5. A short collection time is desired not only for the sake of rapid charge collection, but also in order to limit the charge cloud spread, which is the primary source of point spread in an overdepleted sensor. The point spread is thus referred to as being charge diffusion limited. The exact charge cloud size depends on multiple factors including the overbias voltage, the sensor temperature, and the x-ray conversion depth within the sensor. Appendix A includes calculations of the charge collection time and charge cloud size for a few relevant scenarios.

Transport in an underdepleted sensor

The sensors considered in this dissertation are all operated such that x-rays enter the sensor on the side opposite the pixel collection nodes. The collection nodes form the p-n junctions from which the depletion region expands into the sensor volume. Therefore, if the sensor is not biased sufficiently high to achieve full depletion, there will be an undepleted region on the x-ray entrance side. This has significant consequences for the sensor efficiency and spatial resolution.

Consider an x-ray stopped in the undepleted region. The photo-generated charge carriers, seeing no electric field, diffuse in three dimensions. The charge cloud profile is modeled as a Gaussian with width given by Equation 2.5.

Charge carriers continue to diffuse outward from the generation point until they either reach the edge of the depletion region or are lost at the sensor boundary or to recombination. The recombination time depends on the impurity concentration of the material, but in high-resistivity silicon lifetimes on the order of milliseconds are typical [38]. Thus, it is possible for a charge cloud in the undepleted region to achieve significant lateral spread before dissipating or reaching the depletion region. Upon entering the depletion region, the charge carriers see the transverse electric field and the overall motion proceeds as described above for a depleted diode. However, any lateral spread that has already occurred is preserved, thus diluting the spatial resolution.

The extent to which the undepleted region affects the sensor quality depends on its thickness relative to that of the depleted region, and on the x-ray energy. Higher energy x-rays are more likely to convert farther away from the x-ray entrance side, making them less sensitive to the undepleted region.

2.1.4 Damage

Radiation damage and electrical breakdown of the sensor are both concerns during the operation of deeply-depleted semiconductor radiation detectors. Both topics are covered in [35]. Radiation damage is also reviewed in [39], as it pertains to CCDs, and extensively in [40], which includes radiation hardening techniques for CMOS devices.

Radiation damage

The primary source of radiation damage in a silicon sensor is the trapping of holes in the oxide [39]. Within the oxide, photo-generated holes become trapped due to their low mobility (1.6×10^{-5} cm^2/V·s in SiO_2, compared to 20 cm^2/V·s for electrons), which generates a flat-band voltage shift that can interfere with sensor operation. Trapped charge at the Si-SiO_2 interface can generate an additional voltage shift, as well as increasing the dark current generated at the interface.

Thin oxide layers, which absorb less energy per unit flux, and from which trapped holes have a higher probability of escape by tunneling, are more robust to radiation damage than thicker oxides. The oxide thickness for the TSMC 0.25 μm 3.3 V CMOS process, which has been used in most recent Cornell detector group PADs, is 7 nm. In contrast, the gate oxide used in DALSA's CCD process, used to fabricate the STA3200 direct-detection CCD, is 50 nm.

In an x-ray detector with a thick silicon sensor, the sensor itself shields the oxide layers from much of the incident radiation. As an example, a photon-integrating PAD normally operated with a 500 μm thick silicon sensor has demonstrated radiation tolerance up to 600 kGy dose absorbed by the bare ASIC [27]. At 13.5 keV this would translate to a flux of 1.0×10^{17} ph/mm^2 incident on the sensor face (considering only the shielding from the sensor, and ignoring the additional shielding of the ASIC by the metal bump bonds). The F1 beamline at CHESS reports a flux of 5.5×10^{9} ph/s at 13.5 keV through a 100 μm collimator; under these conditions, the oxide dose limit would be reached after 1.5×10^{5} s in the direct beam. In contrast, as will be shown in Chapter 4, the dose limit of the STA3200 CCD oxide is about 132 Gy. The STA3200 has a 600 μm thick sensor

and would reach its dose limit in about 139 s in the F1 direct beam.

Electrical breakdown

In biasing the sensor into overdepletion, there is a risk of damaging the sensor via electrical breakdown. Electrical breakdown occurs when covalent bonds in the semiconductor lattice are broken, by the electric field alone (Zener breakdown) or by collisions with free charge carriers that are sufficiently accelerated by the electric field to break bonds (avalanche breakdown) [35]. In either breakdown mode, it is the heat generated by the sudden power surge due to the breakdown current that causes permanent damage to the silicon.

To mitigate the risk of breakdown, a guard ring structure can be fabricated onto the sensor. A series of concentric rings with the opposite doping to that of the bulk matieral are fabricated on one side of the diode, as shown in Figure 2.3. The innermost ring is biased to an intermediate voltage V_{sc}, between V_{ext} and the pixel electrode voltage, and with the outer rings left floating (for example, for the STA3200 CCD V_{sc} = 10-20 V when V_{ext} = 155 V). The reverse bias voltage is applied from a contact further inward than the innermost guard ring. As the depletion region grows outward, it punches through to neighboring guard rings, such that the voltage drop is distributed across the rings and the electric field between any two adjacent rings does not get high enough to cause electrical breakdown. Since the concern is having too large a voltage across too narrow a gap, the inter-ring spacing is an important parameter. A ring spacing of 30 μm has been successfully used in the Cornell detector group PADs to allow safe biasing of 500 μm, 10 kΩ-cm diodes up to 190 V.

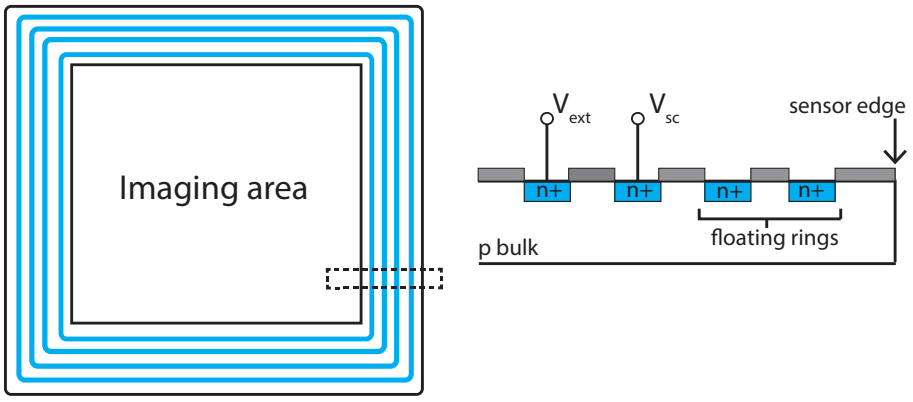

Figure 2.3: Guard ring structure. At left, the sensor is viewed from above. At right, the portion within the dotted lines is shown from the side. A sensor with a p-bulk is shown; an n-bulk sensor would have floating p+ rings. The innermost guard ring is biased at V_{sc}, with the outer rings floating. V_{ext} is the voltage applied to deplete the sensor. The guard rings are not shown to scale relative to the imaging area; rings are typically on the order of tens of microns thick.

2.2 Semiconductor devices and fabrication

In addition to the p-n junction, metal-oxide-semiconductor (MOS) devices are important to the operation of electronic area detectors. These are devices fabricated using a silicon substrate (possibly the silicon sensor itself), a layer of insulating oxide, and layer of conducting material: a metal or, more commonly, highly-doped polycrystalline silicon (called polysilicon, or "poly"), which serves as a gate to which voltages may be applied. Two MOS devices are of particular importance: the MOS capacitor and CMOS transistor. General references include [35], [39] (particularly for MOS capacitors), and [41] (for CMOS transistors).

2.2.1 The MOS capacitor

The MOS capacitor, shown in Figure 2.4a is the basic charge-storage element in the CCDs considered in this dissertation. The oxide contributes capacitance per unit area C_{ox} equal to

$$C_{ox} = \frac{\epsilon_{ox}}{d_{ox}} \tag{2.7}$$

where ϵ_{ox} is the permitivity of the oxide and d_{ox} is the thickness. For silicon dioxide (SiO_2), $\epsilon_{ox} = 3.45 \times 10^{-8}$ F/cm^2. A dual layer of SiO_2 and silicon nitride, which has a permitivity of $6.63{\times}10^{-8}$ F/cm^2, can be used to increase the oxide capacitance [39]. Additionally, if the gate is biased such that the semiconductor directly under the oxide is depleted, the depletion region (referred to as the "channel" in a CCD) contributes its own capacitance given by

$$C_{dep} = \frac{\epsilon_{Si}}{x_d} \tag{2.8}$$

where x_d is the depletion region thickness.

(a) A MOS capacitor.

(b) A MOS capacitor with buried channel.

Figure 2.4: MOS capacitors.

Charge collected at the Si-SiO_2 interface can become trapped by defects at the interface. To mitigate this effect, a variation on the MOS capacitor with a buried channel can be made. As shown in Figure 2.4b, a thin layer of oppositely doped silicon is placed between the bulk and the oxide. This layer modulates

the potential well shape such that charge is collected just under, rather than directly at, the interface. In a CCD, this improves the charge transfer efficiency.

2.2.2 The transistor

A CMOS (complimentary metal-oxide-semiconductor; the "complimentary" refers to the fact that p- and n-channel devices can be fabricated on the same substrate) transistor is the basic building block of every amplifier that will be discussed in this dissertation. As shown in Figure 2.5, two diffusions, the source and drain, with one polarity (n- or p-type) are fabricated at the surface of the bulk silicon of the opposite polarity, with an oxide/gate structure in between. The gate voltage controls the potential well under the oxide, as in the MOS capacitor. When the gate is biased such that a depletion region forms underneath, thermally generated minority carriers are drawn from the bulk towards the Si-SiO_2 interface, forming a conducting channel beneath the gate oxide between source and drain. As the gate voltage increases, more free carriers are drawn into the channel, increasing the drain-to-source current I_D. The transistor is characterized by its transconductance $g_m = \partial I_D / \partial V_{GS}$, where V_{GS} is the voltage drop from the gate to the source, and its output resistance r_0, the resistance as seen looking into the source node.

To first order, a transistor is "off" (i.e., conducts no current) until the gate-to-source voltage V_{GS} exceeds the threshold voltage V_{th}. For a given process, V_{th} has a nominal value determined by, among other things, the oxide thickness (a thinner oxide leads to a lower V_{th}); to second order, V_{th} can be affected by the source-to-bulk (substrate) bias V_{SB}. This is called the body effect and is

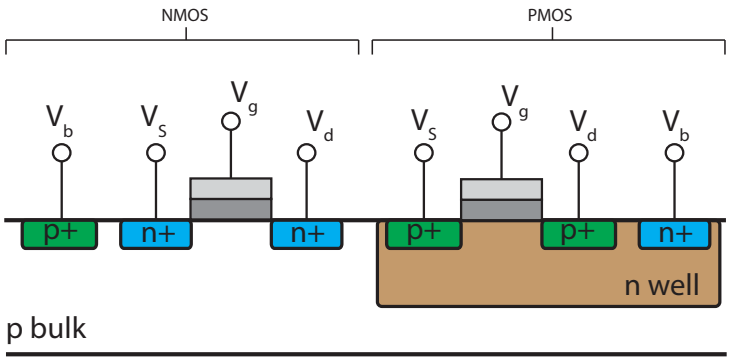

Figure 2.5: CMOS transistors.

described by

$$V_{th} = V_{th0} + \gamma \left(\sqrt{|2\Phi_F + V_{SB}|} - \sqrt{|2\Phi_F|} \right) \tag{2.9}$$

where V_{th0} is the nominal value, $\Phi_F = \frac{k_B T}{q} \ln(N_{sub}/n_i)$ where N_{sub} is the substrate doping concentration, and $\gamma = \sqrt{2q\epsilon_{Si}N_{sub}}/C_{ox}$ is the body effect coefficient. The body effect also leads to a dependence of the drain-source current on the substrate bias, described by the parameter $g_{mb} = \partial I_D / \partial V_{BS}$. It can be shown [41] that g_{mb} is given by

$$g_{mb} = g_m \frac{\gamma}{2\sqrt{2\Phi_F + V_{SB}}}. \tag{2.10}$$

Once V_{GS} exceeds V_{th}, the transistor conducts current through its channel. The exact relationship between I_D, V_{GS} and V_{DS} depends on the relative value of V_{GS} to V_{DS}; the interested reader is referred to [41] for more details. Here, we will limit the discussion to the "saturation" region of transistor operation, when $V_{GS} > V_{th}$ and $V_{DS} > V_{GS} - V_{th}$. In this region, for an NMOS device I_D is given by

$$I_D = \frac{1}{2}\mu_n C_{ox} \frac{W}{L} (V_{GS} - V_{th})^2 . \tag{2.11}$$

That is, I_D is independent of V_{DS}, and g_m is proportional to W/L. For PMOS devices, μ_n is replaced by μ_p, and I_D is defined as negative to reflect the direction of current flow.

2.3 Fabrication of high-resistivity silicon

As seen above, a basic requirement for detector-grade silicon is that it have a high resistivity, so that a large volume can be depleted using a reasonably achievable reverse-bias voltage. 100-500 V is a practical value. Another requirement is that the minority carrier lifetime be long, in order to suppress the leakage current, as the two quantities are inversely related [35]. Therefore, it is vital that detector-grade silicon have very few impurities.

To achieve the high resistivity and low impurity levels required, most detector-grade silicon is fabricated through the float-zone process. Useful overviews of this process can be found in [38] and [42]. A polysilicon feed rod is suspended by its ends and rotated continuously as it is pulled through an RF coil, which heats the rod by induction. Because most of the impurities, including the p- and n-dopants, typically found in the starting material are highly mobile, they are concentrated in the molten zone and are therefore pushed progressively towards one end of the rod. This portion can later be cut off and discarded. Multiple passes through the heating coil can be made to achieve progressively higher-resistivity material. However, convection patterns within the molten zone cause striations of doping inhomogeneities in the final silicon wafers. These striations create small local lateral electric fields which deflect charge carriers from their intended trajectories, leading to geometric distortions, as will be discussed in Chapter 3.

Purity is not only a concern during the fabrication of the high-resistivity wafer itself. Care must be taken that impurities are not introduced during any processing steps the high-resistivity wafer undergoes after its initial fabrication.

The minority carrier lifetime is particularly susceptible to degradation by transition metal impurities. In-process gettering techniques have been developed to mitigate this issue and allow the fabrication of integrated circuits directly on high-resistivity substrates [43].

Of particular interest here is the fabrication of transistors on the high-resistivity silicon substrate required for a deep-depletion CCD. The advantages of transistors fabricated on high-resistivity silicon have been described elsewhere [44], and include minimal capacitance from the p-n junction to the substrate, due to the thickness of the depletion region, and reduced body effect, due to the reduction of the parameter γ in equation 2.9. This allows the transistor to be operated in the presence of the high substrate bias that is required to deplete the sensor.

2.4 Area detector basics

In this section, an overview of the charge collection and readout architectures of CCDs and PADs is presented. These structures are independent of the sensor used; for example, a direct-detection and a phosphor-coupled CCD have the same basic charge collection and readout architecture. Useful references for radiation detectors in general are [35] and [45]. CCDs are comprehensively reviewed in [39]. Previous work within the Cornell detector group on photon-integrating PADs is well-documented in [46] and [27].

2.4.1 CCDs

In a CCD, charge is collected in potential wells within the pixels, then clocked out through the imaging pixels themselves (also called the parallel register) to the edge of the imaging area. There, the charge packets enter a set of non-imaging pixels called the serial register, through which they are clocked until reaching a readout amplifier which converts the signal to a voltage which can be digitized and recorded.

In the CCDs considered here, the parallel register is made up of an array of MOS capacitors.[1] The channel is depleted of free charge carriers, and photocharge generated in the bulk is collected in potential wells within the channel. The amount of charge that can be stored in each pixel (the pixel well depth) is directly proportional to the pixel charge collection area (discussed below) and to the channel doping concentration [39].

Each pixel is made of up multiple MOS capacitors, typically 3 or 4 per pixel (called, respectively, a 3- or 4-phase pixel). Each phase is biased independently in order to produce the potential wells that define the charge collection region within the pixel. By clocking the gate biases during readout, packets of charge can be shifted from one pixel to the next with near 100% charge transfer efficiency.

The choice of phasing involves a few design trade-offs. A four-phase pixel has a larger well depth than a three-phase pixel of the same size, since two phases can be used to collect charge during exposure, as shown in Figure 2.6. However, for the same size pixel, each phase must be smaller in a four-phase

[1] Deep-depletion pn-CCDs, which have no oxide layer between the channel and the pixel gates, have also been developed for x-ray detection [28].

than in a three-phase pixel. This can run up against lithographic tolerances and lead to inter-phase shorts, which can destroy device performance. The serial register may have a different phasing than the parallel register, and it is typically clocked at a different frequency.

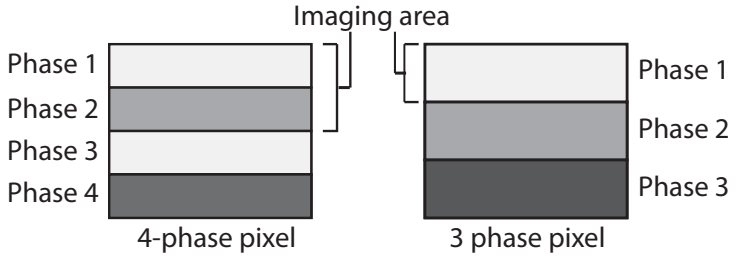

Figure 2.6: Charge storage area in a 3- vs. 4-phase CCD pixel.

In the early days of CCD development, only a thin depletion region could be achieved due to the low resistivity (some tens of Ω-cms) of the silicon used. Therefore, it was more efficient to illuminate through the gates, because optical photons would convert close to the channel and a larger fraction of the charge could be collected. Because of this, the gate side is referred to as the "front side" of the CCD. CCDs illuminated from the non-gate side, as with most deep-depletion CCDs, are said to be "back-side illuminated".

The output amplifier in a CCD is almost invariably configured as shown in Figure 2.7, a transistor configuration called a source follower. The voltage gain of the source follower is given by [41]

$$A_v = \frac{g_{m1} R_S}{1 + (g_{m1} + g_{mb1}) R_S} \tag{2.12}$$

where g_{m1} and g_{mb1} refer to transistor M1 and R_S is the impedance seen at the source node. The net charge-to-voltage gain of a CCD with this output amplifier is then

$$A_{tot} = \frac{1}{C_{sense}} \frac{g_{m1} R_S}{1 + (g_{m1} + g_{mb1}) R_S} \tag{2.13}$$

where C_{sense} is the sense node capacitance. If $g_{m1}R_S$ is large, the amplifier gain approaches unity and the charge-to-voltage gain of the detector approaches $1/C_{sense}$.

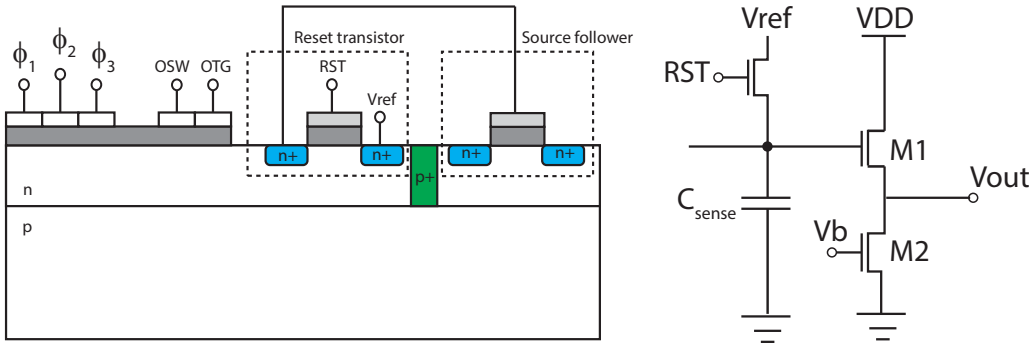

Figure 2.7: CCD output region. A cross-sectional view is shown at left and a schematic view at right. The output summing well (OSW) is the potential well in which charge packets from multiple pixels are summed in the case of on-chip binning. The output transfer gate (OTG) controls when a packet of charge is clocked out of the OSW and onto the sense node.

2.4.2 Pixel array detectors

In contrast to CCDs, which are monolithically fabricated, the pixel array detectors described herein are hybrid devices. As described in Chapter 1, a semiconductor sensor is bump-bonded pixel-by-pixel to a readout ASIC. This has the benefits of allowing for more sophisticated readout circuitry, faster readout, and electronic shuttering, but constrains the pixel size to be larger than that found in CCD processes, due to the need to accomodate both the in-pixel circuitry and the size of the bump bond.

The sensor is shown schematically in Figure 2.8. As with CCDs, the bulk may be either p- or n-type semiconductor, with the pixel implant the opposite

polarity. Since the pixel implant is connected to a metal bump-bond and then the ASIC, PADs are universally illuminated from the opposite side, as shown. The aluminum contact on the x-ray entrance side, which provides a conductive contact for applying the sensor reverse bias, must be thin enough to allow good x-ray transmission. An aluminum contact thickness of about 700 nm is typical.

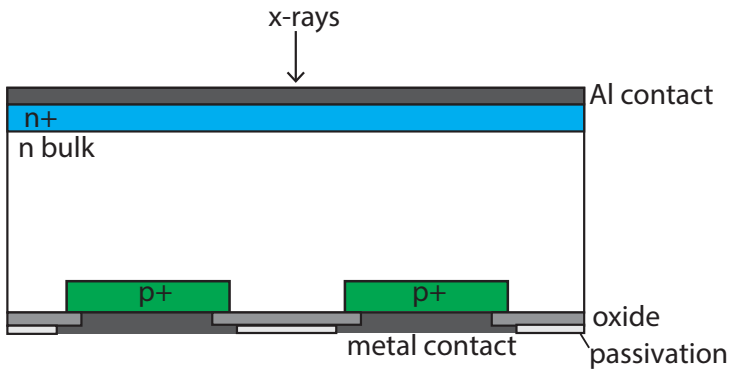

Figure 2.8: PAD diode layer (not drawn to scale).

Typical bump bond materials are solder, indium, or gold. The bump bonds offer additional radiation shielding to the ASIC. Cornell detector group PADs have typically used bump bonds with 75-85 μm diameter, while bump bonds 15-25 μm in diameter have been used in the PILATUS detectors [47]. A PAD with 25 μm pixels is currently under development at PSI, and with modest success at bump-bonding at this scale [48].

A high-level schematic of the PAD pixel electronics is shown in Figure 2.9. Every PAD currently in production or development has a charge-integrating front-end amplifier, followed by some kind of processing electronics. Whether the PAD is a photon-counting or -integrating device depends on the size of the front-end feedback capacitor and the nature of the in-pixel processing electronics.

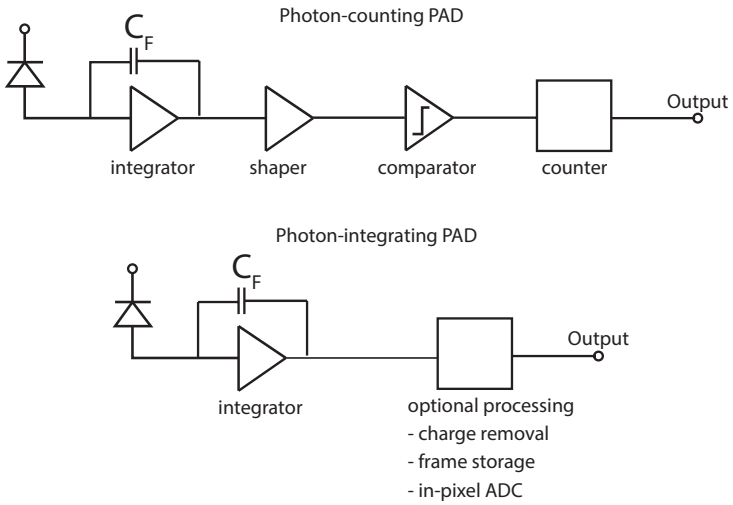

Figure 2.9: PAD pixel electronics.

In a photon-counting PAD, the feedback capacitor is small, so that the charge collected from a single x-ray in the energy range of interest produces a voltage swing at the amplifier output sufficiently large to trigger a comparator. The reference voltage of the comparator corresponds to the voltage swing expected for an x-ray of a specific energy. When the comparator is triggered, an in-pixel counter is incremented and the front-end is reset.

The speed at which the thresholding decision can be made, and the counter incremented, limits the maximum acceptable hit rate of the detector. The count rate limitation of the PILATUS detectors has typically been reported as 10^6 ph/pixel/s. This is the level where the dead time for processing a single photon hit becomes significant relative to the incoming signal; beyond this level, some (but not all) incoming photons are lost and the observed count rate is less than the incoming count rate. The relative amount of signal lost depends on the incoming count rate and its time structure, as detailed in [49]. In order to bleed off any signal that falls below the energy threshold, the front end usually has a DC compensation circuit to bleed off low-level signals, including accumulated

charge from dark current.

Energy thresholding has another consequence in terms of detector systematics. As described above in Section 2.1.3, photo-generated charge in an overdepleted sensor diffuses as it travels towards the pixel collection nodes. As a result, the photo-generated charge can be split between neighboring pixels. Depending on the exact value of the comparator reference voltage in each pixel, the photon may be counted by more than one pixel, or it may be missed entirely. This problem has been remedied in the Medipix3RX photon-counting PAD through use of arbitration circuits which compare the amount of charge recorded by neighboring pixels during a single shared photon hit and allocate the photon hit accordingly [50]. This strategy has not yet been implemented in the PILATUS family of detectors.

In a photon-integrating PAD, the feedback capacitor is larger, so that charge from a large number of photons can be collected in a single exposure. The output of the integrator is sampled, potentially processed in some way, and read out. The purpose of the in-pixel processing electronics varies from detector to detector. The CS-PAD uses an in-pixel analog-to-digital converter (ADC) to digitize the front-end output before readout. In the MMPAD, the processing block includes a charge-removal circuit that removes a fixed packet of charge from the integration capacitor when a certain signal threshold is passed and increments a counter; this extends the dynamic range of the detector signficantly, but does impose an instantaneous hit rate limitation of 10^{12} ph/pixel/s [31]. The Keck PAD has a bank of in-pixel frame storage capacitors, which can be re-addressed for repeated charge accumulation before readout of the chip. This raises the maximum continuous frame rate of the device to the MHz regime. Because

photon-integrating PADs integrate photo-generated charge rather than processing photon hits individually, they have less stringent count-rate limitations, and charge sharing between pixels does not result in over- or under-counting photons.

2.5 Major challenges

Here, some of the challenges presently facing the detector community are described. These range from the mechanical and electronic design of medium- to large-scale detectors, to developing efficient detector calibration methods that are transparent to the end user. This discussion is intended to provide the background against which many of the design choices for detectors discussed in this work were made.

2.5.1 Tiling modules

Although successful science can be done with small detectors, many users want or need larger active areas. Protein crystallographers, in particular, require large area detectors. The size of a single-chip module for semiconductor devices is limited, first, by the available wafer sizes in the relevant processing technology. Many foundries, especially those specialized for work with high resistivity silicon, are limited to 6-inch wafer production and processing. This limits the maximum square device size to about 96 mm. In hybrid devices such as PADs, the limit on the ASIC size is more stringent, since foundries limit the reticle step size; that is, the maximum size for a single chip is much less than the wafer size.

For the TSMC 0.25 μm process the reticle size is about 21 mm. This sets the size of a single ASIC. Multiple modules must be tiled together to make a detector with an active area comparable to that of a commercially-available phosphor-coupled CCD.

The major hurdle in tiling multiple direct-detection devices together is accomodating the electrical connections that usually exist along at least one edge of the module. So far, the approach has been to make single modules three-side buttable, with gaps between modules to accomodate the connections (typically wire bonds). Through-silicon vias offer a way towards minimizing this problem, by making electrical connections to the back of the ASIC rather than the side, but have not yet been realized in a commercially available large area x-ray detector.

2.5.2 Vacuum windows

Ideally, photon-integrating detectors should be operated below room temperature to minimize dark current and improve device stability. Cooling requires that the detector be run inside a vacuum housing so that condensation is avoided. A suitable vacuum window must be used that allows sufficient transmission of x-rays in the energy range of interest.

Aluminized mylar is a good choice for small detector modules, and has been used on multi-module PADs up to 42 mm $\times$ 63 mm. However, it bows significantly under vacuum, so it is impractical for larger areas. Carbon fiber fabric is strong and bows much less, but it attenuates low energies strongly and significantly decreases the x-ray efficiency of the system. Thin silicon nitride has been

used to make a small-area window on a tapered nose from the detector face, but this limits the flexibility of detector placement and sample-to-detector distance. Beryllium windows are almost ideal in terms of strength and x-ray transmission, and can be made fairly large (several inches in diameter), but pose a safety and health hazard, as beryllium is highly toxic.

2.5.3 Pixel size

Small pixels provide high spatial resolution in the detector plane and are thus highly desirable. Very small pixels are difficult to achieve in PADs due to the need to accomodate a large amount of circuitry in the pixel in the ASIC layer. This constraint is exacerbated in designs that include large integration capacitors and/or in-pixel frame storage capacitors, since capacitors are area-hungry elements. In the TSMC 130 nm, 180 nm and 0.25 μm processes, MiM (metal-insulator-metal) capacitors have a capacitance of 1 fF/μm^2. The IBM 130 nm process, used in the Adaptive Gain Integrating Pixel Detector (AGIPD) [51], offer 2 fF/μm^2 capacitance. Additionally, hybrid devices must have pixel sizes that accomodate the need to bump-bond the sensor to the readout ASIC.

The pixel size is also constrained in a CCD process, though not as stringently. The design rules for DALSA's standard CCD process allow a minimum poly layer width of 2.5 μm, which sets the minimum width for a single phase (recall that there are typically 3-4 phases per pixel). Additionally, the full well scales with the pixel size; this is especially important for direct-detection CCDs, since a single x-ray generates thousands of charge carriers that can quickly saturate a modestly sized pixel. The maximum pixel size is also constrained by the need

to maintain good charge transfer efficiency (CTE). Consider a typical pixel with 3 or 4 poly phases; if the pixel is too large, the phases themselves are so wide that charge carriers collected in the channel cannot be efficiently moved from one phase to the next, as charge carriers near the center of the phase will not see the potential gradient between phases.

Some consideration as to the minimum pixel size required for a given experiment is warranted. If the pixels are smaller than the features of interest, then sub-pixel spatial resolution may be attainable by centroiding; additionally, for a given flux (photons/s/μm^2), individual pixels experience a lower instantaneous hit rate, which can ease hit rate concerns for photon-counting systems. However, every additional pixel added to compute the total intensity of a feature contributes read noise. A small pixel size also requires more pixels to cover a given area, which means larger data files to stream to disk, store, and process. Due to these considerations, support electronics for CCDs should be designed to allow for on-chip binning, so that multiple pixels can be summed without read noise penalty, the frame rate can be increased, and the image file sizes decreased when the loss of spatial resolution is deemed acceptable.

Regardless of pixel size, the spatial response of the sensor (i.e., the point spread function) is ultimately limited by the charge cloud width, as described in Section 2.1.3.

2.5.4 Calibrations

The performance of a detector is strongly influenced by its calibration. The primary quantities to be calibrated are the efficiency of the sensor, the gain of each

readout amplifier, and the effective area of each pixel. Detailed calibration techniques will be discussed in Chapter 3. Here, a few words about the issue of calibrations in general.

A major challenge in performing a high-quality detector calibration is that very large datasets are required to be collected and processed. Ideally, the gain of each amplifier and the area and efficiency of each pixel must be measured independently. As such, calibration difficulty trades with pixel density and frame rate (often accomplished via the use of additional readout amplifiers, each of which must be calibrated independently).

Corrections must also be applied to experimental data in a way that is transparent to the end user, and the correction should not introduce additional features or systematics to the processed data. A corrections routine that is complicated or time-consuming to execute may be ignored by the user, in which case the detector may as well be un-calibrated; even if applied, a time-consuming corrections routine slows down data analysis and can preclude performing basic analysis at the beamline, wasting valueable beamtime.

CHAPTER 3

AREA DETECTOR CHARACTERIZATION METHODS

3.1 Introduction

All detectors exhibit systematics that must be characterized and accounted for in order to achieve optimum device performance. Systematics arise primarily from process variations in integrated circuit fabrication and variations in sensor quality (i.e., thickness, resistivity). Furthermore, characterization methods, and image correction routines, must be developed to suit particular applications and detector families. For example, calibration procedures for phosphor-coupled CCDs primarily address zinger removal, background subtraction, variation in sensitivity, and correction of area distortions arising from structure within the fiber optic taper [52]. Calibration procedures for PADs also address background subtraction, but focus heavily on pixel-by-pixel amplifier gain correction and correction of area distortions arising from resistivity variations in the sensor [53]. Calibration procedures for photon-counting PADs must further address the precise trimming of in-pixel comparators, ideally to better than 1% [54].

In this chapter, some basic imager calibration methods will be reviewed. Established methods for measuring efficiency, spatial resolution, and gain will be covered. Additionally, a method for measuring and correcting pixel area distortions developed during the course of this dissertation work will be presented. Finally, the impact of image correction routines on recorded data will be considered. The MMPAD will be used as an example case for many of the methods covered.[1]

[1]Parts of this work were presented at the 2012 International Conference on Synchrotron Ra-

3.2 Detective quantum efficiency: a measure of performance

The detective quantum efficiency (DQE) is a measure of the detector's impact on the SNR, and is defined as:

$$\mathrm{DQE} = \frac{(S_{out}/N_{out})^2}{(S_{in}/N_{in})^2}. \tag{3.1}$$

where S_{out} and N_{out} are the signal and noise recorded by the detector (i.e., coming "out" of the detector), and S_{in} and N_{in} are the signal and noise incident on the detector face. The DQE can be used as a metric of overall detector performance, accounting for the net effect of all detector systematics on a given dataset: read noise, geometric distortion, gain variations, etc. An ideal detector would have a DQE of 1, i.e. it would record the experimental signal perfectly and introduce no noise or other systematics.

The DQE is a function of the incident dose, and can also vary with several quantities including photon energy and measured feature size. Detector systematics can manifest differently, for example, when measuring isolated spots versus continuous features. This will be discussed in greater detail in Section 3.8. The DQE can be used to compare the performance of different detectors under identical experimental conditions, or to compare the performance of a given detector in different experimental conditions. It can also be used to test the efficacy of detector calibrations, as will be discussed.

diation Instrumentation (SRI 2012), and have been published in Journal of Physics: Conference Series [53].

3.3 Efficiency measurements

The efficiency of a sensor varies with photon energy. Consider a silicon sensor of thickness t. The transmission through the sensor is given by

$$T = \exp(-n\mu_a t) \tag{3.2}$$

where n is the number of atoms per unit volume in the sensor and μ_a is the atomic photoabsorption cross section of the material. Thus the stopping power is given by

$$A = 1 - \exp(-n\mu_a t). \tag{3.3}$$

Ideally, this would give the actual efficiency of the sensor. However, the true efficiency will vary for several reasons. Inevitably, the thickness of the sensor will vary slightly over its area due to fabrication tolerances. Any window material or sensor metallization on the x-ray entrance side can decrease the system efficiency. Additionally, in the case of a partially-depleted silicon sensor, local variations in the depletion layer thickness will lead to variation in the efficiency. As will be discussed in Chapter 4, efficiency measurements at different photon energies can be a useful tool for debugging problems in fully depleting a thick silicon sensor.

The efficiency can be determined by comparing the signal recorded on the detector of interest with that recorded under identical illumination with a second, calibrated detector. The illumination source should be monochromatic, since the efficiency varies with energy. As such, it is appropriate at this juncture to make a few comments on the spectra of the sealed tube sources used for all of the calibration measurements discussed in this dissertation.

3.3.1 Spectral characterization of sealed tube sources

Throughout this work, copper and molybdenum anode sealed tubes were used as x-ray sources. When using a sealed tube source to approximate a monochromatic flood field of x-rays, the tube is biased above the Kα emission line of the anode material, and filters are used to cut out the Kβ line and reduce the low- and high-energy bremsstrahlung. The Kα lines for Cu and Mo are 8.0 keV and 17.5 keV, respectively.

A Vortex-90EX (SII NanoTechnology USA Inc, Northridge, CA) silicon drift detector (SDD) was used to measure the energy spectra of the sealed tube sources. The efficiency of the SDD sensor was determined experimentally by measuring the increase in recorded signal as the SDD was tilted with respect to the incoming beam, thus changing the apparent sensor thickness by a known factor. The SDD sensor thickness was calculated to be $287\ ^{+27}_{-29}\ \mu$m. Measured spectra are shown for the Mo and Cu tubes in Figures 3.1 and 3.2, respectively. The spectra measurements were taken using 25 μm zirconium and nickel filters, respectively; by correcting for the filter transmission and SDD efficiency, the true spectrum at the source can be computed, as can the expected spectrum after any other set of filters.

To assess the spectral purity of the source, the number of counts in the Kα line can be compared the the number of counts in the low- and high-energy bremsstrahlung. The low-energy band was defined as the band from 0 keV to 0.5 keV below the Kα line, and the high-energy band was defined as the band from 0.5 keV above the Kα line to the cutoff energy of the spectrum (determined by the tube bias voltage). These ratios are shown in Table 3.1 for both sources, using the filters most commonly used in this work. The Cu tube, biased at 15 kV

and with a 50 μm Ni filter, is a much more monochromatic source than the Mo tube biased at 25 kv with a 100-200 μm Zr filter. For the latter, the low-energy bremsstrahlung is particularly strong and difficult to filter efficiently.

	Cu 50 μm Ni	Mo 100 μm Zr	Mo 200 μm Zr
High-energy vs. Kα	0.028	0.068	0.01
Low-energy vs. Kα	0.038	1.092	0.60

Table 3.1: Ratio of low- and high-energy bremsstrahlung intensity versus Kα emission line intensity for Cu and Mo tube sources.

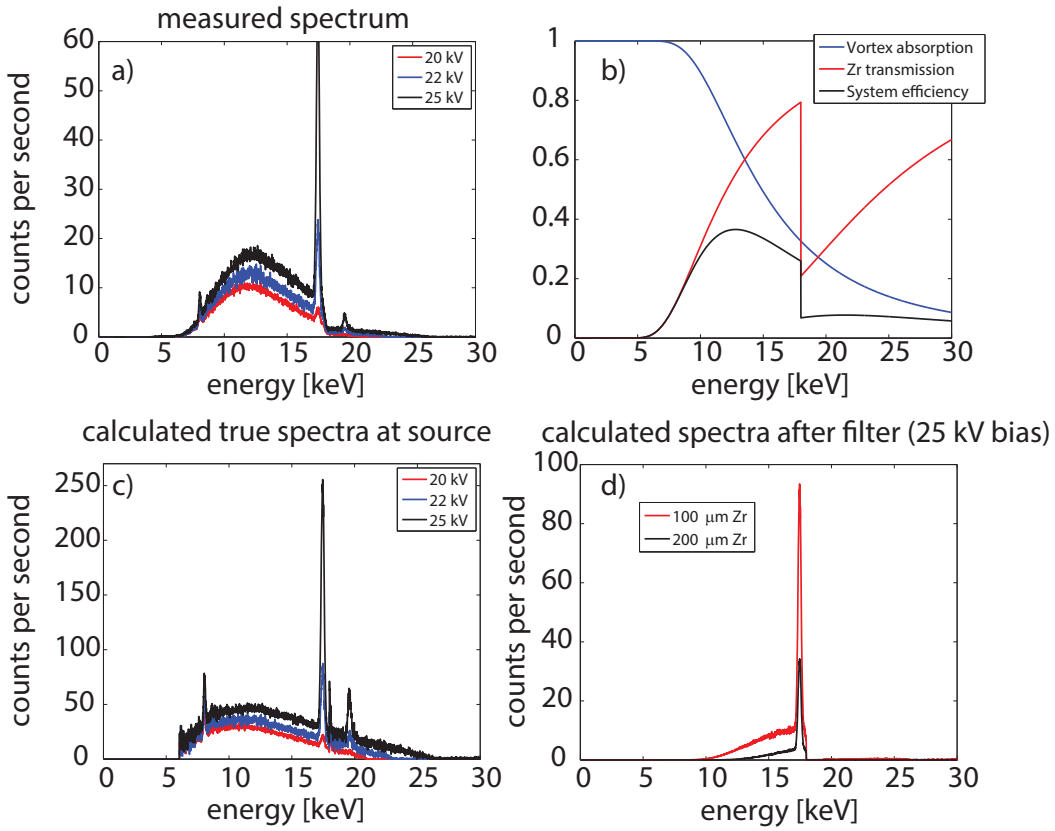

Figure 3.1: Measurements of the energy spectrum of the sealed source Mo tube. a) The spectra as measured by the Vortex SDD for 20, 22 and 25 V x-ray tube bias. In all cases, the tube bias current was 0.078 mA and a 25 μm Zr filter was placed directly in front of the source. b) The Vortex SDD absorption, Zr transmission and system efficiency plotted as functions of x-ray energy. c) The calculated true spectra at the x-ray source. d) The calculated spectrum expected after a 100 μm and 200 μm Zr filter, as used in many measurements elsewhere in this work.

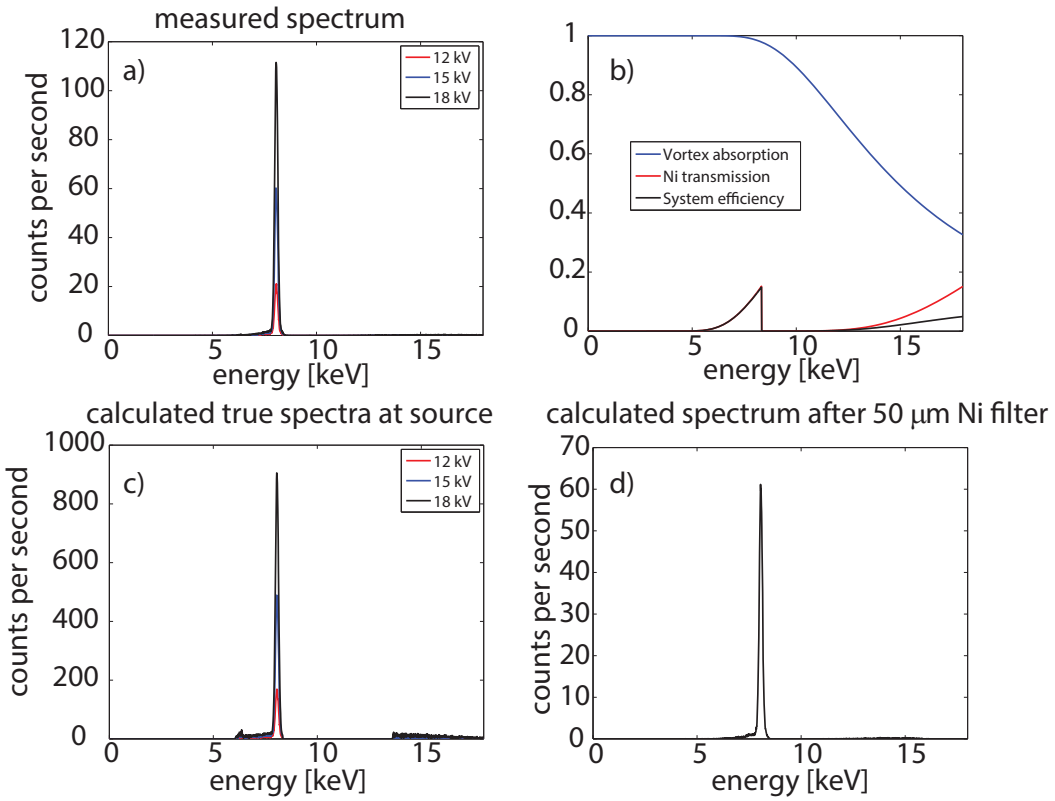

Figure 3.2: Measurements of the energy spectrum of the sealed source Cu tube. a) The spectra as measured by the Vortex SDD for 12, 15 and 18 V x-ray tube bias. In all cases, the tube bias current was 0.115 mA and a 25 μm Ni filter was placed directly in front of the source. b) The Vortex SDD absorption, Ni transmission and system efficiency plotted as functions of x-ray energy. c) The calculated true spectra at the x-ray source. d) The calculated spectrum expected after a 50 μm Ni filter, as used in many measurements elsewhere in this work.

3.4 Spatial resolution

The spatial resolution of an imager can be quantified by any of several related metrics: the edge spread response (ESR), line spread response (LSR), and point spread function (PSF). The PSF is frequently used in the synchrotron community and will be used most frequently in this dissertation.

The PSF is the impulse response of the imager; that is, given an image I, the measured image I_g is given by the convolution of I and the PSF:

$$I_g = I * \mathrm{PSF} = \int_{area} I(\xi, \eta)\mathrm{PSF}(x - \xi, y - \eta)\mathrm{d}\xi\mathrm{d}\eta \tag{3.4}$$

The LSR is the response of the imager to an infinitely thin line illumination, and is given by integral of the PSF:

$$\mathrm{LSR}(x) = \int \mathrm{PSF}(x, y)\mathrm{d}y \tag{3.5}$$

The ESR is the response of the imager to a step function illumination. The LSR is the derivative of the ESR:

$$\mathrm{LSR}(x) = \frac{d\mathrm{ESR}}{dx} \tag{3.6}$$

In practice, the ESR is often the easiest of the three metrics to measure experimentally. The ESR can be found directly by imaging a sufficiently sharp x-ray opaque knife edge. The knife edge measurement can either be done by scanning the knife edge across the detector face in sub-pixel steps, or by misaligning the knife edge from the pixel axis by a shallow angle, as described in [55]. Tilting the knife edge has the same effect as aligning the knife edge parallel to the direction of measurement and capturing frames at perpendicular translations of $p\sin(\theta)$, where p is the pixel pitch and θ is the angle by which the knife edge is tilted from the axis. This geometry is illustrated in Figure 3.3.

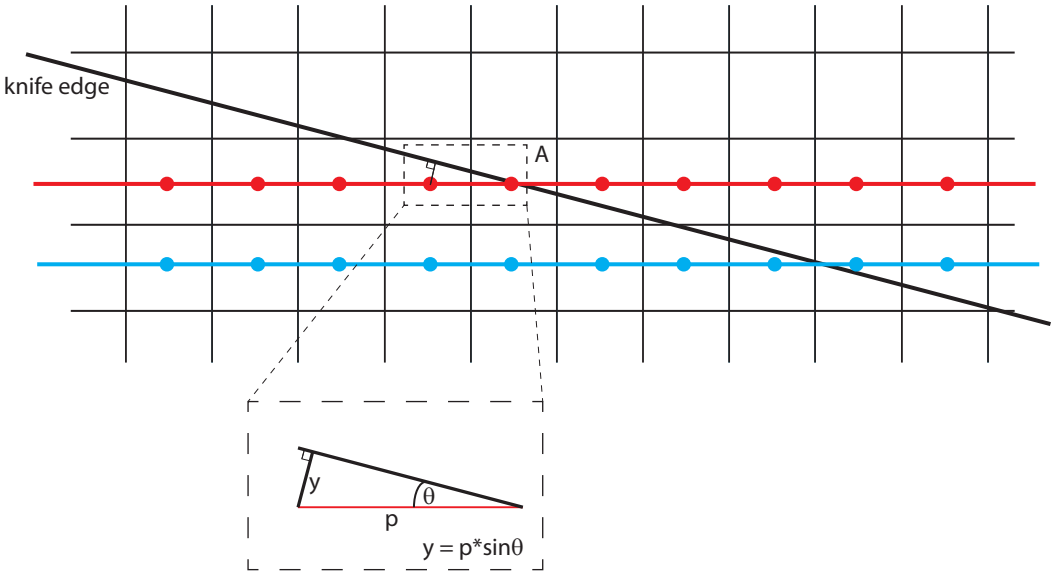

Figure 3.3: Illustration of the tilted knife edge measurement. The tilt of the knife edge is exaggerated for clarity.

While a sufficiently sharp knife edge can feasibly be fabricated and used for measuring the ESR, the LSR and PSF cannot be measured directly without significant effort in deconvoluting the shape of the x-ray source and the line or pinhole mask that would be imaged. Instead, as indicated above, the LSR can be found by differentiating the experimentally measured ESR. By definition this is equivalent to a one-dimensional slice through the PSF, and if the PSF is assumed to be isotropic, this gives a fairly good model of the PSF itself.

The PSF can also be measured experimentally by imaging a small pinhole, albiet with significant care taken to fully characterize the shape of the source and the pinhole. If the pixel size is sufficiently large and the PSF sufficiently small that signal from a single pinhole can be confined to a single pixel, then the pixel function must be deconvolved as well, leading to significant limitations to the quality of the analysis [46].

3.5 The photon transfer curve

The photon transfer curve (PTC) is a tool for determining the gain, read noise, and saturation value of an imager. It is most commonly used with CCDs and visible light, but can equally be applied to other imagers, such as PADs, and can be performed using monochromatic x-ray illumination. The following description follows from [39].

To construct the PTC, a series of images is taken over a range of integration times such that the average signal recorded per pixel spans from the read noise floor to the pixel full well depth. The average signal per pixel in a selected region of the detector is measured and plotted on a log-log scale against the standard deviation of the signal in that region, as shown in Figure 3.4. The curve should have three distinct regions:

- Low signal: standard deviation dominated by read noise; PTC is flat
- Mid range: Shot noise from the photon source dominates; slope of the PTC is 1/2
- High signal: Non-uniformity in pixel sensitivity dominates; slope of the PTC is 1

If the pixel full well depth is surpassed, the PTC levels off and, for CCDs, turns downward as blooming smooths out pixel-to-pixel variation in the region of interest.

Examination of the slope = 1/2 line provides a method for calculating the gain of the CCD. Let K be the electrons-to-ADU gain of the CCD and J be the

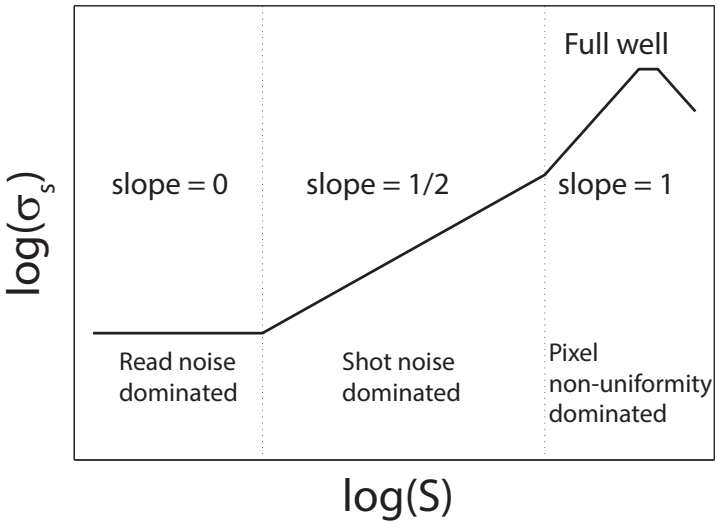

Figure 3.4: Ideal CCD photon transfer curve, showing the three expected regions. Adapted from [39].

photons-to-ADU gain. The signal recorded by a pixel, in units of ADU, is given by:

$$S = P \times QE \times \eta \times S_v \times A_V \times A_{ADC}. \tag{3.7}$$

where P is the number of incident photons, QE is the photon quantum efficiency (i.e., the number of stopped photons per incident photon, or the stopping power of the sensor), η is the quantum yield (i.e., the number of electrons per stopped photon), S_v is the sensitivity of the amplifier sense node (in units of volts/electron), A_V is the amplifier gain (in units of volt/volt), and A_{ADC} is the ADC gain (in units of ADU/V). The gains K and J are defined as:

$$K = \frac{1}{S_v \times A_V \times A_{ADC}} \tag{3.8}$$

$$J = \frac{1}{\eta \times S_v \times A_V \times A_{ADC}} \tag{3.9}$$

Analysis of the photon transfer curve is a way to numerically obtain J and K without knowing all of the quantities in equation 3.7.

For the purposes of explanation, consider the case where photons with en-

ergy below 3.1 eV are used, in which case each stopped photon produces only one electron and the calculation is simplified. This sets $\eta = 1$, and Equation 3.7 becomes

$$S = \frac{P_i}{K} \tag{3.10}$$

in which P_i is defined as $P \times QE$. The noise on S is given by

$$\sigma_S^2 = \left(\frac{\partial S}{\partial P_i}\right)^2 \sigma_{P_i}^2 + \left(\frac{\partial S}{\partial K}\right)^2 \sigma_K^2 + \sigma_R^2 \tag{3.11}$$

where σ_R^2 is the read noise variance. Assuming there is no variance in the gain K,

$$\begin{aligned} \sigma_S^2 &= \left(\frac{\partial S}{\partial P_i}\right)^2 \sigma_{P_i}^2 + \sigma_R^2 \\ \implies \sigma_S^2 &= \left(\frac{\sigma_{P_i}}{K}\right)^2 + \sigma_R^2 \\ \implies \sigma_S^2 - \sigma_R^2 &= \left(\frac{\sigma_{P_i}}{K}\right)^2 \\ \implies K^2 &= \frac{\sigma_{P_i}^2}{\sigma_S^2 - \sigma_R^2}. \end{aligned} \tag{3.12}$$

Assuming a Poisson source, $\sigma_{P_i}^2 = P_i$, thus

$$\begin{aligned} K^2 &= \frac{P_i}{\sigma_S^2 - \sigma_R^2} \\ \implies K^2 &= \frac{S \times K}{\sigma_S^2 - \sigma_R^2} \\ \implies K &= \frac{S}{\sigma_S^2 - \sigma_R^2}. \end{aligned} \tag{3.13}$$

K can now be found through examination of the slope = 1/2 region of the PTC. Since the noise in this region is dominated by the shot noise of the photon source, σ_R^2 can be neglected, and Equation 3.13 reduces to

$$\sigma_S^2 = \frac{S}{K} \tag{3.14}$$

If the PTC data is plotted as shown in Figure 3.4, K can be found by extending the slope = 1/2 line back to the x-axis. The x-intercept on the log-log plot is

where $\log \sigma_S = 0$, i.e. $\sigma_S = 1$; the equation then reduces to $K = S$. Alternatively, if the variance σ_S^2 is plotted on a linear scale against the signal, the data can be fit to a linear function with slope $1/K$.

If photons with energy greater than 3.1 eV are used, the method gives J instead of K. Alternatively, for a given energy J can be extrapolated from K if the number of electrons generated per stopped photon is known. This is the case for direct detection of x-rays in silicon, where each 3.6 eV of deposited energy yields, on average, one electron-hole pair.

3.6 Gain calibration using the discrete photon spectrum

In addition to the PTC method, the x-ray gain of a detector can also be measured by generating a histogram over many frames of photon hits in a specified area illuminated under low-flux conditions. The histogram is composed of a series of discrete photon peaks, corresponding to zero photon hits, one photon hit, and so on. The detector gain determines the spacing between the discrete photon peaks, and the read noise determines the peak width. An example spectrum, obtained for a single pixel in the MMPAD, is shown in Figure 3.5. This method is particularly useful for measuring the pixel-by-pixel gain variation in photon-integrating PADs, where x-ray pinholes can be used to isolate individual pixels, each of which has its own readout amplifier [46]. However, the method is equally applicable to CCDs, as will be shown in Chapter 4.

A gain map obtained by this method for the 2×3 MMPAD module is shown in Figure 3.6. The pixel gains are nearly uniform, with a mean of 10.8 ADU/8 keV photon, and varying by about 0.5% across the detector, with the exception

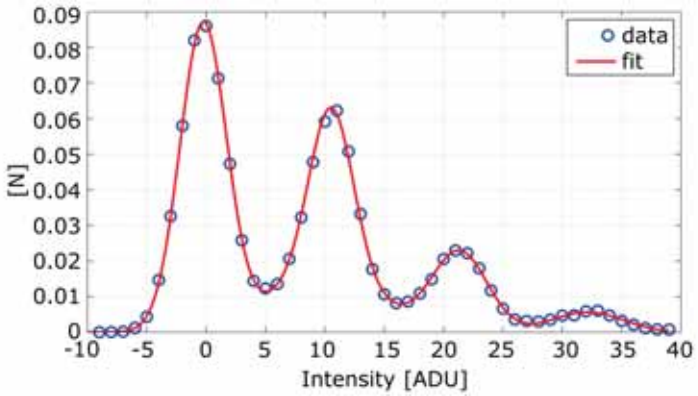

Figure 3.5: Photon spectrum recorded by one pixel over 130,000 8 ms frames. The fit shown is to a sum of 5 Gaussians: four corresponding to discrete photon peaks (including a peak corresponding to zero photons), and the fifth accounting for the heights of the valleys between peaks. The y-axis is normalized to the total number of frames represented. The negative ADU values arise from the background-subtraction process, in which pixels registering zero photons may record integrated dark current slightly above or below the corresponding value in the background frame.

of the upper right corner of the lower middle chip, which is systematically low in the gain map as well as in the flood field (Figure 3.6(b)). Normalizing the flood field by the computed gain removes this feature.

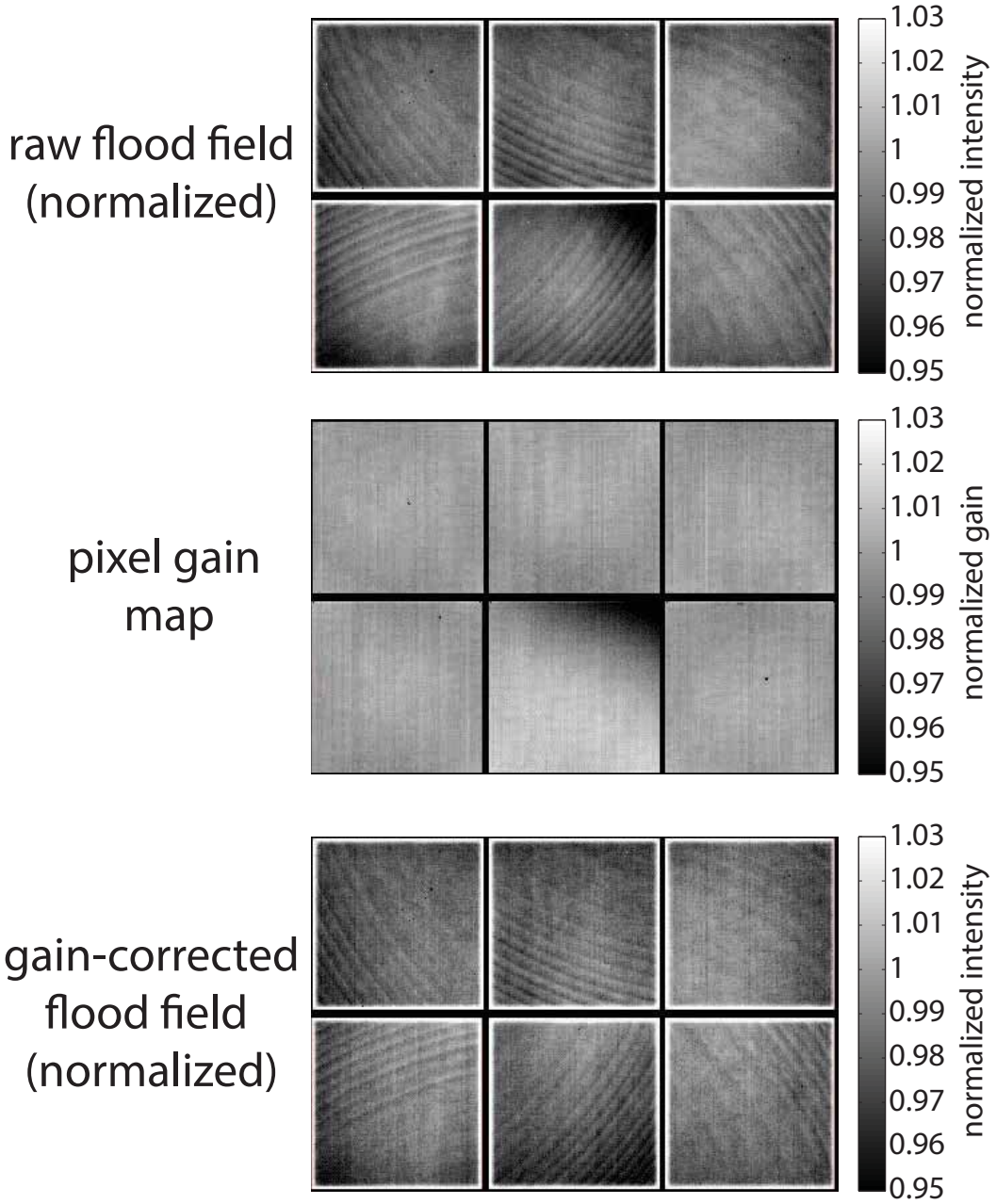

Figure 3.6: Top: background-subtracted flood field collected on the 2 × 3 MMPAD using 8.0 keV x-rays. Center: Map of pixel-by-pixel gain on the 2 × 3 MMPAD. Pixels where the gain calibration failed have a value of 0 in this map and appear as isolated black spots. Bottom: The effect of gain correction on a flood field image. In addition to gain variation effects, striations ("tree rings") due to doping inhomogeneities, described in Section 3.7, are evident.

3.6.1 Energy thresholding

The ability to resolve individual photons in a low-noise integrating detector opens up the possibility of performing energy thresholding as a post-processing step. This has the potential to improve the fidelity of low-signal measurements while maintaining the high-flux capabilities of integrating detectors. As an illustrative example, a discrete photon spectrum from data collected during an experiment at CHESS beamline A2 is presented in Figure 3.7. In this experiment[2], the dynamics of reactive metal foils were studied *in situ* by capturing 2 ms frames on the MMPAD before, during and after the initiation of a run-away thermal reaction. Similar experiments using an earlier-generation PAD are described in [56].

The short exposure time was necessary to capture the sample dynamics, but lead to low signal per frame. The photons from the undulator source were 15 keV, but the samples also produced significant nickel fluorescence at 7.5 keV. Figure 3.7 is the histogram of all pixel values recorded in a single frame. Peaks at 10 and 30 ADU per pixel correspond to one and three 7.5 keV photons per pixel, respectively; peaks at 20, 40 and 60 ADU per pixel correspond to one, two and three diffracted 15 keV photons per pixel. The 20, 40 and 60 ADU peaks may also contain small contributions from pixels registering two, four and six 7.5 keV photons, respectively.

The separation between the first two peaks allows single-photon fluorescence rejection to be carried out in software as a post-processing step. All pixels registering 15 ADU or less could be set to zero, thresholding out both single-photon fluorescence hits and the read noise in pixels with zero photon hits.

[2]In collaboration with the Todd Hufnagel group at Johns Hopkins University.

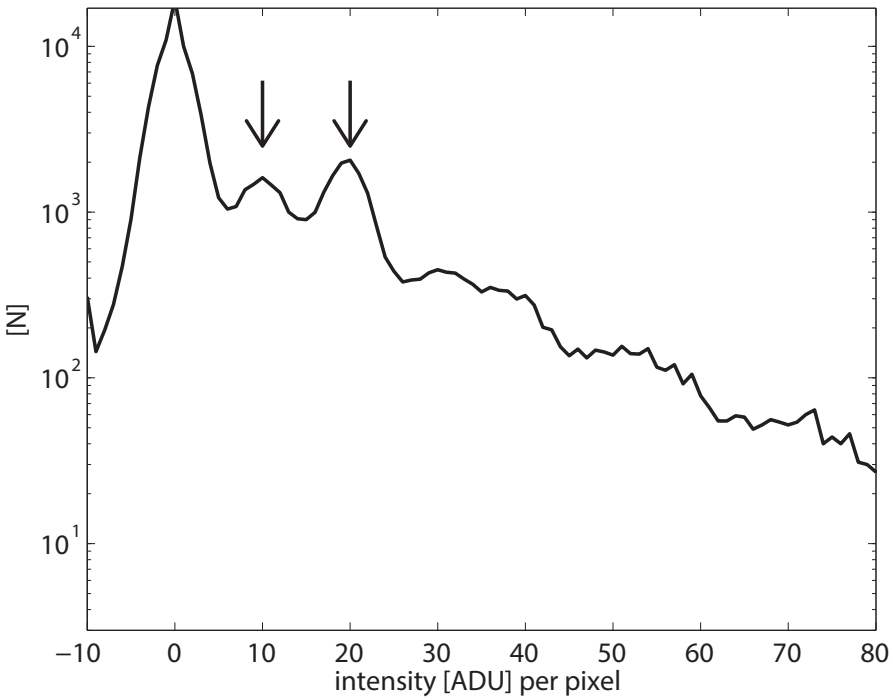

Figure 3.7: Photon spectrum from the full 2 × 3 MMPAD module from one 2 ms frame taken at CHESS A2 station during a reactive foil experiment. Distinct peaks are seen for both 15 keV (arrow, right) diffracted photon and 7.5 keV (arrow, left) nickel fluorescence from the sample.

Read noise from these pixels would be excluded from any intensity sum (for example, integrating the intensity in a diffraction ring), improving the SNR of the sum. However, this does come at the expense of throwing away 15 keV photon hits that are split between two or more pixels. Because the proposed thresholding is a post-processing step, the user can decide whether to prioritize fluorescence rejection or the preservation of all diffracted photons.

3.7 Area distortions

Radial resistivity variations on the order of 20% are typical in high-resistivity float-zone silicon [42]. The resistivity variation is due to doping inhomogeneities in the boule from which the wafer is cut, which are in turn caused by convection patterns that form when portions of the boule are melted during refinement [38]. The doping inhomogeneities produce lateral fields that deflect charge as it traverses the diode, altering the effective collection area of a given pixel. This results in a "tree ring" pattern in areas of nominally flat illumination, as illustrated in the MMPAD flood field shown above in Figure 3.6 and in the next chapter for the STA3200 CCD. This effect is seen in practically all other area detectors based on thick, high resistivity silicon sensors, including silicon drift detectors on both float-zone silicon [57] and neutron transmutation doped silicon [58], [59], [60], pixel array detectors with sensors made from float-zone silicon [61], [46], [53], and other deep-depletion CCDs fabricated on float-zone silicon [62].

All of the detectors referenced above, with the exception of the STA3200, are run fully- or over-depleted, in which case the tree rings can be fully attributed to lateral area distortions. If a sensor is underdepleted, local variations in resistivity will lead to variations in the depth of the depletion region. This will result in variation in efficiency, in addition to the lateral pixel area distortion. This effect has been observed in studies of the Medipix photon-counting PAD [61] and the STA3200 CCD discussed in Chapter 4.

In an overdepleted sensor, because the amount of lateral deflection depends on the strength of the transverse electric field compared to the lateral fields, the

tree ring amplitude decreases as the bias voltage used to deplete the diode is increased. Additionally, the distortion depends on the x-ray conversion depth, and thus on the photon energy, as charge carriers generated at the top of the diode will be deflected onto different paths than those generated near the bottom [46]. It has been the experience of the Cornell detector group that pixel areas are distorted by 1-5% in 300-600 μm thick diodes.

Area distortions cannot be corrected for by a multiplicative factor, which would treat the distortions as a variation in gain. The appropriate correction is a re-distribution of charge between neighboring pixels, wherein the total signal on a chip is preserved. To construct the re-distribution map, an accurate measure of the pixel boundaries must be determined.

In the past, flood field images have been used to generate maps of pixel boundary variations via an adaptive filtering algorithm [46]. However, there is insufficient information in a flood field image to directly decouple gain variations from area distortions, so the solutions generated by this method tend to be non-unique. To illustrate this problem, consider the following model: each pixel is ideally a square with side length w, but in reality is distorted due to lateral electric fields within the diode. For simplicity, suppose that the effective pixel areas are rectangular, and express the amount by which each pixel boundary is displaced from its ideal location as a fraction α of w, as in Figure 3.8 (so α_l applies to the left edge of the pixel, α_r to the right, etc.). Note that by this convention all α's are defined to be non-negative.

Assume a constant flux F (units: photons/unit area) across the detector face, as in a flood field measurement. Then the signal measured by pixel (i, j) can be

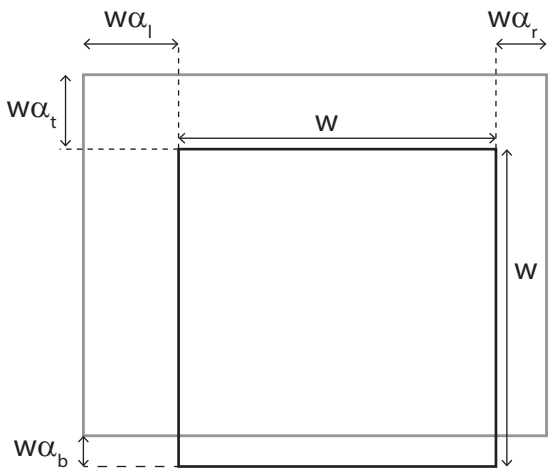

Figure 3.8: Rectangular model of pixel area distortion. Ideal pixel boundaries are shown in black; effective boundaries in grey.

written as:

$$\begin{aligned} I_{ij} &= FA_{ij} \\ &= F(w \pm w\alpha_{t,ij} \pm w\alpha_{b,ij})(w \pm w\alpha_{r,ij} \pm w\alpha_{l,ij}) \\ &= Fw^2(1 \pm \alpha_{t,ij} \pm \alpha_{b,ij})(1 \pm \alpha_{r,ij} \pm \alpha_{l,ij}) \end{aligned} \tag{3.15}$$

where +/- is chosen for each term to be + if the pixel's area is increased in the relevant direction and - otherwise. Pixel (i, j)'s signal can be normalized to the average signal over all pixels, $< I >= Fw^2$:

$$I_{ij,norm} = \frac{I_{ij}}{Fw^2} = (1 \pm \alpha_{t,ij} \pm \alpha_{b,ij})(1 \pm \alpha_{r,ij} \pm \alpha_{l,ij}). \tag{3.16}$$

An image with R rows and C columns of pixels has $N = RC$ such equations. Interior pixels each have four nearest neighbors, but since α's for shared edges are not independent, and pixels at the edges and corners of the array have fewer than four nearest neighbors, there are fewer than $4N$ unknown variables. Figure 3.9 provides a visual aid for the following discussion.

If the edges of the pixel array are assumed to be fixed, there are $C - 1$ vertical edges in a row, and R rows, giving $R(C - 1)$ vertical edges across which charge

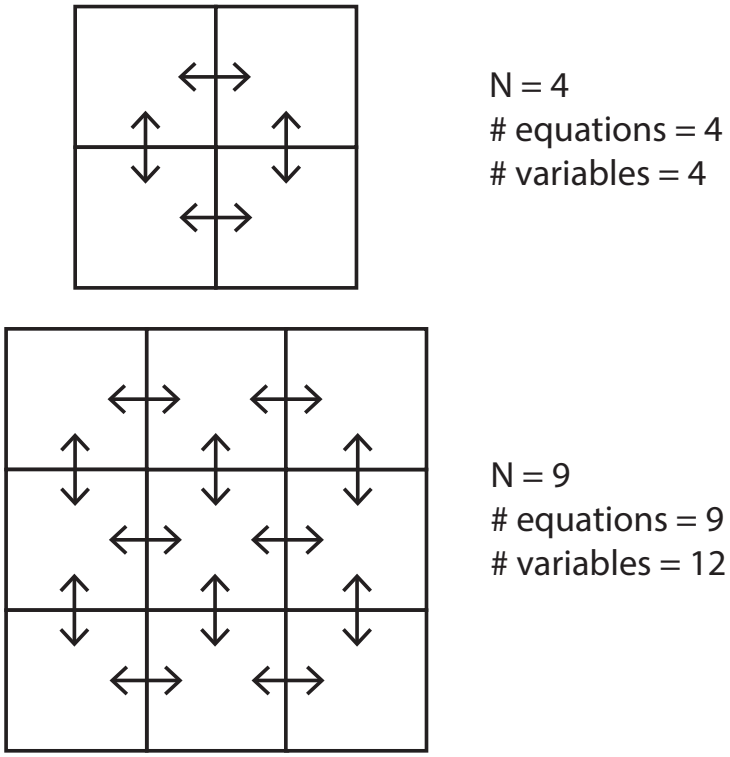

Figure 3.9: Aid to counting the number of unknowns for a given number of pixels N (only square configurations are shown for simplicity). Edges of the pixel array are assumed to be fixed and only nearest neighbors share charge. Each arrow indicates a pixel boundary that can move.

can pass. Similarly, there are $R-1$ horizontal edges in a column, and C columns: $C(R-1)$ horizontal edges across which charge can pass. This gives $R(C-1)+C(R-1)$ variables. We wish to determine whether there exist some R, C for which the number of variables is less than or equal to the number of equations:

$$\begin{aligned} \text{variables} &\leq \text{equations} \\ \Rightarrow R(C-1)+C(R-1) &\leq RC \\ \Rightarrow 2RC-(R+C) &\leq RC \\ \Rightarrow RC &\leq R+C \end{aligned} \tag{3.17}$$

The only positive integer solutions to this equation are: $R = C = 1$; $R = C = 2$; either R or $C = 1$ but not both (i.e., a strip detector).

In fact, the edges of the pixel array may not be fixed, because edge pixels can potentially collect charge from the region of the sensor that falls over the guard ring, outside of the nominal imaging array. This effect is seen strongly in the 2×3 MMPAD, for example in Figure 3.6, where the edges of each chip are particularly bright compared to the rest of the imaging pixels. In this case, the intensity of pixel (i, j) is again described by Equation 3.15, but since the imaging array is extended beyond its nominal boundaries by an unknown amount, the average pixel signal may be greater than Fw^2. However, even if the flux incident on the detector were known independently, there would still be more variables than can be uniquely determined from a flood field image. There are now $C + 1$ moveable vertical edges in a row, across R rows: $R(C + 1)$ vertical edges across which charge can pass. Similarly, there are $R + 1$ horizontal edges in a column, across C columns: $C(R + 1)$ horizontal edges across which charge can pass. This gives $R(C+1)+C(R+1)$ variables. Again, we can check if the number of variables is less than or equal to the number of equations:

$$\begin{aligned} \text{variables} &\leq \text{equations} \\ \Rightarrow R(C+1) + C(R+1) &\leq RC \\ \Rightarrow 2RC + R + C &\leq RC \\ \Rightarrow RC &\leq -(R + C) \end{aligned} \tag{3.18}$$

which has no solution for positive integer R, C.

Thus, in a rectangular-pixel model where charge is only shared between nearest neighbors, the problem is undetermined (using only flood field data) for any area detector other than a 2×2 pixel chip with fixed edges. With insufficient information in a flood field image to accurately determine pixel boundary displacements, an independent measurement of each pixel boundary location

is needed. This requirement spurred the development of the following pinhole scan technique.

To measure the pixel boundaries in an efficient manner, the detector is scanned across an array of pinhole spots. The pinhole diameter is chosen to provide good isolation of a single pixel; for example, for the MMPAD, with a nominal pixel size of 150 μm $\times$ 150 μm, a 75 μm pinhole provides a good compromise between single-pixel isolation and flux through the pinhole. The pinhole pitch should be sufficiently large that neighboring pinholes never illuminate neighboring pixels. The mask is placed as close to the detector entrance window as possible to minimize parallax. The mask is then flood illuminated from a monochromatic source.

To measure the effective pixel widths in x or y, the mask is centered in y or x, respectively, and translated in sub-pixel-width steps across the detector face in the desired direction. A step size one-tenth of the nominal pixel width provides a compromise between resolution and time required to complete a scan. The total exposure time at each scan step is chosen to yield the desired Poisson-limited accuracy.

Example pinhole crossings for the 2 $\times$ 3 MMPAD are shown in Figure 3.10 for two neighboring pixels. This data was collected using 8.0 keV x-rays. The rising and falling edges of each pinhole crossing are identified and each is fit to a sigmoid function,

$$y = \frac{a}{1 + e^{-b(x-c)}} \tag{3.19}$$

where y is the signal recorded in the pixel at position x, c is the crossing midpoint (i.e., the pixel boundary), a is the average signal recorded when the pinhole is isolated on the pixel, b determines the steepness of the boundary crossing. Note

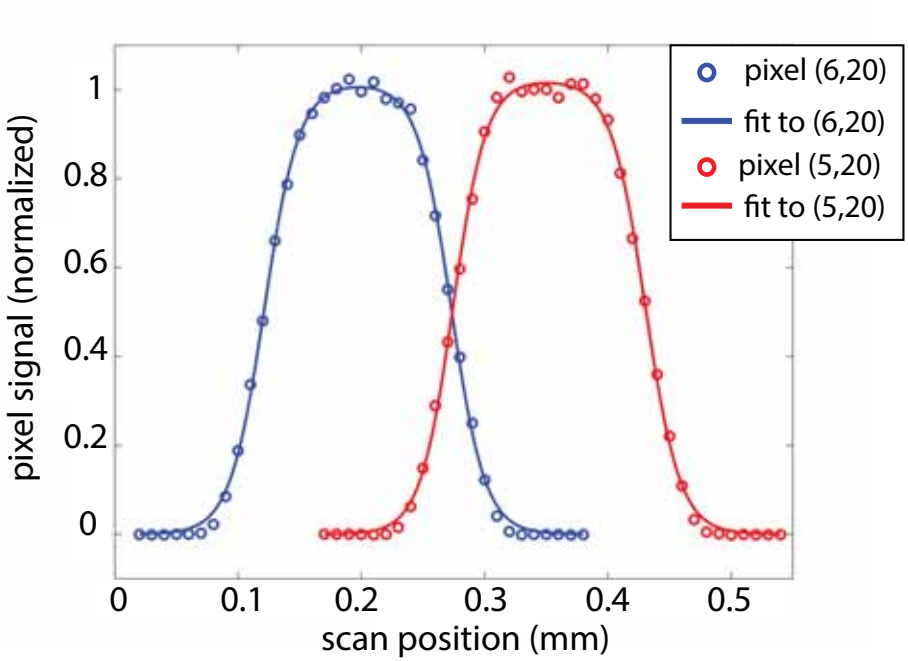

Figure 3.10: Pinhole crossing fits for two neighboring pixels on the 2 × 3 MMPAD.

that b must be positive for a rising edge and negative for a falling edge. In practice, to simplify the curve-fitting procedure, two equations of this form can be mutliplied together to fit the complete pinhole crossing at once:

$$y = \frac{a}{1 + e^{-b_{RE}(x - c_{RE})}} \frac{a}{1 + e^{-b_{FE}(x - c_{FE})}} \tag{3.20}$$

where the subscripts "RE" and "FE" refer to the rising and falling edges of the pinhole crossing, respectively. Maps of computed pixel areas obtained during calibration of the 2 × 3 MMPAD, and of the older, single-chip MMPAD, are shown in Figures 3.11 and 3.12, respectively.

As can be seen in the "raw" area maps, the pixel areas as computed directly from the fits are grainy, especially near the chip edges. This effect is more pronounced in the single-chip MMPAD area map, where a checkerboard pattern is faintly visible in the raw area map, especially in the lower left quadrant of

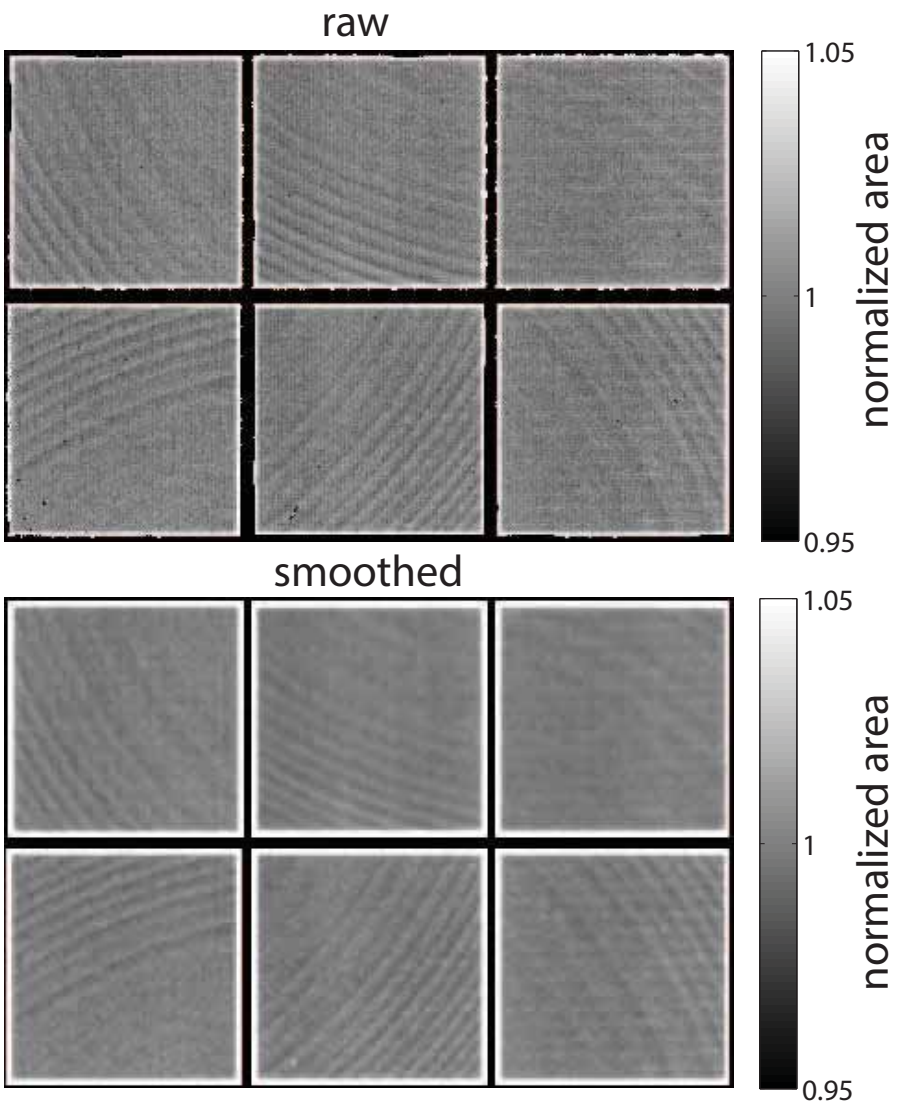

Figure 3.11: Computed area map for the 2 × 3 MMPAD. The "raw" area map, computed directly from the pinhole crossing fits, is shown at top. The area map with a running average filter is shown at bottom. The area map closely resembles the tree ring pattern visible in the flood field collected on the same detector, shown in Figure 3.6.

the chip. This is likely an artifact due to inaccuracy in the motion of the translation stages used during the pinhole scans. For efficiency, the pinhole scans were done using a mask with pinhole spacing about twice that of the detector pixel pitch, so that on average every other pinhole in a row or column is illu-

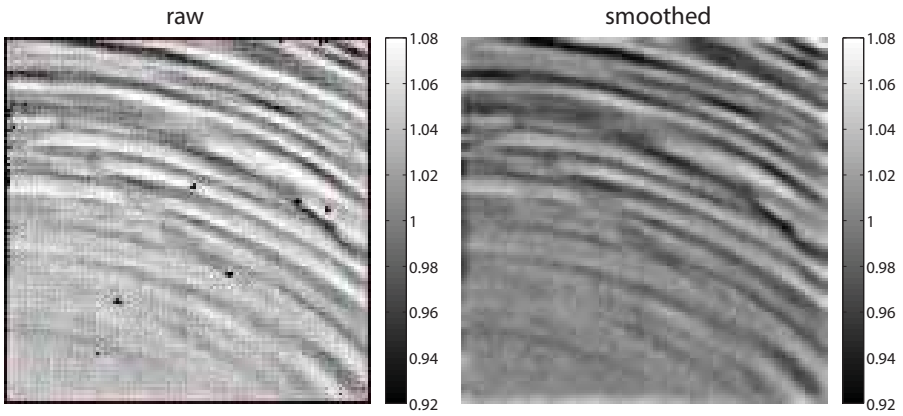

Figure 3.12: Computed area map for the single-chip MMPAD. The "raw" area map, computed directly from the pinhole crossing fits, is shown at left. The area map with a running average filter is shown at right.

minated at a given mask position. Consider a pinhole being stepped across a pixel boundary with nominal step size s. During the curve-fitting procedure, the position corrdinate x is computed from the nominal step size, rather than read back from the motor. Now suppose that during one of the steps, the motor moves by a slightly larger distance $s + \delta_s$. This will result in an inaccuracy in the position coordinate x, and the crossing point (c in Equation 3.19) will be shifted slightly from the true value. The computed width for one pixel will be slightly enlarged while its neighbor is contracted. Since the mask is rigid and the pinholes fall on every other pixel, a checkerboard pattern emerges.

A running average can be applied to the computed pixel widths and heights to smooth out these variations. A window size w is chosen, and each data point (a pixel width or height) is replaced by the average of all data points within that window:

$$y(x_i) = \frac{y(x_{i-w}) + ... + y(x_i) + ... + y(x_{i+w})}{2w + 1} \tag{3.21}$$

The effect of this filter is shown in the "smoothed" area maps, where a window size of 1 pixel was used. Depending on the severity of the scan artifacts, this

procedure may or may not be desirable, since some fine spatial resolution is sacrificed.

Approximating the pixels as rectangular, the overlap between a pixel and the nominal collection regions of each of its eight neighbors can be calculated. Then, to correct an image, a corresponding fraction of a pixel's signal is shuffled to/from each neighbor. This procedure degrades the spatial resolution slightly. Alternatively, software packages designed to work with distorted images could use the pixel boundary map directly.

The effect of the charge-shuffling correction method is illustrated in Figure 3.13. The single-chip MMPAD was used to collect small-angle x-ray scattering (SAXS) data from carbon nanotube (CNT) forests during and after growth[3], at CHESS beamline G1. The frame shown is a grazing-incidence SAXS pattern collected from a sample after the growth of the CNT forest. Because of the continuous nature of the scattering features (as opposed to the discrete features found in a pattern of diffraction spots), the tree ring distortions are particularly obvious in the original data. By measuring the locations of the pixel boundaries as described above, calculating the overlaps and redistributing the recorded signal accordingly, the tree rings were successfully removed from the corrected image. In this case, the smoothed area map was used. The correction was also performed using the raw area map. The difference between the resulting corrected images was imperceptible to the eye at the contrast level used here. As such, only the corrected image using the smoothed map is shown.

[3]In collaboration with the John Hart group from the University of Michigan Department of Mechanical Engineering.

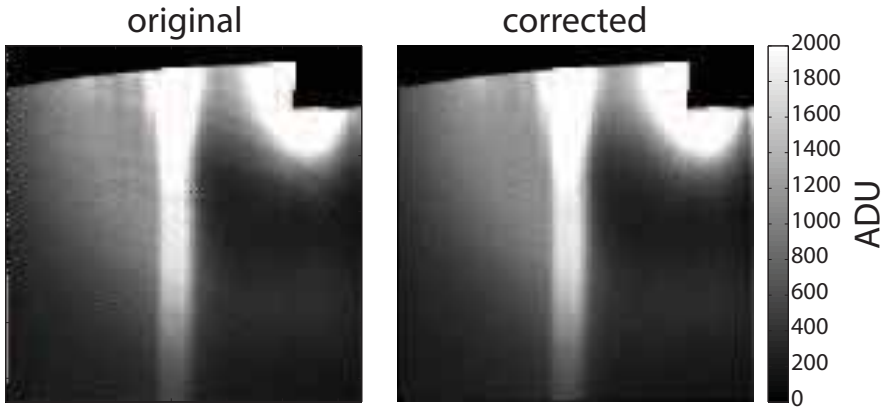

Figure 3.13: Pixel area correction demonstrated on grazing-incidence SAXS data collected on the single-chip MMPAD.

3.8 Impact on data quality

As important as accurate calibrations are, calibration data can be extremely time-consuming to collect and process, especially in the case of calibrating pixel-by-pixel gain and area. It can also be cumbersome to apply correction algorithms to every image gathered by the detector during normal operation. Therefore, consideration should be given to whether a given calibration is well-suited to the targeted scientific data.

To illustrate some potential issues with matching a calibration procedure to various, qualitatively different datasets, the findings of one of the early papers on phosphor-coupled CCDs [63] are summarized here. In this case, the detector under study was a phosphor-coupled CCD with 50 μm $\times$ 50 μm pixels and a point spread FWHM of 80 μm. A pixel nonuniformity correction generated from flood field data more successfully corrected images containing large features than small, isolated ones. This is due to the fact that the point spread affects small, isolated features differently than large and/or continuous features. For large features, such as a flood-illuminated patch or a large pinhole

or diffraction spot, pixels inside the illuminated area contain contributions from their neighbors due to the point spread. In contrast, an isolated point-like feature has no such smoothing contributions. Because the flood-field-generated nonuniformity correction inherently includes smoothing from the point spread, the isolated features are not as well corrected as larger, continuous features. In the cited case, the difference was a correction to 1% for 75 μm spots versus 0.3% for 300 μm spots.

Finally, while this chapter has focused on calibrations related to fundamental issues with the sensor and pixel readout amplifier, in practical settings it has been my experience that the more pressing corrections to apply are those related to quirks of individual *cameras*; that is, the detector along with its support electronics, which themselves contribute noise and systematics. For example, the photon-integrating pixel array detectors considered here exhibit a frame-by-frame, chip-by-chip common mode pedestal variation that can not only distrub users viewing the raw data, but also completely drown out very-low-flux signal. The pedestal variation is illustrated in Figure 3.14, which shows six consecutive background-subtracted frames from the reactive foil experiment described in Section 3.6.1.

This pedestal variation is believed to be due to some component in the support electronics chain, and is quite signficant for the 2×3 MMPAD module. Yet this detector has been successfully used in a range of experiments involving the collection of low-flux data by part or all of the detector. Examples include the pixel-by-pixel gain measurements described in Section 3.6, the time-resolved studies of reactive foils described in Section 3.6.1, ptychographic image reconstruction [64], and a rotating anode expectation-maximization image re-

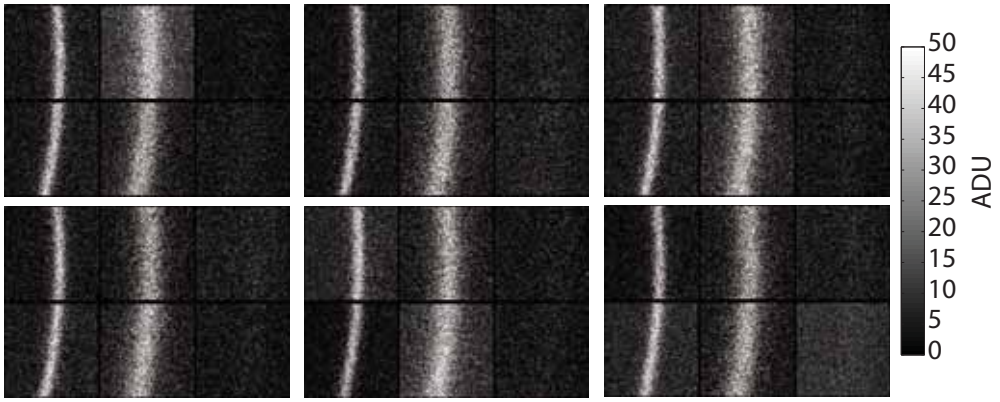

Figure 3.14: Frame-by-frame, chip-by-chip pedestal variation in the 2×3 MM-PAD.

construction experiment [65]. The ability to successfully analyze these datasets has depended on the application of a pedestal-correction algorithm, as will be illustrated below using data from the reactive foil experiment as an example.

To evaluate the pedestals, the average signal recorded by pixels receiving zero photon hits is evaluated for each chip in each frame. To do so, the signal in pixels that are unconnected from the sensor (either by design or through a bump-bonding failure) can averaged in each frame; or, if no such pixels are available, pixels recording zero photon hits can be identified in an automated manner by histogramming all pixel values per chip per frame and identifying the lowest peak (recalling the discrete photon specturm method from section 3.6), as shown in Figure 3.15. The pedestals are then subtracted from a pixels in the corresponding chip and frame. The effect of this correction is illustrated in Figure 3.16, which shows the set of frames from Figure 3.14 after pedestal correction.

It is worth noting that the tree ring distortions are not evident to the eye in the raw or corrected data from the reactive foil experiment. The detector is the

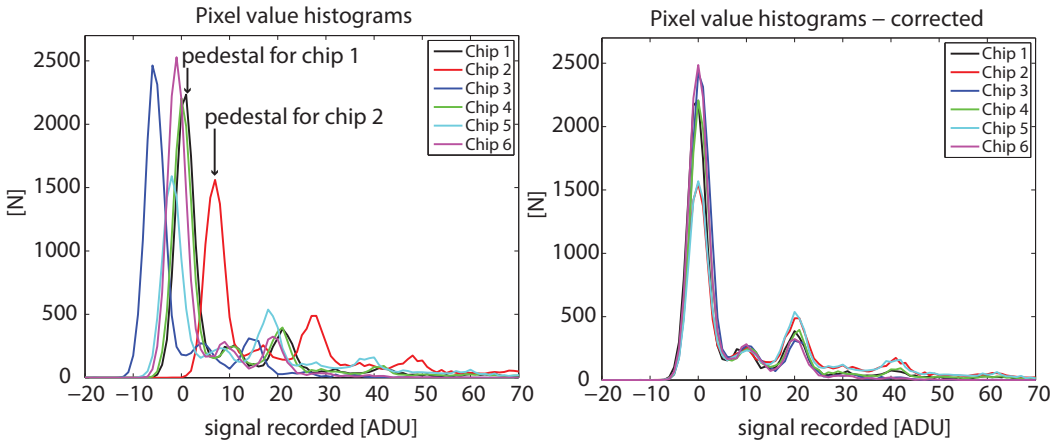

Figure 3.15: Chip-by-chip pixel histogram for the first frame in Figure 3.14, showing pedestal variations. At left, all pixel values in each chip are histogrammed separately. The pedestals for chips 1 and 2 are indicated for reference. The pedestals range from about -10 to 10 ADU. At right, the pixel histograms are shown for the same frame after the pedestal correction is applied.

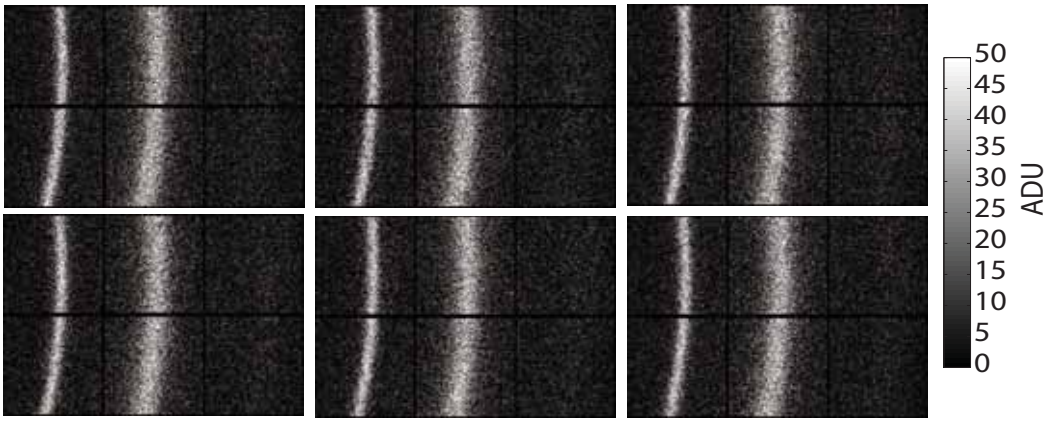

Figure 3.16: Effect of the pedestal correction on MMPAD data.

exact same unit as was used to collect the flood field shown in Figure 3.6 and the area distortion map shown in Figure 3.11. The pixel area distortions are present in the sensor, but in this case they do not significantly affect the recorded data, which does not contain the kind of continuous features present in the SAXS data in Figure 3.13. The reactive foil data is an example of a dataset which does not particularly need the pixel area correction, but which absolutely does require the pedestal correction.

CHAPTER 4

THE STA3200 DIRECT-DETECTION CCD

4.1 Introduction

As we have argued, direct-conversion silicon area detectors, in which x-rays are absorbed in a silicon sensor, are excellent devices for synchrotron science due to their high spatial resolution and to the large number of charge carriers generated per incident x-ray. This leads to a high single x-ray signal-to-noise ratio (SNR) when compared to indirect detection methods, such as phosphor coupling, in which x-rays are stopped in a phosphor that is optically coupled to a conventional CCD that records the resultant visible light. Much detector development has focused on PADs of either the x-ray integrating or x-ray counting variety. However, the pixel size of a PAD is constrained by the need to fit a large amount of signal processing and readout circuitry into each pixel. Typical PAD pixel sizes range from 55 μm $\times$ 55 μm in the Medipix chip [66] to 172 μm $\times$ 172 μm, for the PILATUS [47]. In comparison, the point spread function in a thick, over-depleted silicon sensor is dominated by the diffusion of charge carriers and can have a full-width half maximum (FWHM) of less than 50 μm, as will be discussed below. Therefore, fabrication of a traditional CCD structure on thick, high-resistivity silicon gives a closer match between pixel size and the underlying spatial resolution of the sensor.

Direct-detection CCDs for astronomy, as well as synchrotron and x-ray free electron laser (XFEL) science, have been and are currently being developed, typically with 50-450 μm thick depletion regions [67, 28, 68]. The device described in this chapter is a deep-depletion, backside-illuminated x-ray CCD fabricated

on 600 μm thick high-resistivity silicon. It has an imaging area of 96 mm $\times$ 96 mm, which is about the maximum size that can be cut from a single 6-inch silicon wafer. Results from device characterization are presented.[1] Results from a protein crystallographic experiment using this device will be presented in Chapter 5.

4.2 Design overview

The CCD described here, the STA3200, was designed and custom built by Semiconductor Technology Associates, Inc. (STA; San Juan Capistrano, CA). The wafer processing was done by Teledyne DALSA (Waterloo, Ontario, Canada) in a standard NMOS buried channel triple poly/double metal CCD process. To improve the pixel well depth, the channel doping concentration was increased (the exact doping concentration is information proprietary to STA). Readout is controlled by 4-phase parallel registers, clocked at 300 kHz, and 3-phase serial registers, clocked at 5 MHz. The parallel registers have metal strapping to mitigate the high RC constant of the polysilicon gates, which can hinder performance at high speeds. The serial register is widened to increase the binned well depth and can accommodate almost twice the single-pixel full well. There are 8 output amplifiers on the top and bottom edges, for a total of 16. A frame can be read out either in a split-frame configuration through all 16 ports, or through the 8 ports on either side, as shown in Figure 4.1. A defect in one amplifier on the current chip makes 8-port readout necessary in order to capture the full imaging area. The detector was operated in full-frame mode with 8-port readout in all measurements described here.

[1] Parts of this work have been published in Journal of Applied Crystallography [69].

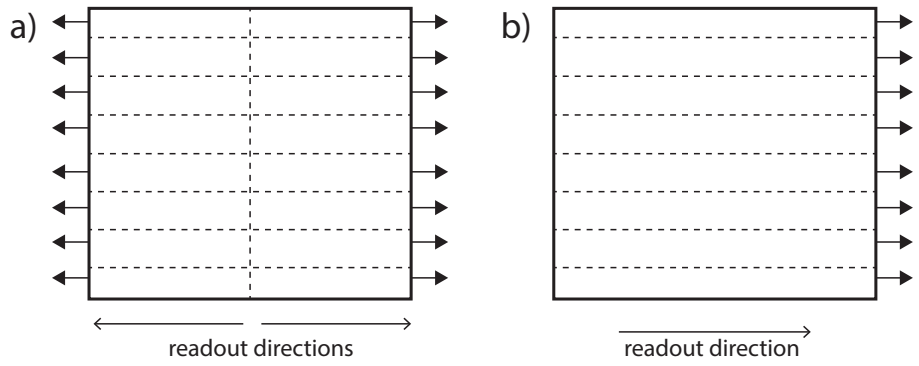

Figure 4.1: 16-port vs. 8-port readout for the STA3200. The sections of the detector read out through each port are delineated by dashed lines.

The diode structure is sketched in Figure 4.2. The 600 μm thick silicon should provide 84% efficient X-ray stopping power at 13.5 keV. The material is p-type float-zone silicon and has a resistivity of ≥10 kΩ-cm, as stated by the manufacturer. It was found that the clock feed-through noise could be significantly reduced by gating the reverse bias such that the full bias is only applied during the integration period, gating it off during readout. The device is intended to be run with a reverse bias (V_{BB}) sufficiently large to over-deplete the sensor. Initial testing by STA showed full depletion at 300-325 V reverse bias as evidenced by the single photon response of x-rays from a weak ^{55}Fe source. (^{55}Fe is a radioactive isotope that produces 5.9 keV x-rays and is frequently used to test the single-photon response and charge transfer efficiency of CCDs.) After these initial tests, the onset of electrical breakdown was observed at a reverse bias of 170 V and the CCD could no longer be operated in full depletion. The cause appears to be damage to the electrical guard ring structure on the surface of the CCD. Therefore, unless otherwise noted, the measurements described were carried out at a reverse bias of 155 V.

A 300 V minimum depletion bias would correspond to a resistivity of approximately 11.4 kΩ-cm. At this resistivity, a reverse bias of 155 V would de-

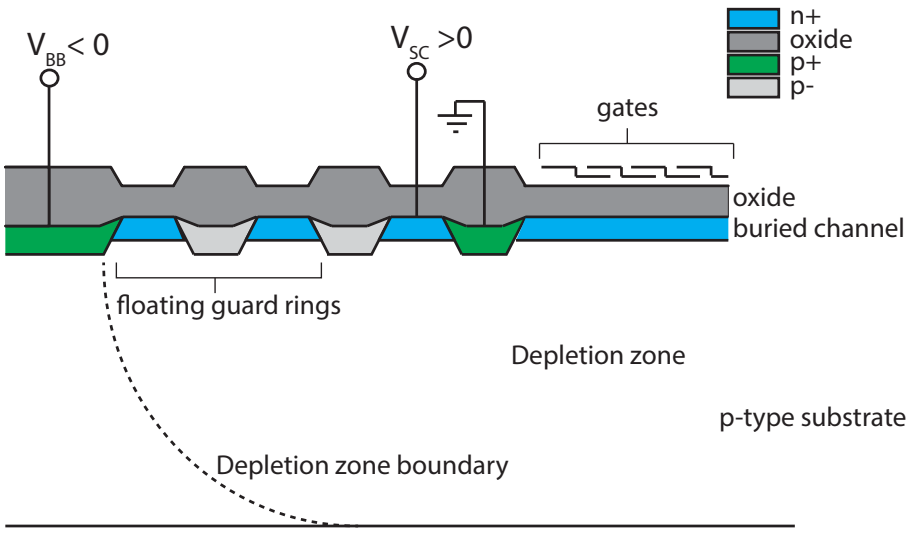

Figure 4.2: The STA3200 diode structure. X-rays enter from the back side (shown at the bottom). The prototype includes eight floating guard rings; fewer are shown for simplicity.

plete a 430 μm thickness within the wafer, leaving a 170 μm thick undepleted region at the x-ray entrance side. Having an undepleted region will affect both the efficiency and the resolution, as discussed below.

The chip is cooled to 205 K using a Cryotel closed-cycle cryocooler (Sunpower, Athens, OH). The x-ray vacuum window of the detector consists of a 0.79 mm thick epoxy-carbon fiber fabric. Although the window absorption lowers the system efficiency to 72% at 13.5 keV, the window was inexpensive and served well for the testing purposes of this report. However, the carbon window attenuates lower energies more severely, as shown in Figure 4.3 and should be replaced with a beryllium window for use with lower energy x-rays.

The detector is controlled over a CameraLink interface. Signals sent over CameraLink from the control computer are relayed through a backplane to a set of bias, clocking and A/D printed circuit boards. Both continuous framing and immediate trigger modes are provided. The trigger can be provided through

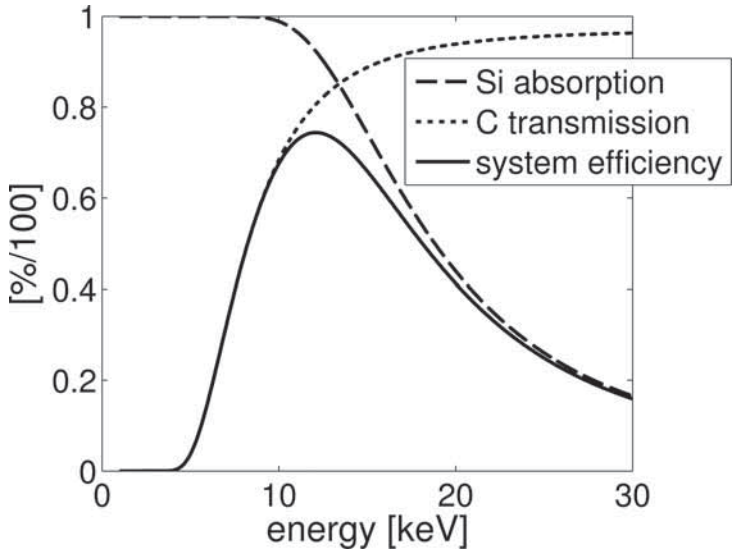

Figure 4.3: Nominal detector, window and system efficiencies as a function of x-ray energy.

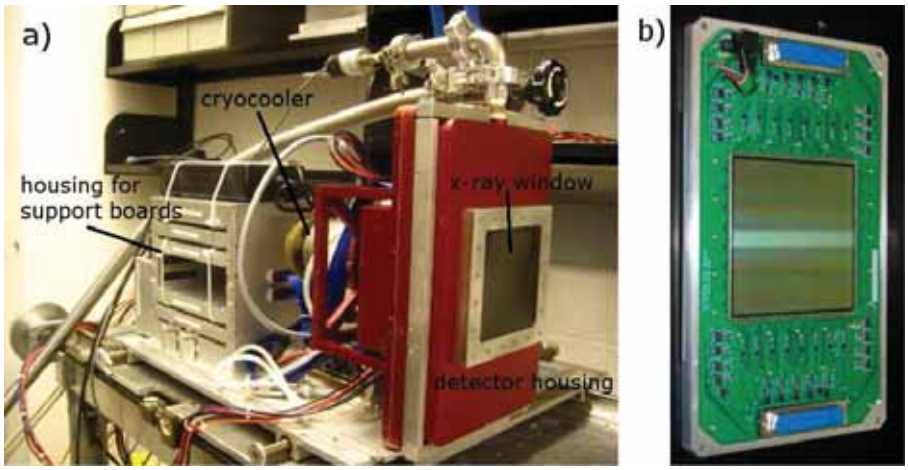

Figure 4.4: (a) The direct-detection CCD with detector housing, cryocooler and support electronics. (b) The bare CCD on its headboard.

software or by a hardware TTL signal. Vertical binning is available on-chip. Figure 4.4 shows a photograph of the prototype device, as well as a photograph of the bare CCD on its headboard.

As described in Chapter 2, in the absence of an electric field, free charge carriers in silicon move diffusively according to Equation 2.5, whereas in the

presence of an electric field, charge carriers drift according to Equation 2.6. By design, in this and other deep-depletion silicon sensors, the full sensor volume should be over-depleted, such that there is a strong transverse electric field across the sensor sweeping photo-generated charges rapidly towards the pixel gates. However, in the prototype CCD described here, the previously mentioned 155 V limit constrained us to operate the device in a partially-depleted state.

It is possible for x-ray photons to be stopped and converted into charge in the undepleted layer. The probability of this occuring depends on the x-ray energy and is greater for lower energies. If an x-ray is stopped in the undepleted field-free region, the photo-generated charge will spread diffusively in three dimensions until it either enters the depleted region or recombines. The recombination time within silicon varies, depending on the defect density, from nanoseconds to milliseconds. Minority carrier lifetimes between 2-6 ms are typical in high-resistivity float zone silicon [38]. Photo-charge generated in the undepleted region that does reach the depletion region before recombination will be collected, but potentially by a pixel some distance away from the location of the photon hit. Therefore, the presence of the undepleted layer has implications for the spatial resolution and efficiency of the CCD, as will be discussed in the next section.

This model provides a qualitative understanding of the effects of partial depletion. It is not our intention to rigorously characterize the motion of charge in the undepleted region, since the presence of an undepleted region in this prototype is a flaw that should not be repeated. As will be discussed in Section 4.4, future revisions of this device would include an improved guard ring structure

that would allow the chip to be operated in over-depleted mode.

The extent to which the undepleted layer impacts device performance depends on its thickness relative to the depleted layer. As described above, ^{55}Fe testing showed evidence of full depletion around 300 V, indicating an 11.4 kΩ-cm resistivity and a 170 μm undepleted layer at the operating reverse bias. Because the electrical damage prevented us from rigorously verifying that 300 V is the absolute minimum bias required for full depletion, we consider this a lower bound on the resistivity, and an upper bound on the undepleted thickness. As will be discussed in Section 4.3.3, efficiency measurements provided a lower bound on the undepleted thickness.

4.3 Detector characterization

The detector characteristics are summarized in Table 4.1[2]. The calibration measurements are described below. Visible light measurements were made using an LED placed within the detector housing. The x-ray calibration measurements were carried out using copper and molybdenum anode x-ray tubes (TruFocus, Watsonville, CA), with 180 μm source size. The distance between the detector window and the x-ray source, or between the mask and the x-ray source where a mask was used, was 1 m, unless otherwise noted. The surface of the CCD is 19 mm behind the detector window.

[2]STA was contracted for a "best-effort" fabrication of an ambitious CCD and the associated electronics. The measured noise and frame rate values in Table 4.1 fall notably short of the values in the STA proposal for fabrication of the detector. Fabrication of the CCD proved to be considerably more difficult than STA had anticipated, and despite repeated fabrication attempts, yields were low and detector characteristics were compromised. The CCD described in Table 4.1 was used for this study, even though it suffered from a bad amplifier and a defective guard rings. It was the best CCD to emerge out of the effort.

Quantity	Value
Pixel size	24 x 24 μm
Format	4000 x 4000 pixels
Frame rate	1.6 Hz in 8-port readout (625 ms read time)
	3.2 Hz in 16-port readout (310 ms read time)
Read noise	3 ADU (0.10 photons)
Pixel well depth	1.4 Me- (373 photons)
Serial register well depth	2.2 Me-
Gain	128.2 e-/ADU (29.2 ADU/photon)
Dark current	22 e-/s at 205 K
Point-spread function FWHM	22 μm (at 17.5 keV)
	40 μm (at 8.0 keV)

Table 4.1: STA3200 characteristics. Quantities quoted in units of photons refer to 13.5 keV photons.

4.3.1 Visible light measurements

Many CCD system parameters can be extracted by examining the visible light photon transfer curve, as described in Chapter 3. A visible-light PTC, shown in Figure 4.5, was obtained by STA using illumination from a red LED. Since each visible photon generates no more than a single electron, the variance in the recorded signal goes as the number of electrons recorded, yielding a direct measurement of system gain. Referring back to Equation 3.13, the variance is linear with respect to the signal, with a slope of $1/K$. These measurements show a system gain of 128.2 e-/ADU, with a read noise of 380 e- RMS. Full well per pixel was measured to be 1.4×10^6 e-. Since x-rays produce an electron hole pair for each 3.6 eV deposited in the silicon, a single 13.5 keV x-ray would generate 3750 e-. Expressing the CCD parameters in terms of 13.5 keV x-rays, the system gain would be 29.2 ADU/x-ray, with a read noise of 0.10 x-ray, and a full well of 373 x-rays. Parameters at other x-ray energies would scale directly as the x-ray energy. Dark current measurements show a non-linearity of <1.5% over the full range, as shown in Figure 4.6. Gain variations between amplifier readouts were

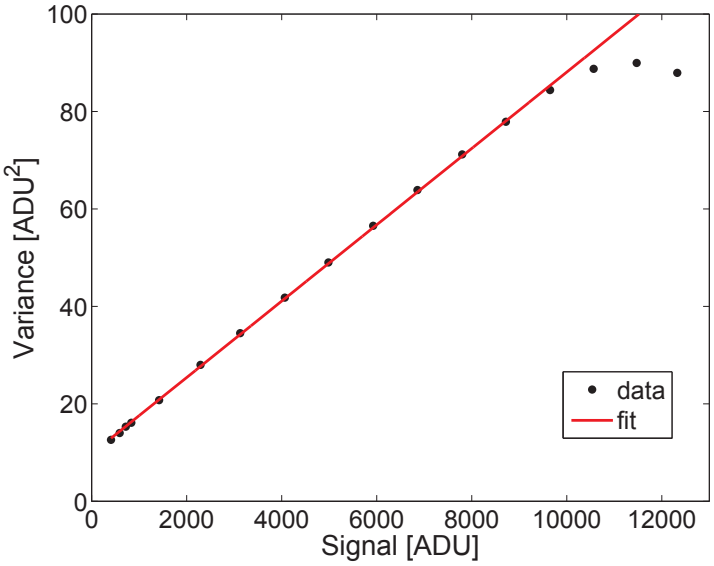

Figure 4.5: Visible PTC for the STA3200 CCD. The variance is fit to a linear function of the signal to yield an estimate of the detector gain.

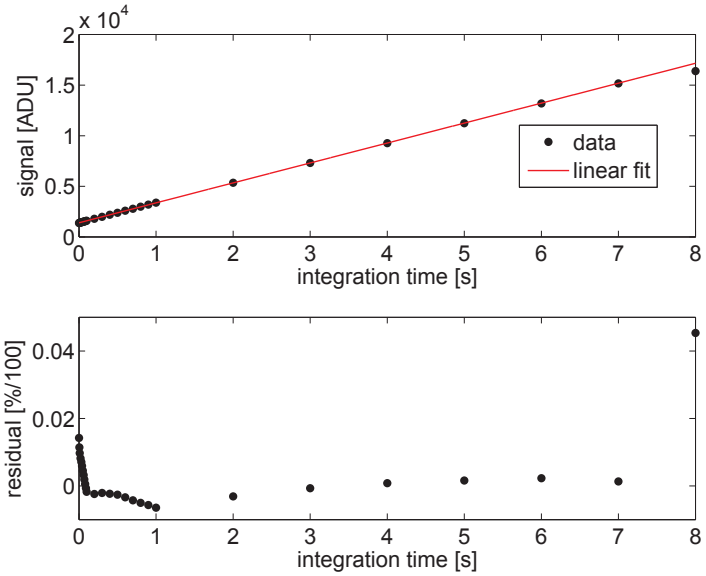

Figure 4.6: Linearity measurements for STA3200 CCD. Dark current was collected with the detector held at 283 K using integration times from 1 ms to 8 s. Dark current was used rather than x-rays in order to collect data up to the pixel full well in a short amount of time. At top, the average signal per pixel within the region is fit to a linear function of the integration time. At bottom, the residuals are plotted as absolute values. The pixels have reached saturation at 8 s, as evidenced by the departure from linearity.

measured to be 1.86% RMS and can be corrected by applying a multiplicative factor.

4.3.2 X-ray gain measurement

The x-ray gain of the STA3200 was also measured using the discrete photon spectrum technique, as described in Section 3.6. An x-ray opaque mask fabricated in 50 μm thick tungsten with a square array of 25 μm diameter pinholes on a 330 μm pitch was used to produce isolated spots of illumination on the detector. The mask was flood-illuminated using a Mo anode tube, biased at 25 kV and 0.078 mA. A 200 μm thick zirconium foil was placed directly in front of the x-ray source to improve the spectral purity, as discussed in Section 3.3.1, and isolate the 17.5 keV Mo Kα line. A set of 50 five second frames were taken, with about 2 photons on average incident through a single pinhole per frame.

Since the illumination from a single pinhole is not necessarily confined to a single pixel, multiple pixels must be summed in order to fully capture the intensity from each spot. Since each pixel in the sum contributes read noise, care is required in defining the area to be summed, as the minimum area which encompasses the signal should be used. To do this, the center of mass of each pinhole was determined from the averaged, background-subtracted image. For a given radius, r, pixels in the neighborhood of a pinhole were flagged if any fraction of their area fell within a circle of radius r centered on the pinhole center of mass, as illustrated in Figure 4.7. In each frame, the flagged pixels were summed to obtain the pinhole intensity. Figure 4.8 shows the spectra obtained for r ranging from 0.33 to 2.00 pixels. As the radius is increased, the photon peaks broaden

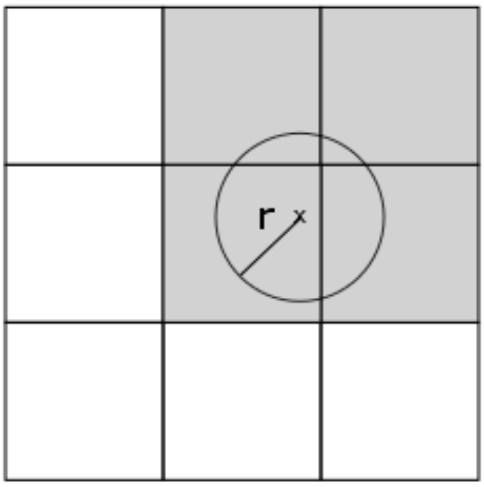

Figure 4.7: A block of 3 × 3 pixels is shown to illustrate the area summation operation. The center of mass of the pinhole is marked by an 'x'. A circle of radius r is drawn centered on the pinhole center of mass. If any fraction of a pixel's area falls within the circle, the pixel is included in the intensity sum.

as additional read noise is incorporated into the sum. The photon peak spacing initially increases as the radius increases to about 1 pixel, then levels off, suggesting that most of the pinhole intensity is captured by the sum with r in the range of 1-1.5 pixels.

To compute the gain, the spectra are fit to a sum of $N + 2$ Gaussians, corresponding to the zero-photon peak, N discrete photon peaks and a diffuse peak that accounts for the tails of the distribution, with the detector gain as a fit parameter. The fit for $r = 1.5$ pixels is plotted in Figure 4.8(c). The computed gain is plotted as a function of summation radius in Figure 4.8(d). The computed gain levels off to 34.5 ADU per 17.5 keV photon for $r = 1.33$ - 1.66 pixels. The measurement at a radius of 2 pixels is more uncertain due to increased read noise introduced into the sum.

Since one electron-hole pair is generated for every 3.6 eV deposited in the

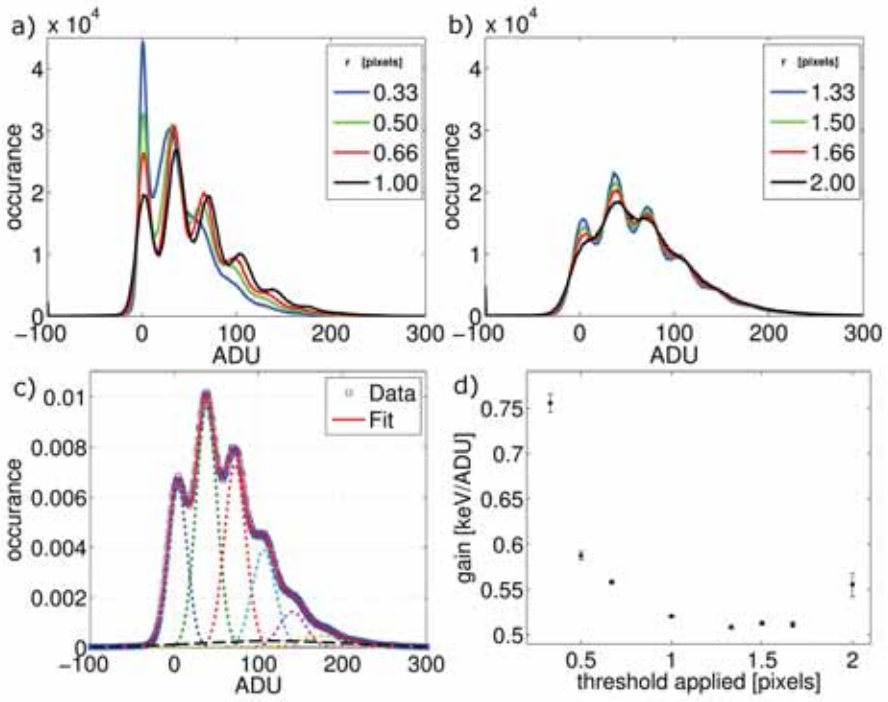

Figure 4.8: (a), (b): The discrete photon spectra obtained by summing pixels within a radius of 0.33-2.00 pixels of the pinhole center of mass. The results are split into two plots for clarity. (c): The fit to a sum of Gaussians is shown for r = 1.50 pixels. The dotted lines show the individual discrete photon peaks and the dashed black line is the background Gaussian. (d): The computed gain from the fit is plotted as a function of the summation radius.

detector, a gain of 34.5 ADU per 17.5 keV photon corresponds to an energy-independent conversion factor of 140 e-/ADU. This agrees well with the measurement made with visible light to within 10%. The agreement between visible light and x-ray measurement confirms that the parameters extracted from the visible light data are valid when extrapolated to the x-ray regime. Note that x-ray spectral peaks at lower x-ray energy broaden due to the higher proportion of photons converting in the undepleted zone. Both the increased lateral spread and loss of charge due to recombination cause these photon peaks to no longer be well resolved.

4.3.3 X-ray Efficiency

The efficiency of the CCD was determined by comparing the signal measured by the CCD with that from a calibrated SDD, as described in Section 3.3. Both the CCD and a Vortex-90EX SDD were illuminated through a 1.9 mm^2 lead aperture with either a Cu or a Mo x-ray tube. Both sources were filtered to improve spectral purity: the Cu tube with a 50 μm thick Ni filter, and the Mo tube with a 75 μm thick Zr filter combined with a 1 mm thick Al filter. The latter configuration provides similar transmission, especially at high energies, to the 200 μm Zr filter described above, with the main difference being decreased transmission of the Kα line.

The number of counts per second in the Kα line of each source was calculated from the SDD data, using an equivalent carbon fiber window to that on the CCD. As described in Section 3.3.1, the SDD sensor thickness was calculated to be 287 $^{+27}_{-29}$ μm. Using the gain computed from the photon transfer curve, the signal recorded by the CCD was converted to a number of photon counts per second. The ratio of the measured to expected flux gives the CCD efficiency: approximately 0.55 $^{+0.07}_{-0.09}$ at 17.5 keV and 0.47 ± 0.01 at 8.0 keV.

If the CCD were fully depleted, the efficiency should be 0.58 at 17.5 keV and nearly 1 at 8.0 keV. The efficiency measured for 17.5 keV x-rays agrees with this expectation within the uncertainty of the measurement. The loss of efficiency at 8.0 keV indicates that the CCD is not fully depleted. Since the CCD depletes from the p-n junction at the front side, under-depletion would result in an undepleted layer at the back side (i.e., the x-ray entrance side). X-rays could still be stopped and converted into charge in the undepleted layer, but the photogenerated electrons would be more likely to be lost to recombination. There

would also be a loss of spatial resolution, due to the absence of a strong electric field to sweep the photo-generated charge towards the CCD gates, as discussed in Section 2.1.3. The undepleted layer could therefore be partially collecting. If the undepleted layer were approximated as a purely attenuating dead layer, the efficiency measurements would suggest a thickness of 55 μm at the operating reverse bias of 155 V. This gives a lower bound on the thickness of the undepleted layer.

The effect of the reverse bias on the collection efficiency was probed by repeating the measurement for Cu Kα radiation over a range of reverse bias settings. The measured efficiency is plotted in Figure 4.9. The curve shows a growing depletion thickness with increasing bias. However, the loss of efficiency at 170 V suggests that the CCD is still far from fully depleted. At 170 V and above a sharp increase in current draw on the reverse bias supply, combined with an increase in dark current around the chip edges, indicated the onset of electrical breakdown in the chip. The cause appears to be damage to the electrical guard ring structure on the surface of the CCD. While this constrained the reverse bias that could be applied, it allowed sufficient depletion of the CCD for the characterization of this report.

4.3.4 Spatial resolution

In a direct-conversion device, the point spread is determined by the lateral diffusion of charge carriers as they traverse the diode, as discussed in Section 2.1.3. In the ideal case of an overdepleted sensor, the lateral charge carrier diffusion is limited by reducing the time required to sweep the charge carriers across the

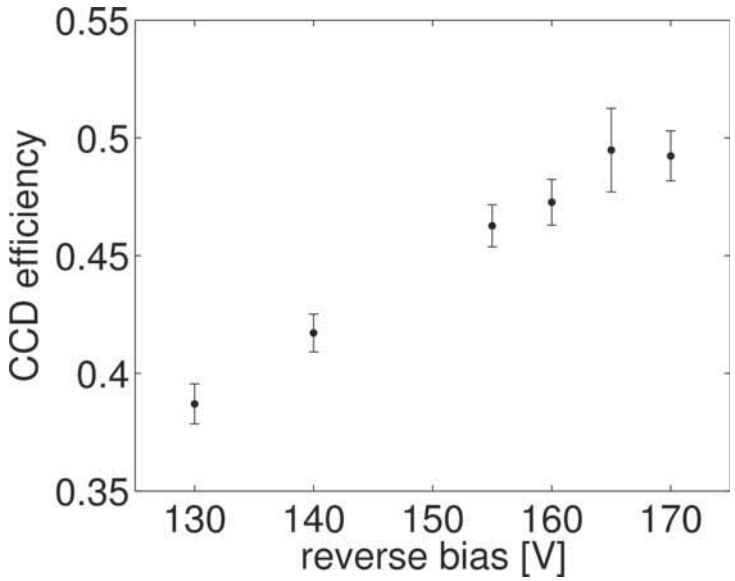

Figure 4.9: The measured CCD efficiency at 8.0 keV as a function of reverse bias.

diode.

As a test case, we consider the lateral charge spread in a 10 kΩ-cm, 600 μm thick fully-depleted sensor cooled to 205 K. The full calculation is shown in Appendix A, and is summarized here for reference. We model the scenario where the x-ray is absorbed at the back surface of the sensor, which gives the longest transit time and therefore an upper bound on the lateral spread of the charge cloud. This calculation does not take into account inter-charge repulsion or local field variations, which in an over-depleted sensor will be weak compared to the reverse-bias field. The results obtained give an estimate of the point spread that can reasonably be achieved with a 600 μm thick, fully-depleted silicon sensor. The standard deviation of the Gaussian charge cloud is plotted as a function of overbias voltage in Figure 4.10. A σ of 10 μm is expected at 10 V overbias, an applied bias of approximately 350 V. The support electronics for the CCD were chosen to accommodate an applied bias of 500 V. However, in the current prototype, the power supply draw became unstable above a reverse bias of 155

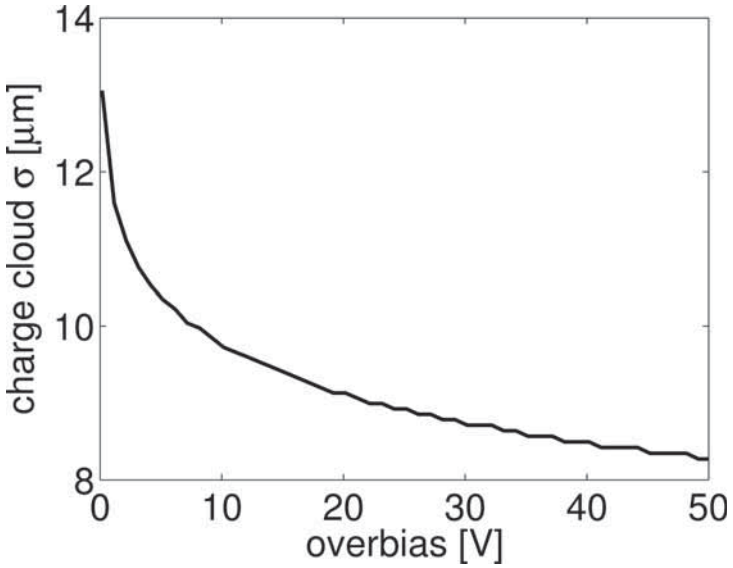

Figure 4.10: The charge cloud width σ versus overbias in a 600 μm 10 kΩ-cm diode.

V.

To characterize the spatial resolution of the CCD, the response to knife edge illumination was measured, as described in Section 3.4. A 1 mm thick tungsten knife edge was placed within 4 mm of the CCD window and was aligned with the charge transfer axis of the CCD, then tilted by approximately 2° using a rotation stage. The knife edge was illuminated by a Mo tube biased at 25 kV and 0.142 mA, filtered by a 200 μm thick Zr foil. A set of 50 sixty second exposures was averaged to obtain the final knife-edge image. A complementary dataset was taken with the knife edge oriented slightly off-axis in the direction perpendicular to charge transfer. The measurement was repeated using a Cu tube, biased at 15 kV and 0.6 mA, with a 50 μm thick Ni filter. By plotting the intensity along a row or column that the knife edge crosses, the edge-spread response (ESR) of the device is obtained (Figure 4.11).

For 17.5 keV (Mo Kα) radiation, the ESR is similar in both directions. The

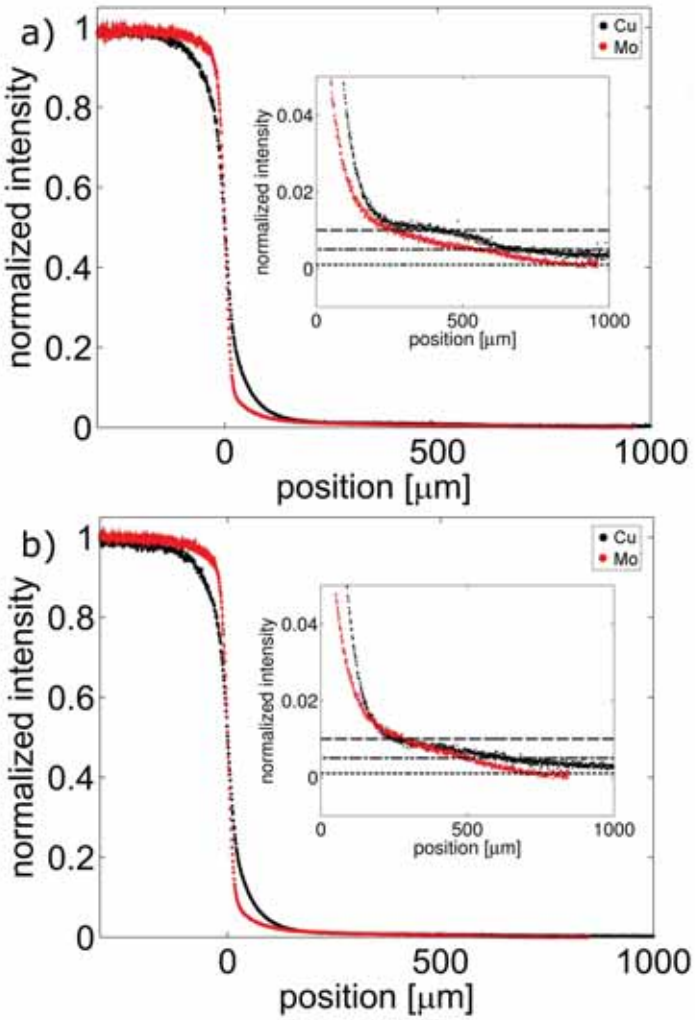

Figure 4.11: (a) The edge-spread response of the CCD parallel to the charge transfer direction. (b) The edge-spread response perpendicular to the charge transfer direction. The 1, 0.5, and 0.1% levels are indicated by dashed lines in the insets.

most notable feature of the measured ESR is the long tail in the non-illuminated region. The intensity falls off to the 10% level at 20 μm from the knife edge, to the 1% level at 300 μm, to the 0.5% level at 500 μm, and to the 0.1% level at 800 μm.

For 8.0 keV (Cu Kα) radiation, the long-range spread is greater. The intensity falls off to the 10% level at 55 μm from the knife edge in both directions, to the 1% level at 300 μm from the edge in the perpendicular direction and 400 μm in the parallel direction, and to the 0.5% level at 650 μm in both directions. Elevated dark current near the chip edges corrupts the response curve before the 0.1% level is reached.

The long tails of the edge-spread response, and the dependence on energy, again indicate that the detecting volume is not fully depleted. As discussed previously, when photons are stopped in the undepleted layer, there is no electric field to sweep the charge carriers efficiently towards the CCD gates. Instead, the charge produced diffuses in three dimensions but in this case the lateral spread can be significant by the time the charge reaches the depletion region. Charge carriers that reach the depletion region before recombining will be swept to the CCD gates by the reverse bias field, but will be collected by pixels potentially far away from the original photon hit. A greater portion of the incident radiation will be stopped in the dead layer at 8.0 keV than at 17.5 keV. Given the observed lateral charge spread of several hundred microns, recombination lifetime must exceed a few microseconds. This is well within the electron lifetime possible in high-purity float-zone silicon [38].

The line spread response (LSR) is obtained by differentiating the ESR and is shown in Figure 4.12. The LSR was modeled as a convolution of a Gaussian,

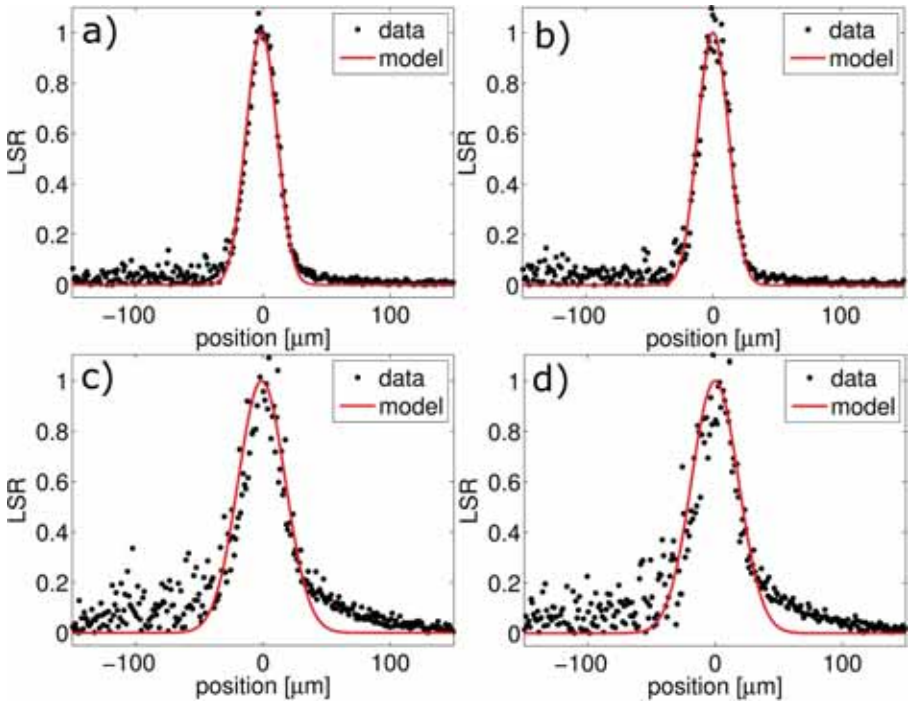

Figure 4.12: (a) The LSR perpendicular to charge transfer with Mo radiation. (b) The LSR parallel to charge transfer with Mo radiation. (c) The LSR perpendicular to charge transfer with Cu radiation. (d) The LSR parallel to charge transfer with Cu radiation. Each measured curve is shown along with the best fit model.

representing the diffusion of charge in the sensor, with a boxcar function representing the 24 μm pixelation. This model gave a best-fit charge diffusion FWHM of 22 μm for Mo Kα radiation and 40 μm for Cu Kα radiation. Though the data deviates from this model at the low-intensity tails, the fit is reasonable at the FWHM level.

4.3.5 Uniformity of response

In addition to fixed pattern noise and cosmetic defects, flood field illumination of the CCD shows characteristic "tree ring" variations (Figure 4.13). As described in Section 3.7, this pattern is due to the lateral deflection of charge

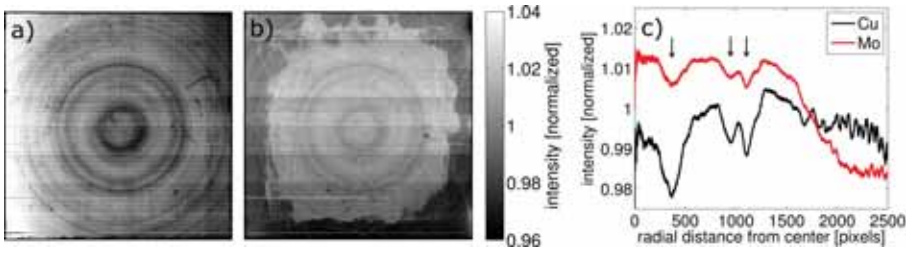

Figure 4.13: (a) A Cu Kα flood field. (b) An Mo Kα flood field. (c) An azimuthal integration of both flood fields, centered on the tree rings structure. An annulus width of 1 pixel was used.

carriers by local electric fields caused by radial resistivity variations in the silicon. The silicon used in this device has a stated radial resistivity tolerance of 25%. Because the CCD is under-depleted, the doping inhomogeneities may also lead to local efficiency variations which contribute to the tree ring pattern. The tree rings are most likely due to a superposition of lateral deflection and efficiency variation. Note that since the CCD is cut to the maximum size allowed by a 6-inch wafer, the full tree ring structure of the wafer is visible, whereas in smaller devices, a single sensor includes only a slice of the pattern from the source wafer.

The magnitude of distortions depends on several factors, including the angle of incidence, the conversion depth and the x-ray energy. The dependence on x-ray energy is illustrated in Figure 4.13, which shows a Cu Kα flood field and a Mo Kα flood field, respectively. The flood fields were taken using a Cu tube biased at 18 kV and 0.4 mA, at a distance of 1.5 m from the detector window, and a Mo tube, biased at 25 kV and 0.6 mA, with a 200 μm thick Zr filter, at a distance of 1 m from the detector window. The tree ring structure is more distinct in the Cu Kα flood field, but is present in both images. An irregularly-shaped region of increased intensity covering most of the chip is visible in the Mo Kα flood field (Figure 4.13b). Due to its shape, we suspect it is visible fluorescence from the

thermal grease (Apiezon N; M&I Materials Limited, Manchester, UK) between the CCD chip and the aluminum cold plate. Apiezon N has been shown to fluoresce in the blue under UV light [70]. Clearly, a non-fluorescent thermal coupling compound should be used for future work.

An azimuthal integration of each flood field is plotted in Figure 4.13(c) as a function of radial distance rchip from the center of the chip. At around r_{chip} = 1500 pixels, in the Mo Kα flood field, the thermal grease fluorescence falls off, leading to a large downward shift in the intensity curve that is independent from the tree rings. Since the fluorescence fall-off is a separate effect from the tree rings, in order to compare the tree ring effects in the sensor in the Mo and Cu Kα flood fields, we focus on the inner region of the chip (r_{chip} = 0 to 1500 pixels). Within this region, there are three significant dips in the intensity curve, indicated by arrows in Figure 4.13(c). These features correspond to dark rings in the flood images. The maximum peak-to-peak excursion in this region is 1.5% in the Mo Kα flood field and 2.7% in the Cu Kα flood field. The RMS variation in the inner region is 0.2% for the Mo Kα flood field and 0.7% for the Cu Kα flood field.

4.3.6 Radiation damage

Radiation damage measurements were carried out on an STA 1759A imager similar in design to the current prototype. The STA 1759A chips were 250 μm thick and were illuminated from the front (gate) side. The benefit of doing radiation damage testing on a front-illuminated device is that it is much easier to observe the effect of radiation on the oxide, whereas in a thick back-illuminated

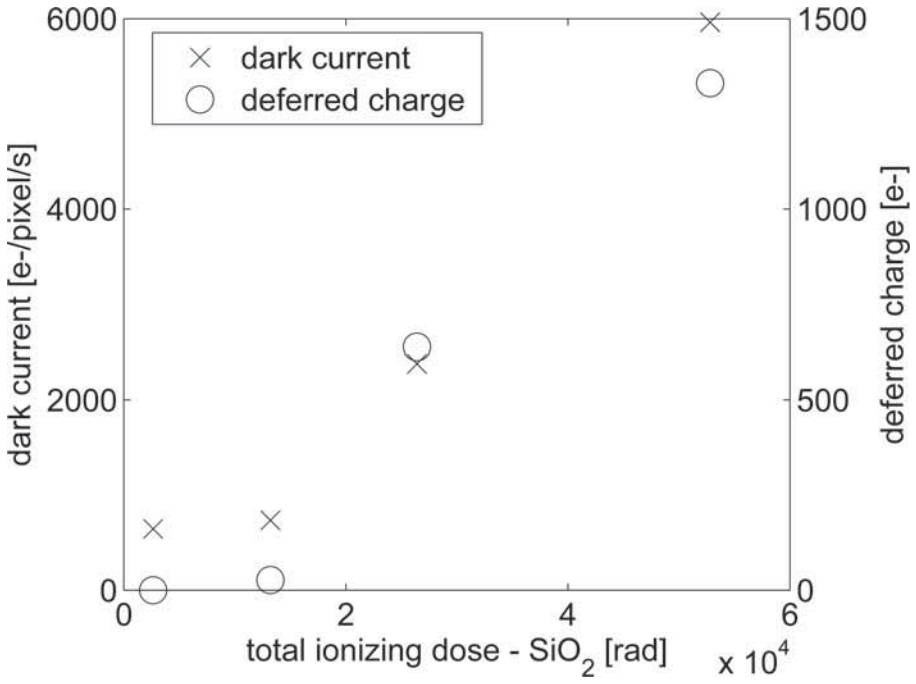

Figure 4.14: STA1795A radiation damage measurements.

device, the gate oxide is shielded by the thick Si detecting layer. As described in Section 2.1.4, the creation of electron-hole pairs in the oxide is a primary source of radiation damage in CCDs.

The test devices were cooled with liquid nitrogen to 213 K and were biased and clocked as in normal operation during radiation damage testing. 8.0 keV Cu Kα x-rays were generated by a rotating anode and isolated by a multilayer monochromater. The dose rate was measured to be 78 rad/s in Si and 44 rad/s in SiO2. Dark current and deferred charge, a measure of charge transfer efficiency (CTE) degradation, were monitored as the devices were dosed. The results are shown in Figure 4.14. A slight (6%) increase in dark current was detected at the lowest dose level recorded, 2640 rad (SiO2). CTE degradation was detected at 13200 rad (SiO2)[3].

[3]The standard SI unit for absorbed dose is the gray (Gy). 1 rad = 0.01 Gy.

4.4 Outlook

The current prototype device exhibits a point spread on the order of 22-40 μm FWHM and a pixel read noise equivalent to 1/10 of a photon at 13.5 keV. Even given known flaws, the prototype performs successfully in the context of protein crystallography, as will be shown in the next chapter. However, further development would improve the frame rate and support electronics, and would eliminate the undepleted layer on the x-ray entrance side of the diode. Thus, the results of the prototype studies have laid the foundation for modifications to future, improved device performance. Lessons for further development are described below.

4.4.1 Undepleted layer and biasing

The undepleted layer is the greatest drawback to the current prototype, leading to loss of efficiency and spatial resolution. The onset of electrical breakdown at the relatively low reverse bias of 170 V needs to be resolved so that the chip can be fully depleted. The early onset of breakdown suggests that the guard ring structure has been damaged. The guard rings in the current prototype are 15 μm wide with 6 μm gaps between rings. An inter-ring gap on the order of 20-30 μm would be more robust.

4.4.2 Frame rate

The current maximum frame rate is ~3 Hz. Higher frame rates could be achieved by increasing either the serial register clock frequency or the number of readout amplifiers. At the current clock frequency and chip size, increasing the number of amplifiers per side from 8 to 32 would result in a maximum frame rate of 20 Hz, the original design goal. A potential drawback to increasing the number of amplifiers on a large device is a decrease in yield due to amplifier failure. This risk could be mitigated through the use of in-process gettering, as described in [43] and currently used in the fabrication of deep-depletion CCDs at LBNL. STA has also proposed modifications to the readout amplifier gates to minimize voltage breakdown. STA has recently fabricated a 36 mm $\times$ 36 mm CCD chip with 56 output amplifiers, i.e. 28 amplifiers per side. The deep-depletion CCDs fabricated at LBNL have even higher amplifier densities, with 192 amplifiers on a 28 mm $\times$ 28 mm chip in a recent CCD [29].

Alternatively, to reduce the noise penalty associated with an increase in clock speed, there are two possible approaches. First, the support electronics could be re-designed so that the CCD output is digitized on the headboard in close physical proximity to the chip outputs; currently digitization takes place on A/D boards connected to the CCD headboard by long (0.3 m) readout cables. This could reduce clock feed-through noise and allow the serial register clock frequency to be increased, without redesigning the chip itself. Second, if the chip were to be redesigned, a four-phase serial register with complementary clocking would lead to reduced clock feed-through in the serial register.

4.4.3 On-chip binning

The current support electronics allow on-chip binning in only one direction and should be redesigned to allow on-chip 2×2 binning. The benefit would be a reduction of read noise in binned mode. Given read noise σ, the noise associated with summing a 2×2 area in software is 2σ. Binning 2×1 allows the same area to be summed with a total noise of $\sqrt{2}\sigma$. Binning 2×2 on-chip would reduce the noise to, simply, σ. Since this detector is optimized for low-flux experiments, it is not critically important that the serial register is not large enough to accommodate 4 times the single-pixel full-well. 2×2 on-chip binning would still be desirable for extremely low-flux scenarios, due to the read noise benefit.

If the chip were to be re-designed, the CCD summing well gate could be enlarged to hold four times a single-pixel full well, making 2×2 on-chip binning possible with no sacrifice in well depth per unit imaging area. However, enlarging the summing well gate could reduce the charge transfer efficiency, so this change would have to be prototyped and studied carefully.

4.4.4 Yield improvement

The yield on this device was poor, with 2 functional devices obtained out of 5 12-wafer fabrication runs. A number of changes could improve the yield in future iterations. The metal strapping resulted in a large number of vertical shorts, which rendered the affected devices inoperable. Reducing the strapping to every 3rd column would reduce the susceptibility to metal particulates that result in shorts. The 4-phase gate structure is also susceptible to inter-poly shorts, though this was not the dominating factor in the yield problems. A device with

3-phase parallel and serial registers would be less susceptible to failure due to inter-poly shorts. However, a 3-phase imaging pixel has a smaller well depth than a 4-phase pixel of the same size.

4.4.5 Amplifier sensitivity

The output amplifier sensitivity could be increased from the current 1 μV/e- to the order of 6 μV/e-. This would significantly reduce the x-ray equivalent read noise of the detector. Compared to the deep-depletion CCDs fabricated at LBNL and by the ASG, described in Section 1.3.2, the current STA3200 prototype does have considerable read noise (380 e-, compared to $\sim$ 20 e- in the LBNL and ASG detectors). However, the well depth of the STA3200 is considerably higher than the other two devices (about 2.8 times larger than the ASG CCD). Increasing the STA3200 amplifier sensitivity would involve trade-offs in terms of speed and well depth that would have to be studied carefully. If a increased amplifier sensitivity were pursued, the amplifier gain could be made programmable so that users could choose between a low-noise/small-well mode and a higher-noise/larger-well mode.

4.4.6 Radiation hardness

Finally, the radiation hardness of the device could potentially be improved through a few methods. As described in Section 2.1.4, detectors with thinner oxides are more robust against radiation damage. In the current prototype, fabricated in DALSA's standard CCD process, the oxide is 50 nm thick. A thinner

oxide could be investigated to provide increased radiaiton hardness. However, the gate oxide cannot typically be made as thin as in a CMOS process (where the oxide may easily be < 10 nm), because higher voltages are applied to CCD pixel gates (on the order of 10 V) than to CMOS transistor gates (typically 1-3.3 V). The detector could also be periodically annealed to at least partially reverse the radiation damage due to trapped charge within the oxide.

CHAPTER 5

PROTEIN CRYSTALLOGRAPHY WITH THE STA3200

5.1 Introduction

Protein microcrystallography is the target application for the STA3200 direct-detection CCD. Recalling Equation 1.2, the average diffraction peak intensity from a crystal of volume V_{xtal} and unit cell volume V_{cell} scales as V_{xtal}/V_{cell}^2. The STA3200 was designed specifically to enable the collection of data from these weakly-diffracting samples, and to complement the other experimental methods discussed in Chapter 1. The tight point spread and small pixels ensure that the spatial characteristics of the diffraction pattern are preserved faithfully and that weak Bragg spots are not washed out by a large point spread. Additionally, the large number of charge carriers generated per x-ray photon makes the pixel read noise (3 ADU, equivalent to 380 electrons) equivalent to about 1/10 of a 13.5 keV photon. This combination of high spatial resolution and low x-ray equivalent read noise increases the detector SNR and makes the device uniquely suited to protein microcrystallography. This chapter describes an experiment carried out at CHESS in which the successful collection of crystallographic data using the STA3200 is demonstrated, and the performance of the STA3200 is compared to that of a convetional phosphor-coupled CCD.[1]

[1] Parts of this work have been published in Journal of Applied Crystallography [69].

5.2 Measurements at CHESS

A series of protein crystallographic data sets were taken at the F1 beamline at CHESS to examine the detector performance. Data were also collected on a Quantum 270 (Q270) phosphor-coupled CCD (Area Detector Systems Corporation, Poway, CA), for direct comparison. The Q270 has 64.8 μm x 64.8 μm pixels at the phosphor surface. As reported by the manufacturer, the spatial resolution FWHM is 90 μm, and the read noise is equivalent to about 1/2 of a 12 keV photon. As can be seen in Table 1.3, this is the lowest read noise found among phosphor-coupled CCDs commonly used in protein microcrystallography. The readout time in the unbinned mode used here is 1.1 seconds.

5.2.1 Experimental setup

The F1 beamline uses a bent Si(111) monochromator crystal and a rhodium-coated Si mirror to focus the x-ray beam from a 24-pole wiggler in the horizontal and vertical directions, respectively. The x-ray beam entering the experimental hutch has an energy of 13.5 keV, with dimensions 0.15 mm by 0.70 mm (FWHM, vertical and horizontal, respectively) and divergence 0.1 mrad by 2.2 mrad (vertical and horizontal, respectively). The beam can then be collimated to 100 μm or focused to 20 μm or smaller using a focusing capillary. The flux is 5.5×10^9 photons/s through a 100 μm collimator at a typical positron beam current of 200 mA.

The samples were flash-frozen thaumatin crystals in 20% glycerol [71]. Thaumatin is a protein found in certain fruits and sometimes used as an artificial

sweetener. Because it is relatively easy to crystallize, it is often used as a test system in studies focused on the development and evaluation of new experimental techniques. All crystals had dimensions in the range 60-100 μm. The crystals were mounted in nylon loops and held in a cold stream at 100 K.

In order to collect comparable datasets on both detectors, the STA3200 was mounted on a vertical translation stage just below the Q270, allowing a rapid switch between the two. Exposures were 1 second with a 1° oscillation per frame, with 90 frames collected per dataset. The exposure time was chosen to limit the number of overexposed reflections. To ensure that radiation damage during data collection did not dominate data quality, four datasets were taken per sample for comparison, alternating detectors after each dataset. The first and third/second and fourth datasets were compared to assess the extent of radiation damage. No significant effect was found for most of the crystals used, including the four used below for analysis and image comparison; this assessment was based on the whether the quality of the diffraction spots changed noticeably between datasets, and whether spots far from the beamstop (i.e., those containing high-resolution information about the crystal structure) faded as data was collected.

Four different experimental configurations were tested: 100 μm beam with the detectors at equal distance from the sample, 100 μm beam with equal solid angle per pixel per detector, 20 μm beam with equal distance, and 20 μm beam with equal solid angle per pixel. The 100 μm beam was produced with a simple collimator, with the collimator end 23 mm from the sample. The 20 μm beam was produced using a single-bounce focusing capillary [72]. A beamstop 1 mm in diameter was placed 23-25 mm downstream of the sample to block the direct

beam.

Because of the relatively small size of the STA3200, it was necessary to place that detector as close as physically possible to the sample in order to span an acceptable solid angle. In general, for protein crystallography a diffraction pattern with well-resolved spots corresponding to 2.0-2.5 Å resolution is considered to be "good", whereas a very high quality diffraction pattern would have spots resolved out to 1.0-1.5 Å [3]. For the equal-solid-angle experiments, the direct-detection CCD was placed 113 mm from the sample; the Q270 was placed 292 mm from the sample. From Bragg's law (Equation 1.1), this leads to a maximum possible resolution of 2.3 Å and 2.1 Å, respectively. For the equal-distance experiments, a sample-to-detector distance of 150 mm was chosen to accommodate physical constraints that prevented us from moving the Q270 closer to the sample. In this configuration, the maximum possible resolution is 2.9 Å on the STA3200 and 1.3 Å on the Q270.

5.2.2 Crystallographic analysis

Crystallographic analysis was performed[2] using MOSFLM [73] and SCALA [74]. The results for the four different configurations are shown in Table 5.1. Data quality was assessed by evaluating R_{merge}, a measure of the agreement of Bragg reflections across multiple measurements, defined as

$$R_{merge} = \frac{\sum_{hkl} \sum_i |I_{hkl,i} - < I_{hkl} >|}{\sum_{hkl} \sum_i I_{hkl,i}} \tag{5.1}$$

in which $I_{hkl,i}$ is the i^{th} measurement of reflection hkl and $< I_{hkl} >$ is the average intensity of the reflection [74]. In all but one case, the STA3200 data resulted in

[2]Crystallographic analysis was carried out by Dr. Marian Szebenyi from MacCHESS, to whom I am deeply indebted.

lower R_{merge} than the Q270, indicating increased fidelity of measurement. In the case of Thau13, the only data set for which the Q270 had better statistics than the STA3200, the diffraction spots on both detectors showed evidence of splitting. We speculate that this may be a scenario where it is preferable, for the purposes of protein structure determination, to resolve less detail within the Bragg spots, and that this may account for the hampered performance of the direct-detection CCD.

Crystal	Mosaicity	Beam size	Detector	Distance	R_{merge}	R_{merge}(fulls)
Thau9	9.8 mrad	100 μm	Q270	148 mm	0.093	0.070
			STA3200	153 mm	0.056	0.038
Thau6	6.3 mrad	20 μm	Q270	148 mm	0.104	0.090
			STA3200	153 mm	0.100	0.067
Thau13	1.4 mrad	100 μm	Q270	292 mm	0.092	0.065
			STA3200	113 mm	0.115	0.088
Thau4	5.2 mrad	20 μm	Q270	292 mm	0.106	0.092
			STA3200	113 mm	0.095	0.069

Table 5.1: Summary of protein diffraction results from the two detectors. Thau6 and Thau9 are nominally equal distance datasets.

On full and partial reflections

In order to explain the presence of R_{merge}(fulls) in Table 5.1, the concept of fully- and partially-recorded diffraction spots needs to be explained. As the crystal is rotated, crystal planes pass into and then out of the diffraction condition. Because this does not happen instantaneously, but over a finite angle, diffraction planes can either pass into and out of the diffraction condition within a single frame (producing "full" reflections), or pass into the diffraction condition in one frame and out in a subsequent frame (producing "partial" reflections).

Due to timing jitter in the triggering interface between the beamline and the

STA3200, some partially-recorded reflections had slight tails due to the shutter being open during readout, whereas this was not an issue with the Q270. As such, the difference in merging statistics between the two detectors is greater if only full reflections are included in the calculation.

5.2.3 Image comparison

In addition to the merging statistics reported above, detector performance can be assessed by examining the relative image quality on the two CCDs. In general, due to the tighter point spread function and smaller pixels, finer detail was seen on the STA3200 data than in the Q270 data. In this section, nominally identical frames from each of the samples listed in Table 5.1 are shown from both detectors for comparison.

There are inherent difficulties in this type of qualitative comparison. When the sample-to-detector distances were set to give equal solid angle per pixel on each detector, the Q270 was farther back and therefore received slightly less intensity per pixel, and in particular, a different ratio of background scatter to diffraction spot intensity. The background scatter per pixel decreases roughly as $1/R^2$, where R is the sample-to-detector distance. The intensity per pixel for the Bragg spots was also decreased, due to the divergence of the diffraction spots (with contributions, again, from both the divergence of the beam incident on the sample and the crystal mosaicity), but the fall-off is generally slower than $1/R^2$.

When the sample-to-detector distances were equal, the Q270 pixels spanned a larger solid angle and therefore collected more intensity than individual pixels on the STA3200. Additionally, the beam intensity was continually changing

through data collection due to changing conditions in the accelerator, i.e. particle beam decay and injection. The question naturally arises how to display images from the two detectors to yield a valid comparison. Here, I have chosen to set the contrast in each corresponding pair of images such that the maximum of the grayscale for each detector is set to a fixed percentage of the maximum intensity recorded on that detector in a defined region of interest.

Figures 5.1, 5.2, 5.3, and 5.4 show frames from Thau4, Thau6, Thau9 and Thau13, respectively, along with magnified regions spanning several diffraction spots. In each image, an equal solid angle is shown from each detector. In all cases, dark current was subtracted (using one frame frame for the Q270, as is the standard protocol for that detector, and an average of 20 frames for the STA3200). The images were then scaled by the detector gain, so that the grayscale is in units of number of photons.

The data in Figures 5.1 and 5.2 were collected using the 20 μm beam. Especially when zooming in on small regions of the frames, the effect of the different PSFs can be seen: diffraction spots on the STA3200 tend to have sharp edges, whereas spots on the Q270 have dim halos. This is particularly evident in the high-intensity spots near the beamstop in Figure 5.2.

The data in Figures 5.3 and 5.4 were collected using the 100 μm beam. The effect of the point spread is not as evident here, indicating that the benefit of direct detection is greater for small beam sizes.

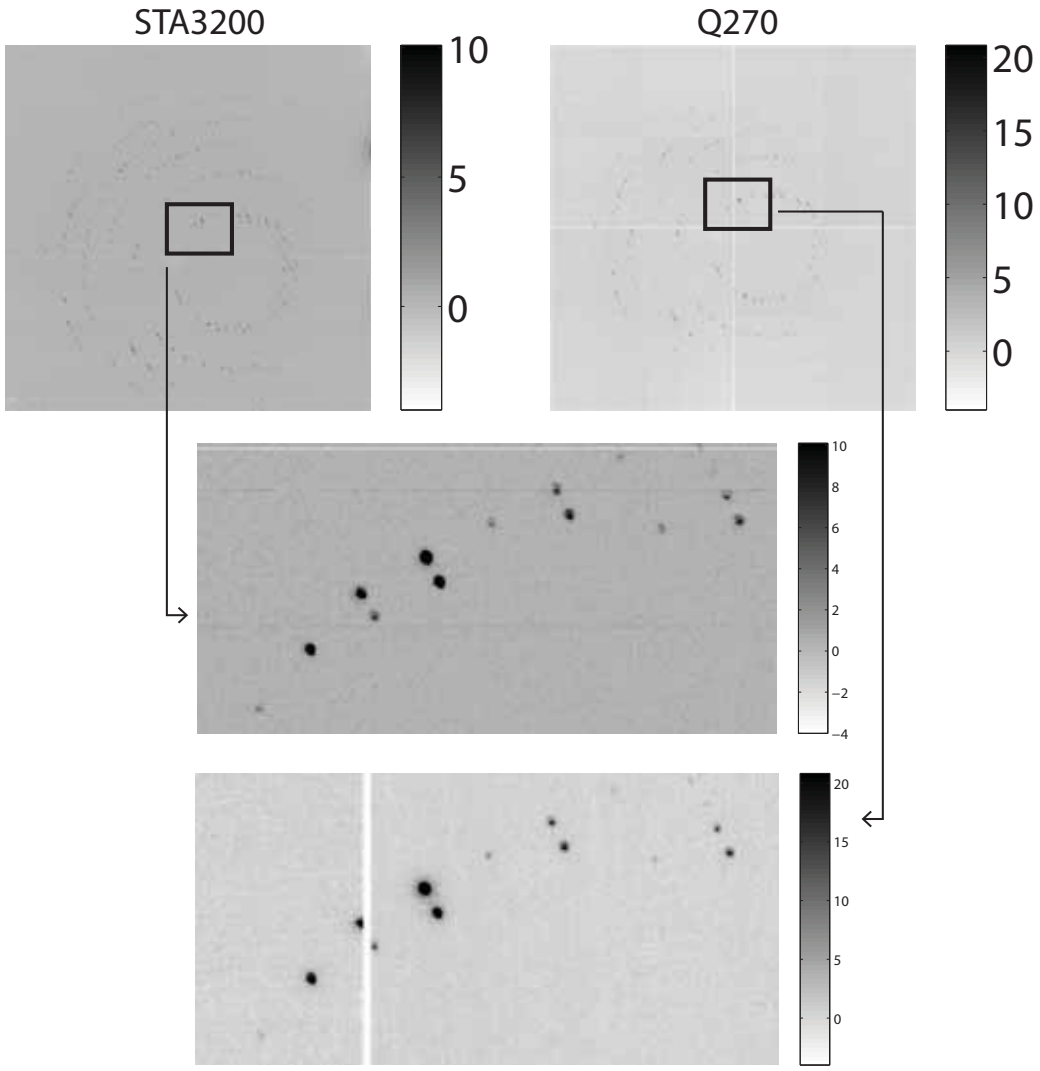

Figure 5.1: Comparison of diffraction pattern from sample Thau4. For this sample, the beam size was 20 μm and the sample-to-detector distances were set to give equal solid angle per pixel per detector. The boxed regions in the large images at top are magnified at bottom. The grayscale is cast in units of number of photons, with the maximum of the scale set to 2% of the maximum intensity in the frame.

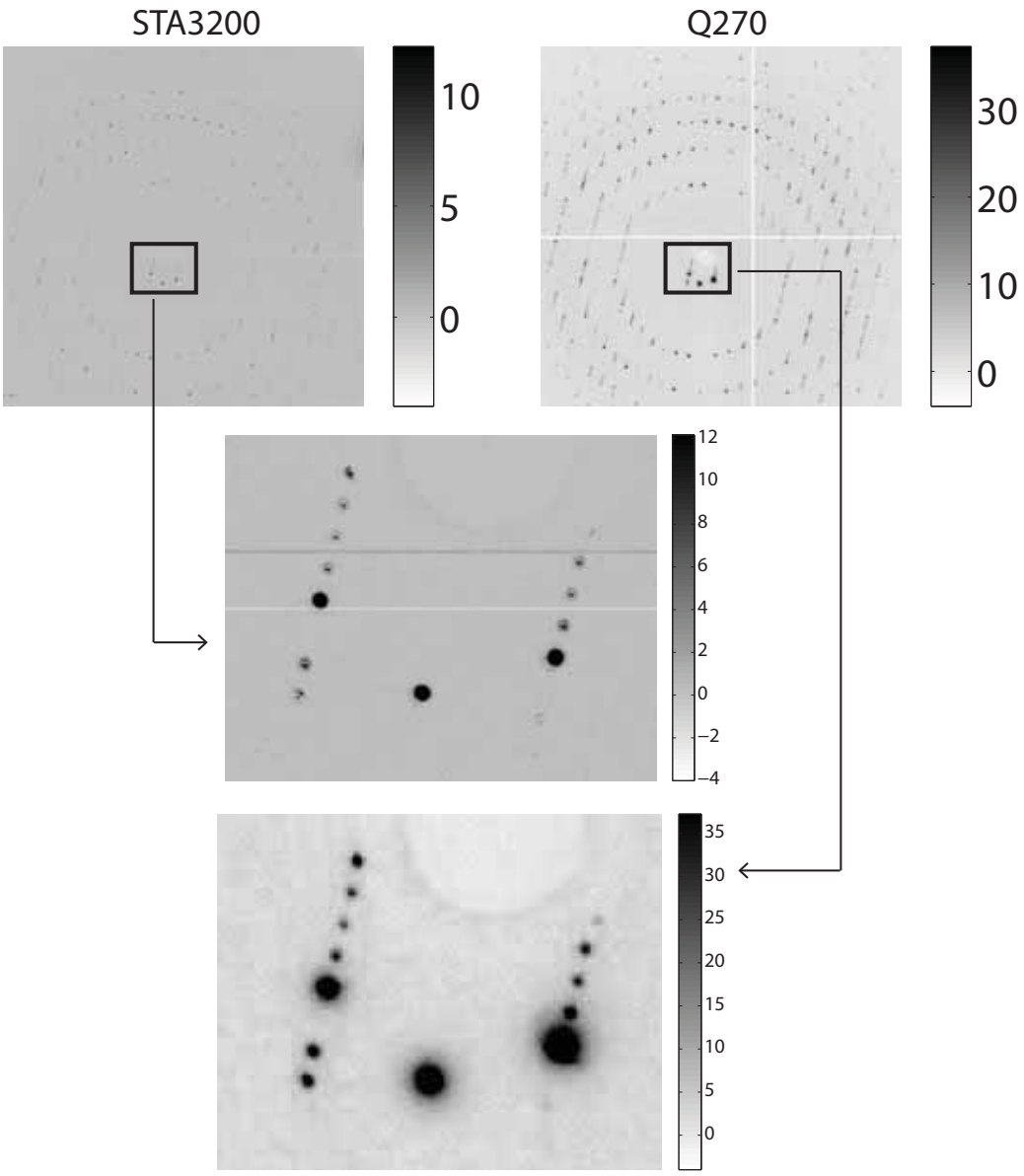

Figure 5.2: Comparison of diffraction pattern from sample Thau6. For this sample, the beam size was 20 μm and the sample-to-detector distances were equal. The boxed regions in the large images at top are magnified at bottom. The grayscale is cast in units of number of photons, with the maximum of the scale set to 2% of the maximum intensity in the frame.

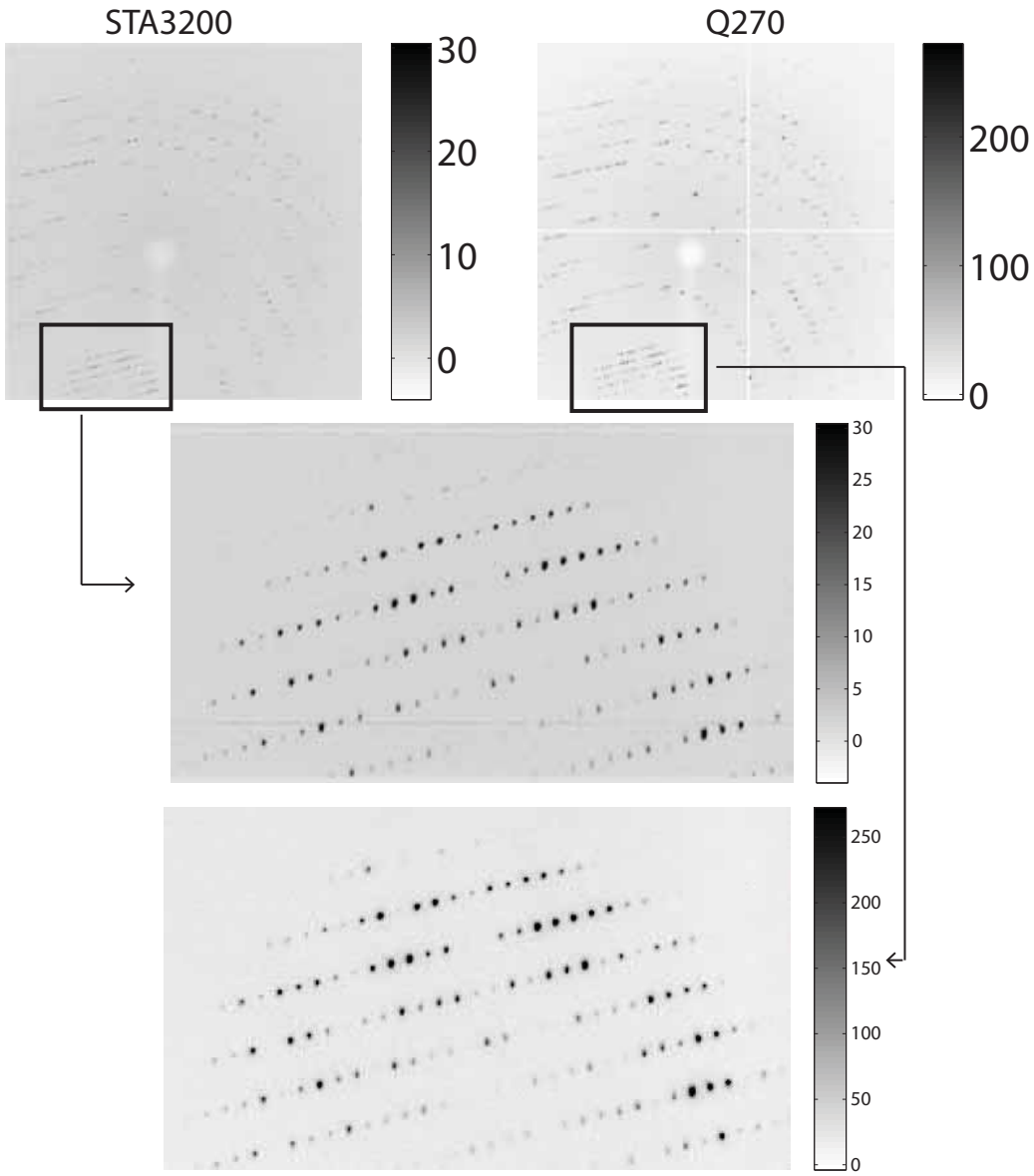

Figure 5.3: Comparison of diffraction pattern from sample Thau9. For this sample, the beam size was 100 μm and the sample-to-detector distances were equal. The boxed regions in the large images at top are magnified at bottom. The grayscale is cast in units of number of photons, with the maximum of the scale set to 5% of the maximum intensity in the frame.

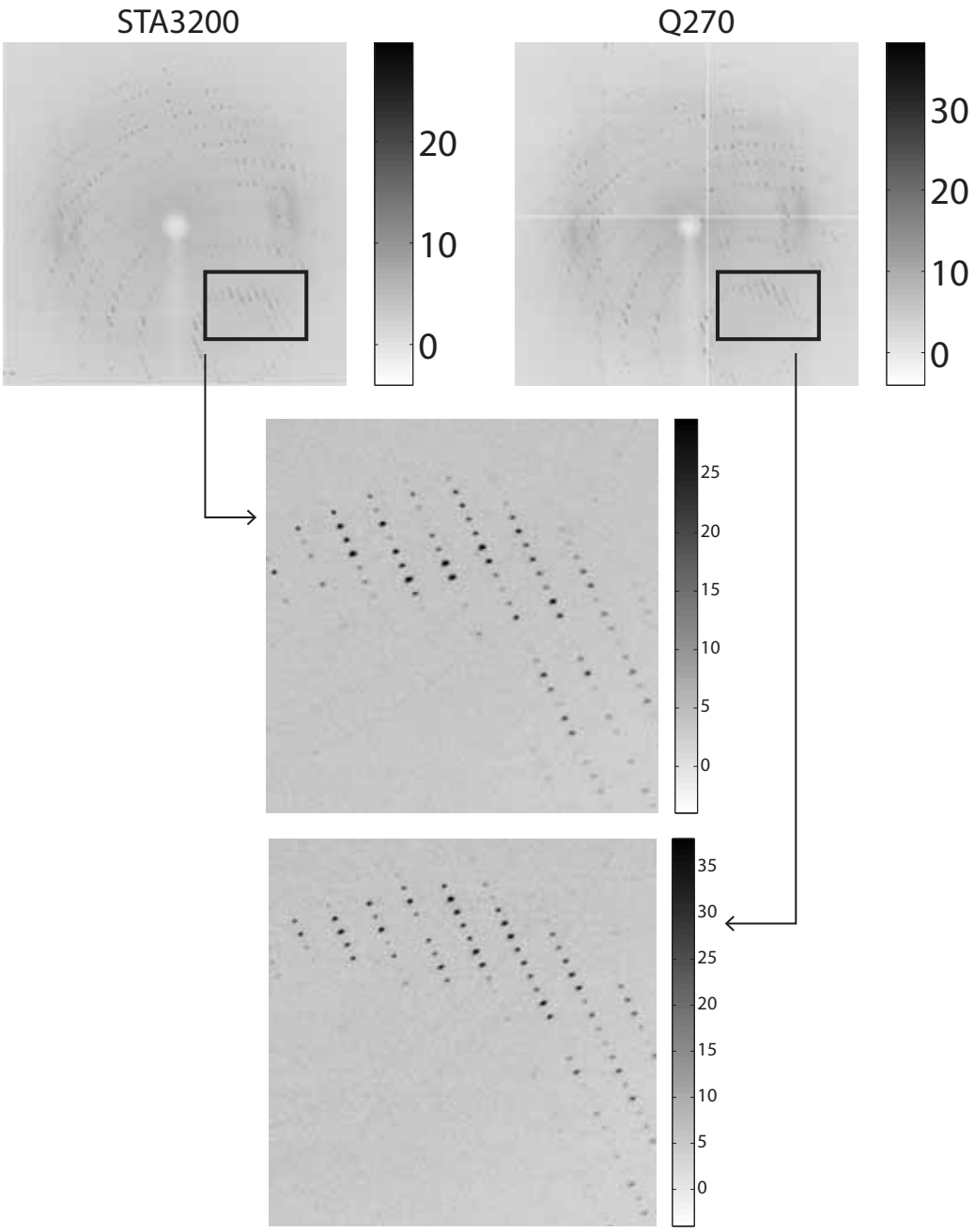

Figure 5.4: Comparison of diffraction pattern from sample Thau13. For this sample, the beam size was 100 μm and the sample-to-detector distances were set to give equal solid angle per pixel per detector. The boxed regions in the large images at top are magnified at bottom. The grayscale is cast in units of number of photons, with the maximum of the scale set to 5% of the maximum intensity in the frame.

Magnified regions, containing only a few diffraction spots, are shown for each of the four experimental configurations for both detectors in Figures 5.5, 5.6, 5.8, and 5.7. One feature immediately obvious to the eye is the greater detail visible in the Bragg spots on the direct-detection CCD, particularly in the 20 μm beam data. The details within the Bragg spots are true features reflecting the beam profile and crystal shape. Details within Bragg spots have been used in XFEL experiments to recover information about the crystal shape [75].

The data in Figures 5.5 and 5.6 were collected using the 20 μm capillary-focused beam. The distinctive beam profile produced by the focusing capillary can clearly be seen on both detectors when the colorscale is set to a maximum of 50% of the maximum intensity within the region. These details within the diffraction spots persist in the STA3200 data as the colorscale is compressed, whereas they quickly fade in the Q270 data. Additionally, spots on the STA3200 remain well-separated even at a 1% contrast level, while the same spots on the Q270 are clearly merged. This is true in the equal-angle as well as equal-distance datasets.

The data in Figures 5.8 and 5.7 was taken with the 100 μm beam. The shape of the Bragg spots is slightly more well-defined on the STA3200 than on the Q270. The non-circular outline of the diffraction spots in Figure 5.8 is due to the crystal splitting mentioned above. Because the 100 μm beam produces more background scatter than the 20 μm beam, the background intensity is higher on each detector at each sample-to-detector distance than in the 20 μm data; this is particularly noticeable in the 1% contrast images. In spite of this increased background scatter, the merging of neighboring diffraction spots on the Q270 versus the well-maintained separation on the STA3200 can still be discerned.

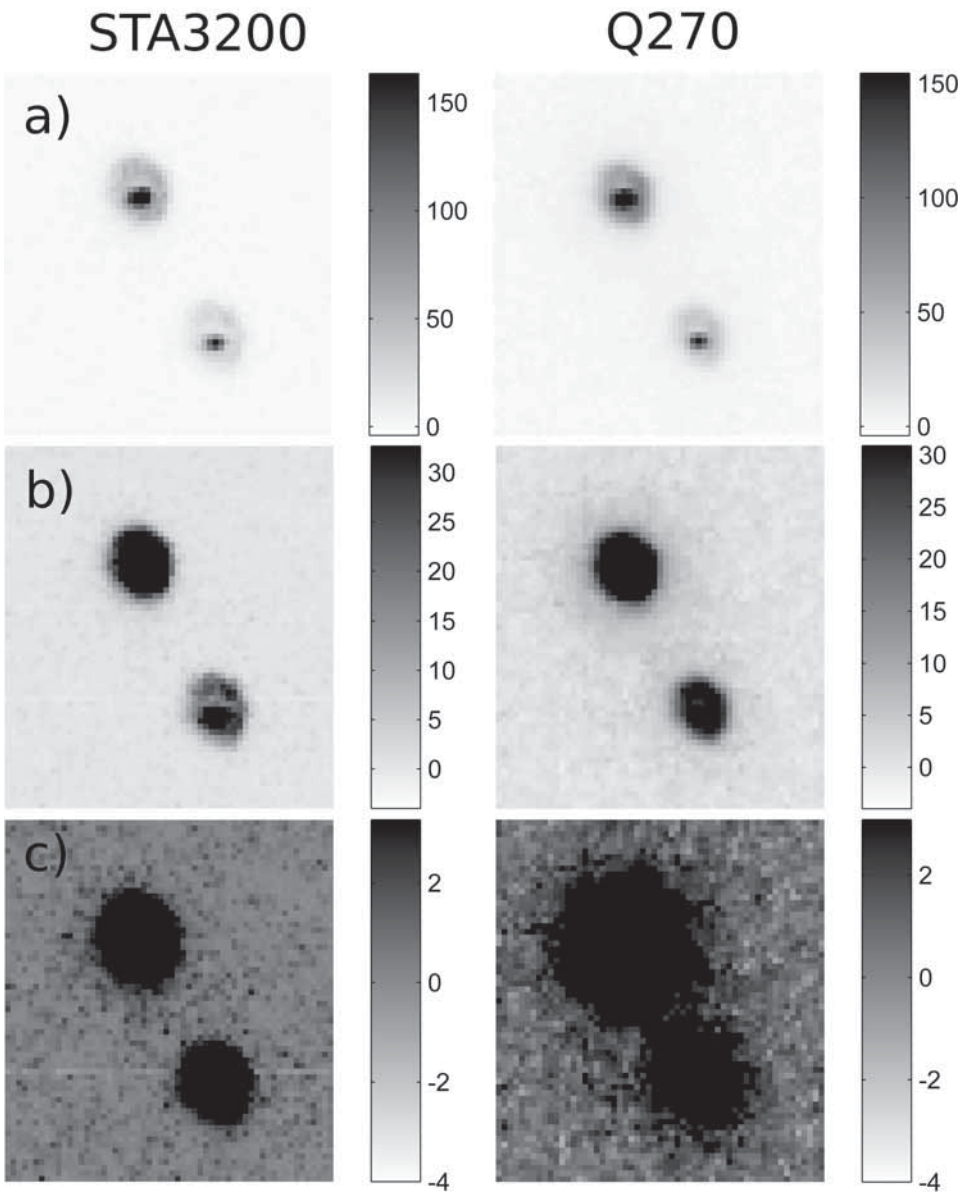

Figure 5.5: Comparison of diffraction spots from sample Thau4. For this sample, the beam size was 20 μm and the sample-to-detector distances were set to give equal solid angle per pixel per detector. The grayscale is cast in units of number of photons. In each pair of images, the same region is shown for the STA3200 on the left and the Q270 on the right. In each pair, the maximum of the colorscale is set to a percentage of the maximum intensity in the ROI: a) 50%, b) 10%, c) 1%.

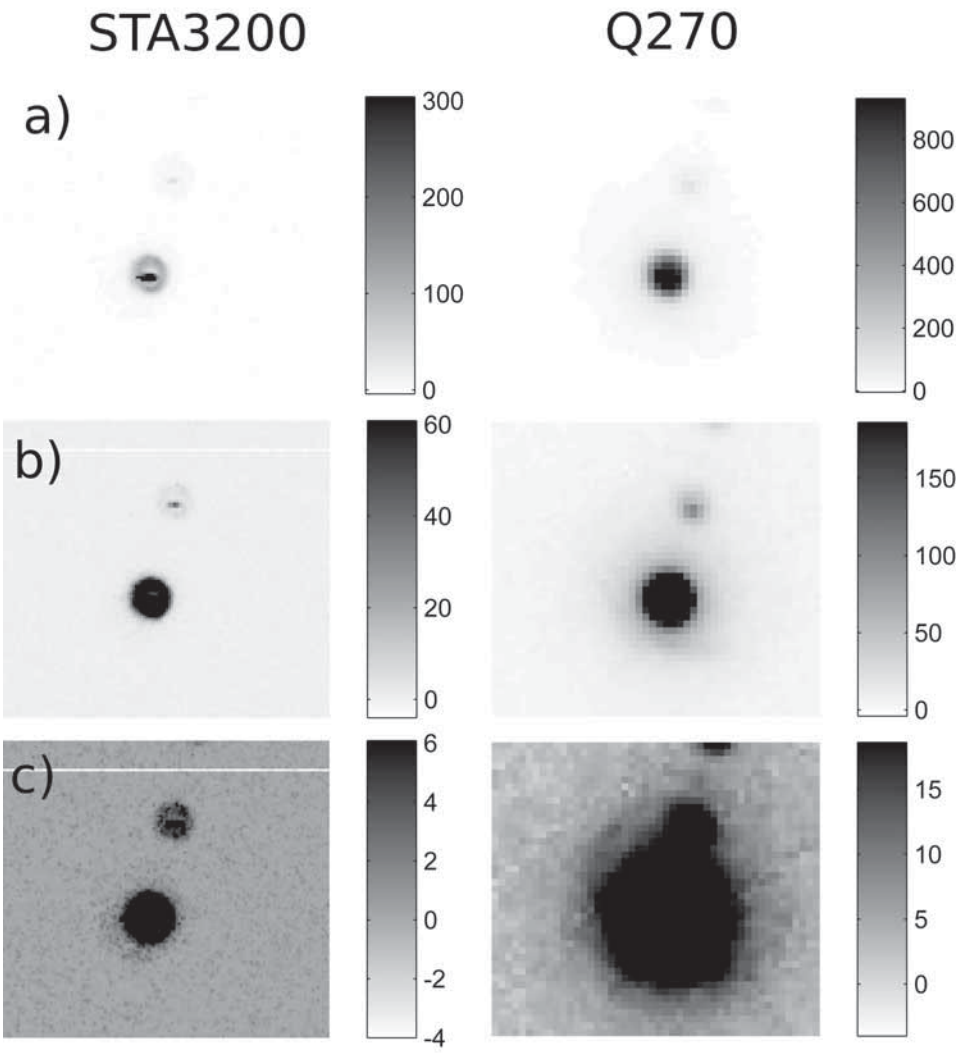

Figure 5.6: Comparison of diffraction spots from sample Thau6. For this sample, the beam size was 20 μm and the sample-to-detector distances were equal. The grayscale is cast in units of number of photons. In each pair of images, the same region is shown for the STA3200 on the left and the Q270 on the right. In each pair, the maximum of the colorscale is set to a percentage of the maximum intensity in the ROI: a) 50%, b) 10%, c) 1%.

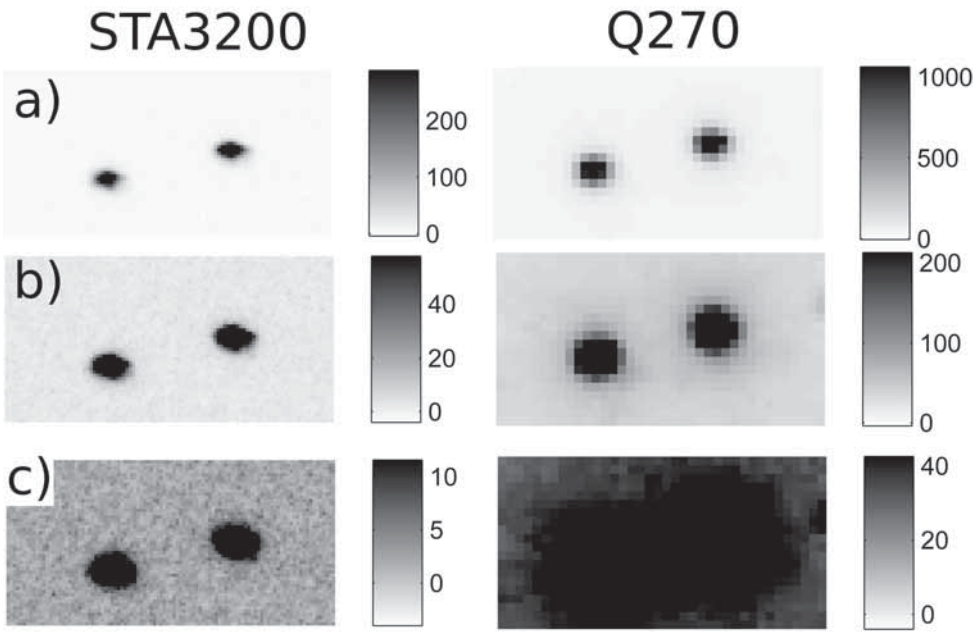

Figure 5.7: Comparison of diffraction spots from sample Thau9. For this sample, the beam size was 100 μm and the sample-to-detector distances were equal. The grayscale is cast in units of number of photons. In each pair of images, the same region is shown for the STA3200 on the left and the Q270 on the right. In each pair, the maximum of the colorscale is set to a percentage of the maximum intensity in the ROI: a) 50%, b) 10%, c) 1%.

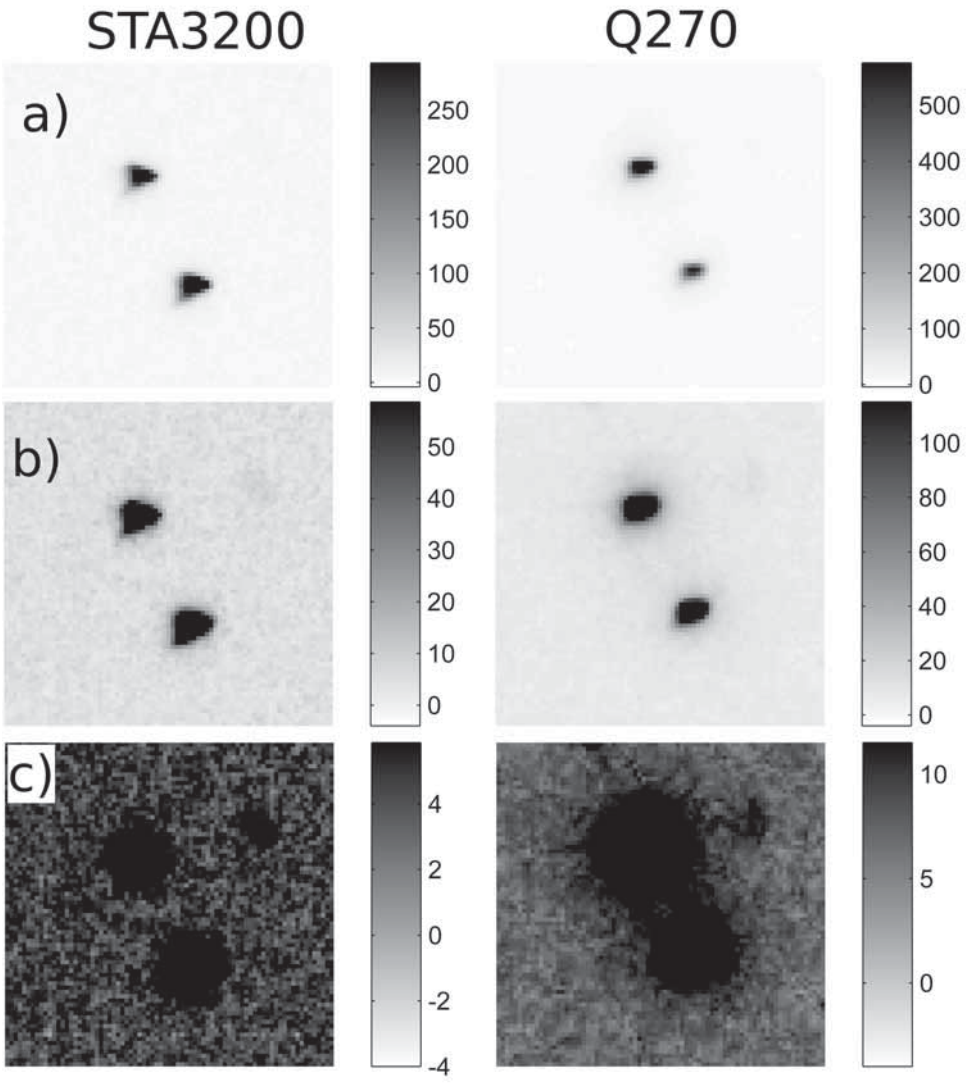

Figure 5.8: Comparison of diffraction spots from sample Thau13. For this sample, the beam size was 100 μm and the sample-to-detector distances were set to give equal solid angle per pixel per detector. The grayscale is cast in units of number of photons. In each pair of images, the same region is shown for the STA3200 on the left and the Q270 on the right. In each pair, the maximum of the colorscale is set to a percentage of the maximum intensity in the ROI: a) 50%, b) 10%, c) 1%.

5.3 Conclusions

The successful collection of protein crystallographic data on the STA3200 has been demonstrated. In most cases, the merging statistics were slightly better than those obtained using a conventional phosphor-coupled CCD. Visually, diffraction spots were more clearly defined, and detail within spots was better-preserved, with the direct-detection CCD. These visual effects were more clearly demonstrated in the 20 μm beam data, confirming that the direct detection CCD is better optimized to data collection using small beams.

Looking beyond the use of the diffraction pattern for structure determination, fine details within and between diffraction spots can be used to recover information about crystal shape and disorder. Diffraction topography is a method in which a crystal is illuminated by a low-divergence monochromatic beam. The diffraction spots are then real-space images of the two-dimensional projection of the crystal. These projections, when recorded with sufficient spatial resolution, can be used to study the disorder present in the crystal [76]; for example, to determine whether a particular crystal suffers from macroscopic disorder (e.g. splitting or twinning) or microscopic disorder (e.g. high mosaicity). The fine structure in and around diffraction spots has also been used in analysis of data collected during protein nanocrystallography experiments at the LCLS [75], as mentioned above, using the ASG pn-CCD described in Section 1.3.2. Here, two details about the crystals were extracted from fine structure in the diffraction pattern. First, the number of unit cells per side of the crystal was determined by counting the diffraction fringes recorded between neighboring Bragg peaks. These fringes appear at a spacing of $1/N$ times the diffraction peak spacing, where N is the number of unit cells on a side. Second, when coherent x-rays

are used, each diffraction spot and the region around it represents the Fourier transform of the crystal shape. By feeding these patterns through an iterative phase retrieval algorithm, an image of the crystal shape was obtained.

CHAPTER 6

HOME LABORATORY EXPERIMENTS AND SIMULATIONS

6.1 Introduction

Protein crystallography experiments, especially those involving microcrystals, involve a multitude of experimental factors that are difficult to control. In particular, x-ray microbeam and crystal quality and alignment presented obstacles in the effort to evaluate the performance of the STA3200 in the context of protein microcrystallography, given the resources available. The difficulty of reliably collecting data using microcrystals precluded a detector comparison experiment using microcrystallographic data, as data quality and characteristics such as spot size and crystal quality could not be sufficiently well controlled.

In order to make a more rigorous study of the detector response, a more reliable, easily-controlled source of small x-ray spots was needed. Therefore, a comparison experiment was performed using a home laboratory x-ray source and x-ray opaque pinhole masks to produce known patterns of spots on the detector. The goal of this experiment was to assess the performance of the STA3200 as the x-ray spot size and intensity were decreased in a controlled fashion, with intensity down to, ideally, one photon on average per spot per frame, and spot size down to 25 μm in diameter.

Additionally, given the flaws in the current STA3200 prototype, the most pressing question is whether an improved version of the detector should be built, and if so, what improvements should be prioritized. Since the STA3200 design effort began in 2008, the deep-depletion CCD projects at LBNL and the

ASG (described in Chapter 1) have progressed significantly, providing new benchmarks for what specifications a deep-depletion CCD should be able to meet. Additionally, the PILATUS photon-counting detectors have gained exposure and popularity in the field of crystallography, and the EIGER detector [77], based on the same platform but with smaller pixels (75 μm $\times$ 75 μm) will be commercially available soon as of this writing. These photon-counting PADs perform very well, especially under low-flux conditions when count rate limitations are not a concern. The question arises whether a revised version of the STA3200 would offer significant benefits compared to a photon-counting PAD in the context of protein microcrystallography, especially as the available PAD pixel sizes begin to shrink.

One could attempt to compare the current STA3200 prototype to a PILATUS detector using home laboratory pinhole data as described above. However, the undepleted layer on the x-ray entrance side of the STA3200 is a significant barrier to a meaningful experimental comparison. Most of the in-house characterization measurements described in Chapter 4 were performed using the Mo x-ray tube, where most of the Kα x-rays pass through the undepleted layer. At this x-ray energy, the STA3200 shows fairly good single-photon resolution and a PSF approaching 20 μm FWHM, as desired in a thick deeply-depleted Si sensor. However, as shown in Section 3.3.1, the Mo x-ray tube, even when heavily filtered, has a relatively broad spectrum. Photon-counting and photon-integrating detectors treat broad spectrum sources in fundamentally different ways. In a photon-integrating detector (such as a CCD), the signal recorded by a pixel is proportional to the total energy absorbed, whereas in a photon-counting detector each absorbed photon that exceeds the user-defined energy threshold will be registered as one "hit"; the energy information is lost. One could set the energy

threshold very close to 17.5 keV in order to reject the lower-energy photons, but this would exacerbate the problem of lost photon counts due to charge sharing at pixel boundaries (described briefly in Chapter 2, and in greater detail later in this chapter). Photon-counting PADs are normally operated with the threshold set to 50% of the x-ray energy of a monochromatic source to minimize photon over- or under-counting at pixel boundaries.

In theory, the Cu tube with a Ni filter would be an ideal home source to use for a comparison experiment, since the Kα line is at 8 keV and the filtered spectrum is very nearly monochromatic. However, 8 keV x-rays are strongly absorbed by the undepleted layer on the STA3200, as was shown in Chapter 4. Therefore, a comparison experiment using the Cu tube source was not pursued with this prototype. Instead, pinhole data using the Mo tube source will be presented for the STA3200 to give a qualitative assessment of the effect of smaller spot sizes and lower intensities on the performance of the current prototype. To compare a potential re-designed version of the STA3200 to the PILATUS and EIGER, simulated spot data will be used.

6.2 Pinhole measurements with the STA3200

In Chapter 3, the DQE was described as a metric for evaluating detector performance. The DQE quantifies the impact of detector noise and systematics on the SNR of a measurement. Evaluation of the DQE requires independent knowledge of the signal incident on the detector face. During the experiment described in this section, the incident flux was not measured directly. In the absense of precise knowledge of the incident flux for each measurement, a mod-

ified version of the DQE will be used to evaluate the detector performance. While the number of photons incident on the detector face is unknown, the number of photons stopped in the sensor can be computed from the recorded signal. The *stopped DQE* (sDQE) will be defined as

$$\begin{aligned} \text{sDQE} &= \frac{(S_{out}/N_{out})^2}{\left(S_{in,stopped}/N_{in,stopped}\right)^2} \\ &= \frac{(S_{out}/N_{out})^2}{S_{in,stopped}} \end{aligned} \tag{6.1}$$

where S_{out} and N_{out} are the signal and noise recorded by the detector, $S_{in,stopped}$ is the number of photons stopped in the detector, and $N_{in,stopped}$ is the uncertainty in the number of stopped photons. The stopped photons are assumed to obey Poisson statistics, i.e. $N_{in,stopped} = \sqrt{S_{in,stopped}}$. Analysis of the sDQE explicitly ignores the efficiency of the detector, but still gives information about detector noise and systematics. The goal of the following measurements was to assess the sDQE of the STA3200 for a range of spot sizes and intensities.

6.2.1 Experimental setup

The Mo tube was used as the x-ray source, biased at 25 kV, with drive current ranging from 0.05 mA to 0.6 mA. These settings were combined with integration times ranging from 1 ms to 300 s, and a Zr filter thickness of 100, 200 or 400 μm, to give as wide a range of intensities per spot per frame as possible, ideally ranging from one photon/spot/frame on average up to the onset of pixel saturation. The spectrum of photons incident on the detector face, after the Zr filter and the carbon fiber window, is shown in Figure 6.1.

The x-ray source was 1.0 m away from the mask. The masks were fixed to

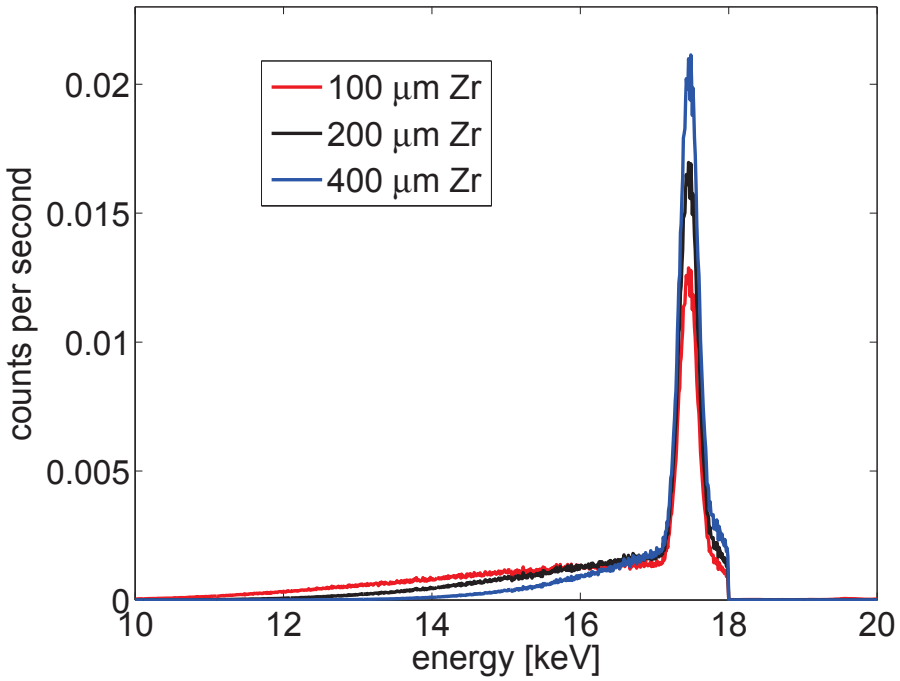

Figure 6.1: Calculated Mo tube spectrum (tube bias 25 kV) incident on the STA3200 face, accounting for the Zr filter and carbon fiber window transmissions. The spectra have been normalized to the total number of counts, and the energy scale has been truncated to clearly show the region of interest.

adapter plates on the front of the x-ray flight path in order to ensure that they were stationary with respect to the source. The detector was placed as close to the masks as physically possible to reduce parallax.

Three x-ray opaque masks were used: a square array of 25 μm diameter pinholes on a 300 μm pitch on tungsten foil, a square array of 150 μm diameter pinholes on a 440 μm pitch on tungsten foil, and an array of 300 μm diameter pinholes on a hexagonal lattice with unit cell dimension 1.9 mm on gold-plated copper. The 300 μm mask has three larger pinholes that could be used for spot identification; on the other two masks, strips of aluminum foil were used to create a fiducial pattern. The ability to identify individual spots accurately was necessary in order to measure and correct for spot size differences.

6.2.2 Accounting for pinhole mask variations

The goal of this experiment was to measure the variation in the pinhole spots as they are recorded by the detector and by doing so, extract a measure of the detector performance. However, the pinholes in each mask vary in size due to manufacturing tolerances. If this variation is not removed from the data, it could easily dominate the measured spot intensity variation.

The STA3200 was used to generate maps of the pinhole areas on each of the three masks. Each pinhole mask was imaged with intensity high enough to give better than 0.5% source-limited accuracy overall (i.e., more than 40000 photons per pinhole over the entire dataset). In order to average out local variations in detector sensitivity, images were taken at multiple detector positions. The computed pinhole area variations are listed in Table 6.1.

Pinhole diameter	Pinhole area variation
300 μm	2.4%
150 μm	0.9%
25 μm	10.3%

Table 6.1: Measured pinhole area variations.

Physical limitations of the STA3200 housing and support electronics assembly restricted movement of the detector to horizontal translations only. To verify that this limited range of motion did not compromise the pinhole area measurement, the measurement was repeated for the 300 μm mask using the MMPAD 2×3 detector, which could easily be moved both horizontally and vertically. The MMPAD data yielded a pinhole area variation of 2.7%, compared to 2.4% from the STA3200 data. The computed pinhole areas vary between the two detectors by, on average, about 1.3%. However, major features of the mask were

captured in both pinhole area maps: for example, a horizontal crease near the mask center, which can also be seen by visual examination of the mask. Between the time the STA3200 pinhole area map data and the MMPAD pinhole area map data were taken, the mask had been removed and replaced on the x-ray tube flight path several times, and the raw images show a 6% difference in mask tilt. As such, each pinhole is sampling one portion of the x-ray flood field in the STA3200 dataset and a slightly different portion in the MMPAD dataset. This may account for the variation between the two pinhole area maps. Meanwhile, the masks were not moved between acquisition of the pinhole area map data and the sDQE data on the STA3200. It was concluded that the pinhole area maps generated from the STA3200 data were sufficiently accurate for the purposes of the following calculations.

6.2.3 Data collection and analysis

For each mask, a series of 20 to 50 static images were taken at each of a range of intensity settings (varying integration time, x-ray tube current and filter thickness). The choice of number of frames was driven by a compromise between time required to collect the data and the need to have a large population of spot measurements over which to obtain statistics. A set of background exposures was taken for each unique integration time on each day (to capture shifts in temperature, electronic pedestal after power cyclings, etc.).

To analyze the data, an averaged background frame was subtracted from each x-ray frame, and the data was corrected for gain variation between the 8 readout amplifiers. The pinhole locations were determined from the aver-

age background-subtracted image for each set of conditions. Next, the signal recorded through each pinhole in each frame was computed and stored. For the 25 μm pinholes, the recorded signal was summed over a radius of 1.5 pixels; for the 150 μm pinholes, over a radius of 5 pixels; for the 300 μm pixels, over a radius of 10 pixels. The pinhole intensities were corrected for pinhole area variation and for global frame-to-frame variation in average intensity, to account for fluctuation in the x-ray source intensity. Each corrected intensity measurement was considered as a member of the population over which the average pinhole intensity, $< S_{norm} >$, and standard deviation, $\sigma_{S_{norm}}$, were computed. These quantities correspond to the ouput signal, S_{out}, and the output noise, N_{out}, in Equation 6.2. To screen out defective pixels and cosmic rays, pinhole intensities deviating from the average by more than 3 standard deviations were discarded.

The number of photons stopped by the detector ($S_{in,stopped}$) was computed from $< S_{norm} >$ and the detector gain. The source was approximated as monochromatic, with photon energy computed as the weighted average of the spectrum measured by the SDD with appropriate Zr filter thickness and carbon window attenuation. The weighted average energies are 16.34 ± 0.02 keV for the 100 μm Zr filter, 16.78 ± 0.01 keV for the 200 μm Zr filter, and 17.166 ± 0.002 keV for the 400 μm Zr filter. The uncertainties arise from the uncertainty in the thickness of the SDD sensor with which the spectra measurements were made.

From the uncertainties in the detector gain, the pinhole area normalization, and the frame-to-frame global intensity fluctuations, it is possible to calculate the uncertainty of the sDQE, as detailed in Appendix B. The primary goal of the uncertainty analysis was to assess the impact of the uncertainty in the detector gain on the measurement. As will be seen, the computed sDQE uncertainties

were generally small compared to the variation between sDQEs for different pinhole sizes and intensities, indicating that the uncertainty in the detector gain is not a limiting factor in this analysis.

The question of local background subtraction

In analysis of protein crystallography data, the local background scatter around each diffraction spot would be averaged and subtracted from the integrated spot intensity. The purpose of this is to remove background scatter (from air, fluid surrounding the sample, etc.) from the spot measurement, in order to recover information about the crystal itself. In pinhole mask data, such background scatter does not exist in a meaningful way; there is only full transmission of photons through the pinhole, or (nearly full) attenuation of photons by the mask. Because the photon energy used here is relatively high, there is a small amount of transmission through the masks, especially for long integration times. Pixels that are completely shielded by the mask can record these transmitted photons. Due to the finite detector point spread, this signal can bleed into the edges of the illuminated pinhole spots.

The mask transmission was evaluated for each dataset. The signals recorded by pixels in areas of the detector completely shielded by the mask have two components: dark current, which should be eliminated through background subtraction, and any photons that are transmitted through the mask. An area roughly equivalent to that of a single pinhole was selected in a region of the detector completely shielded by the mask. The signal recorded in this area was integrated and averaged over all background-subtracted frames. The magnitude of the transmitted signal, normalized to the average illuminated pinhole

intensity, is plotted in Figure 6.2. The transmitted signal is non-zero, but in most cases is a small fraction of the illuminated pinhole intensity.

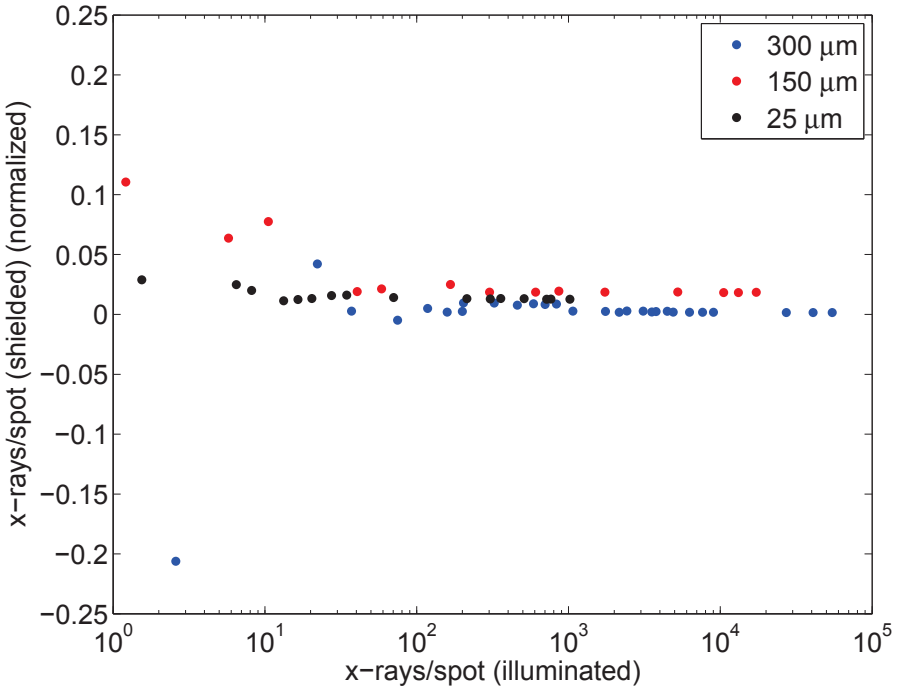

Figure 6.2: Pinhole mask transmission.

The negative value for the lowest-intensity datapoint in the 300 μm dataset indicates a problem with the background-subtraction for that dataset. Further inspection of the raw frames suggest that the dark current level had shifted between the time when the x-ray data and the background frames were taken, with higher dark current in the background frames. Although the increase in dark current was small, when a large number of pixels are summed during integration of the 300 μm pinholes, small negative pixel values accumulate and become significant. This problem appears to be limited to the lowest-intensity 300 μm pinhole dataset. Aside from this outlier, the signal transmitted through the mask was generally small, and should only affect the outer edges of the

illuminated pinholes. Therefore, local background subtraction was not incorporated into the integration of pinhole intensities.

6.2.4 Results

The sDQE curves for all three pinhole sizes are plotted in Figure 6.3, along with the sDQE curves expected from read noise considerations only.

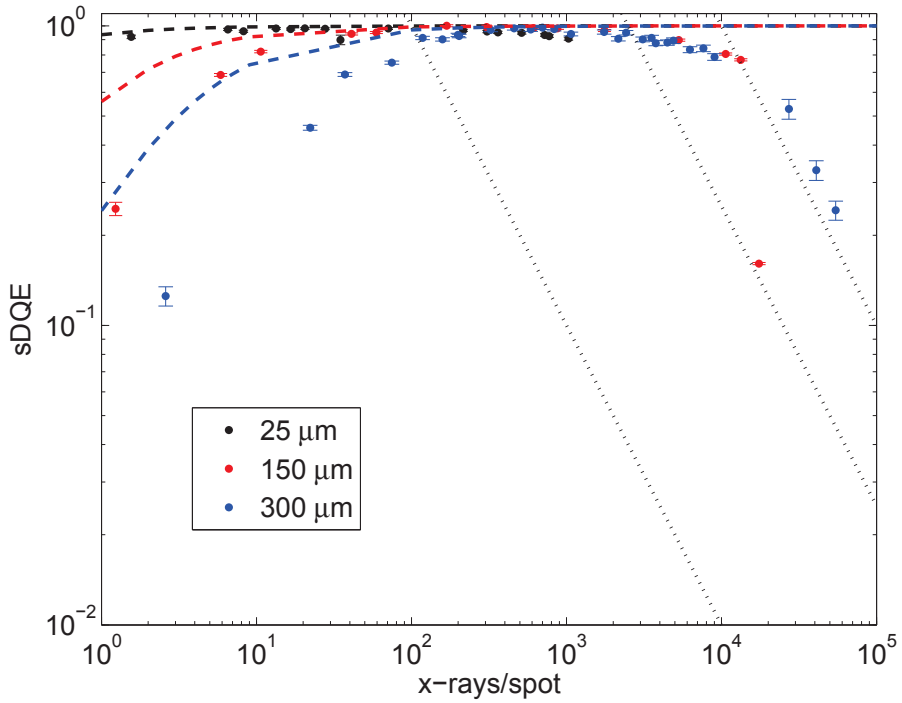

Figure 6.3: STA3200 sDQE curves for 25 μm, 150 μm, and 300 μm pinhole spots. The dashed lines are the expected values of the sDQE for the corresponding pinhole size (i.e., the black dashed line corresponds to the 25 μm pinholes). The dotted black lines are sDQE that would be obtained if the spots were measured to an accuracy of 10%, 2% and 1%.

At low intensity, as expected, the detector performance is best for the 25 μm spots due to the decreased read noise in the pinhole sum. The sDQE for

the 25 μm pinholes closely matches the expected sDQE at low intensity, and is near unity across the accessible intensity range, indicating that the read noise is small enough that it has little impact on the data quality for very small feature sizes. Due to pixel saturation, data was not collected for the 25 μm pinholes beyond 1000 photons per spot. At high intensity, the 150 μm spot sDQE curve approaches the 1% accuracy level, and the 300 μm sDQE curve exceeeds it. These two sDQE curves are also close to unity across a wide range of intensities, from about 100 to 2000 photons per spot.

The intensity at which the sDQE curves begin to turn back down indicates the point at which detector systematics other than read noise become important. The 300 μm and 150 μm curves turn over around 2000 photons per spot. The sharp downturn between the two highest-intensity datapoints in the 150 μm curve indicates that some pixels may be reaching saturation in the highest-intensity dataset (about 2×10^4 photons per spot). The 25 μm curve appears to turn over around 200 photons per spot.

6.3 Comparison of a re-designed direct-detection CCD to a photon-counting PAD

As was established in Chapter 4, the current STA3200 prototype is clearly flawed and is not ideal for scientific use. There remains the possibility of commissioning a re-designed version of the CCD, with improvements to correct the fundamental problems with the current prototype. This section attempts to assess whether this is a worthwhile goal, in light of the fact that a re-designed direct-detection CCD would be competing not only with phosphor-coupled CCDs, but

also with newer photon-counting PADs.

6.3.1 Goals for STA3200 re-design

If the STA3200 were to be re-designed, the first priority would be to improve the guard ring structure in order to fully deplete the sensor. This would improve both the efficiency and the spatial resolution of the detector. A fully-depleted 600 μm thick silicon sensor would have 90% stopping power or better for x-rays up to 12.6 keV, with near-unity stopping power at 10 keV. As described in Section 4.3.4, a 10 kΩ-cm, 600 μm thick p-type sensor, cooled to 205 K, would have a Gaussian point spread function with a standard deviation of roughly 10 μm at an overdepletion bias of 10 V (i.e., an applied bias of 350 V). The detector systematics would also be reduced. In the current prototype, doping inhomogeneities lead to variation both in pixel area and pixel sensitivity. In a fully-depleted sensor, the latter effect would be eliminated, leaving only pixel area distortions, which can be corrected for to some extent using the pixel boundary mapping technique described in Section 3.7. Some variation in pixel sensitivity could persist due to variation in the sensor thickness itself, but should be significantly less than the sensitivity variation in an under-depleted sensor.

The second priority would be to reduce the pixel read noise. As mentioned in Section 4.4, one relatively simple modification would be to place the analog-to-digital converters on the CCD headboard, rather than on a separate circuit board. The long cables which carry the CCD output signals to the ADCs in the current prototype are long and susceptible to noise pickup. It is not clear by what factor this would improve the read noise, but it would undoubtedly help.

The CCD output amplifiers themselves could also be modified to reduce the read noise. This is a more complicated proposition with potential detrimental effects on the pixel well depth. The read noise, cast in units of electrons, is inversely proportional to the sensitivity of the output stage [39]: for low read noise, a large sensitivity is required. At the same time, the sensitivity of the output stage must be sufficiently small that the pixel full well charge can be converted into a reasonable voltage. The amplifiers in the current prototype can output up to 2 V with good linearity and have a sensitivity of 1 μV/e-. If the pixel well depth is fixed at 1.4×10^6 electrons, as in the current prototype, this allows a maximum sensitivity of 1.4 μV/e- at the output stage. This increase in sensitivity would reduce the noise to about 70% of its current value, on top of whatever improvement was gained by digitizing the output signals close to the chip.

The following simulations assume a re-designed direct-detection CCD with a 600 μm fully-depleted sensor giving 99% efficiency at 10 keV and a 10 μm PSF, and with read noise reduced by one-third from the current value (down to 256 e-) through a combination of amplifier modification and repositioning of the ADCs. The full well is unchanged from the current value of 1.4×10^6 e-, which would allow for the collection of about 500 10 keV photons per pixel.

6.3.2 Detector systematics in photon-counting PADs

Photon-counting PADs are subject to the same sensor non-uniformities as other direct-detection semiconductor devices. They also suffer from a fraction of dead area in each pixel due to the combination of charge sharing and energy thresh-

olding. Consider the typical operating mode, where monochromatic illumination is used and the pixel threshold is set to 50% of the x-ray energy. In this case, if the pixel's energy-thresholding comparator is perfectly calibrated, the charge generated by x-rays that hit on or near pixel corners will be split between four pixels, and the photon will not be counted by any of them.

The location and extent of the pixel dead areas can be calculated by using the PSF to compute the fraction of photo-generated charge collected in a given pixel as a function of the location of the initial photon hit. Suppose a photon is incident on the detector at position (x_0, y_0). The fractional amount of charge collected by a pixel spanning x coordinates x_1 to x_2 and y coordinates y_1 to y_2 is given by

$$I_{pix} = \int_{x_1}^{x_2} \int_{y_1}^{y_2} \frac{1}{2\pi\sigma_x\sigma_y} \exp\left(-\left[\frac{(x-x_0)^2}{2\sigma_x^2} + \frac{(y-y_0)^2}{2\sigma_y^2}\right]\right) \mathrm{d}x\mathrm{d}y \tag{6.2}$$

I_{pix} is shown for a range of x_0, y_0 in Figure 6.4 for the PILATUS and EIGER pixels, assuming a 320 μm thick sensor with 6 μm PSF, as reported in [49].

If a photon hits the pixel at a location such that I_{pix} is less than 0.5, the photon will be lost. This criterion can be used to generate a mask showing dead and collecting regions of arrays of pixels, assuming that the pixels are uniform in shape and size and that the energy-thresholding comparators are calibrated perfectly (i.e., this is a limiting, best-case scenario). These masks will be used to simulate the detection of photons by the PILATUS and EIGER, and are shown in Figure 6.5 for arrays of 5×5 pixels.

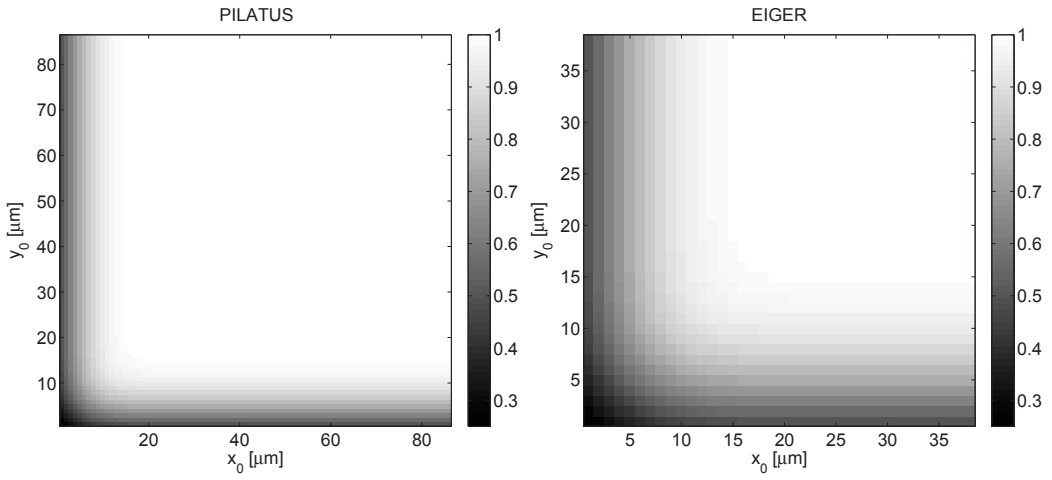

Figure 6.4: Fraction of charge (indicated by grayscale) collected by the PILATUS (left) and EIGER (right) pixels. In each case, a quarter of a pixel is shown, with the corner falling at (0,0). A PILATUS pixel is 172 μm on a side, and an EIGER pixel is 75 μm on a side.

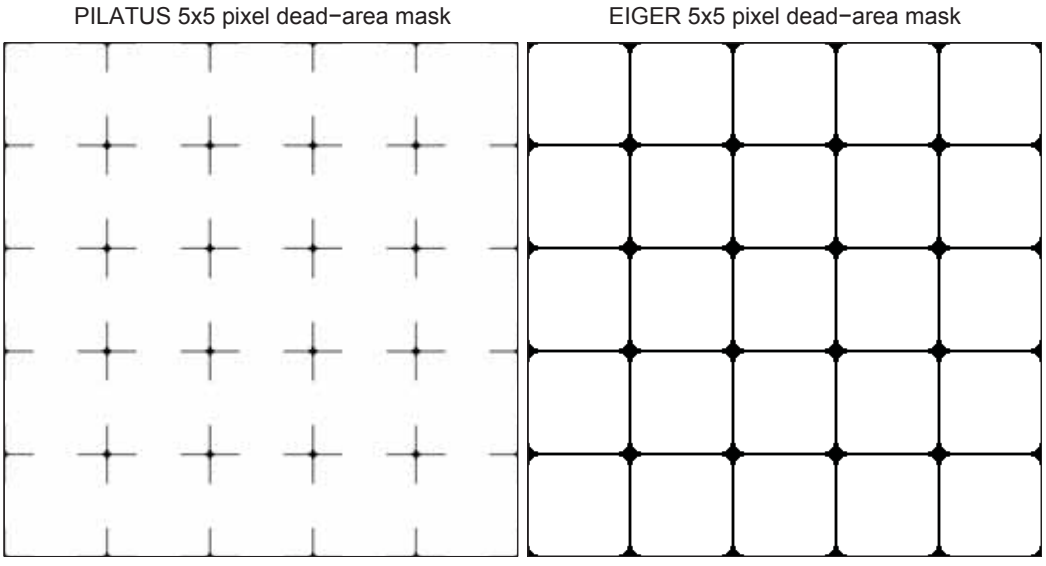

Figure 6.5: Dead-area mask for PILATUS and EIGER. Black areas are regions where photons are lost due to charge sharing. White areas are regions where photons are successfully detected and counted.

6.3.3 Simulation of spot detection

To assess the expected performance of the re-designed direct-detection CCD compared to that of a photon-counting PAD, the detection of spots similar to those used in the pinhole experiment described above was simulated for the PILATUS, the EIGER, and the proposed re-designed STA3200. The simulated DQE will be used as a metric of relative detector performance. This simulation will capture the effects of sensor efficiency, detector point spread and the resultant charge sharing, and read noise, but does not include a model of pixel-to-pixel sensitivity or area variations.

As in the pinhole experiment, spots 25, 150 and 300 μm in diameter and with intensity between 1 and 10^5 photons per spot were considered. Individual spots were simulated as follows. For spot diameter d and average intensity $< S >$, the number of incident photons was generated as a Poisson-noise distributed random number. The spot center was chosen to fall at a random location within the center pixel on a 5×5 pixel grid (for the PILATUS) or a 7×7 pixel grid (for the EIGER). (Because this simulation does not include pixel-to-pixel variations, restricting the spot center to fall within a single pixel is sufficient to fully capture the represented detector systematics, as long as the entire pixel area including edges and corners is included.) Photons were individually placed within a circle of radius $d/2$ at locations randomly generated from a uniform distribution. For each photon, the efficiency of the sensor was modeled by discarding the photon with probability equal to the transmission of the sensor (1% for the CCD, and 9% for the photon-counting PADs). For each combination of spot size and intensity, the simulation was repeated 5000 times to build up a population of simulated measurements.

For the photon-counting PADs, once the map of the dead areas is determined from the PSF, the location of a photon hit determines whether the photon is successfully detected. For the PILATUS and EIGER, the image containing the raw photon hits was compared to the dead-area mask and photons incident on dead areas were discarded. The effect is shown in Figures 6.6-6.9. The remaining photons were summed to determine the integrated spot intensity. The integrated spot intensity was recorded for each trial.

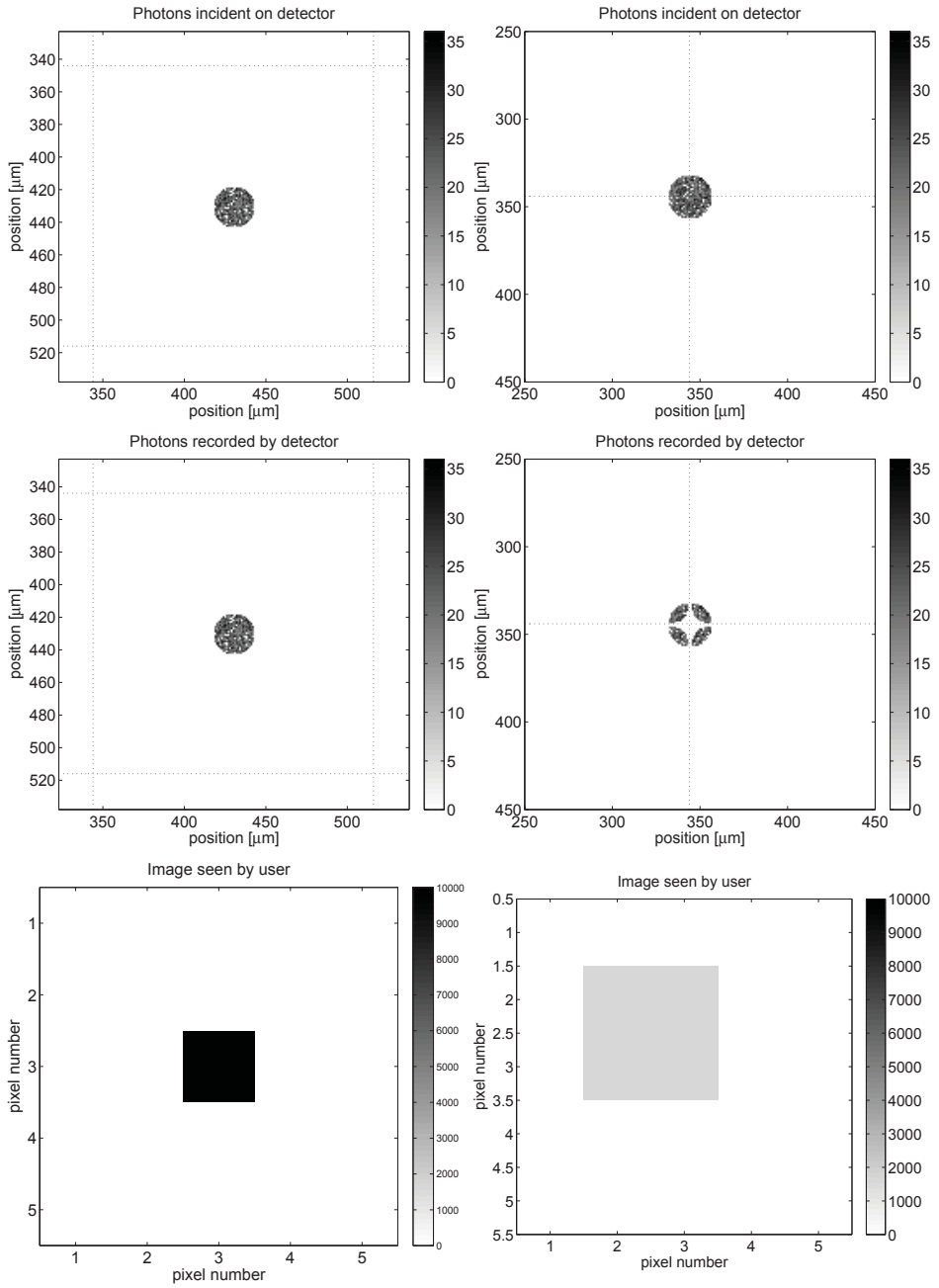

Figure 6.6: Simulated PILATUS performance for a 25 μm spot with 10,000 photons. In each column, the top image shows the photons incident on the detector face, the middle image shows the photons recorded by the detector, and the bottom image shows the pixelated image as seen by the user. The left column shows a spot centered on a pixel and the right column shows a spot centered on a corner. Grayscales are in units of photons. In the top two images in each column, pixel boundaries are indicated by dotted lines.

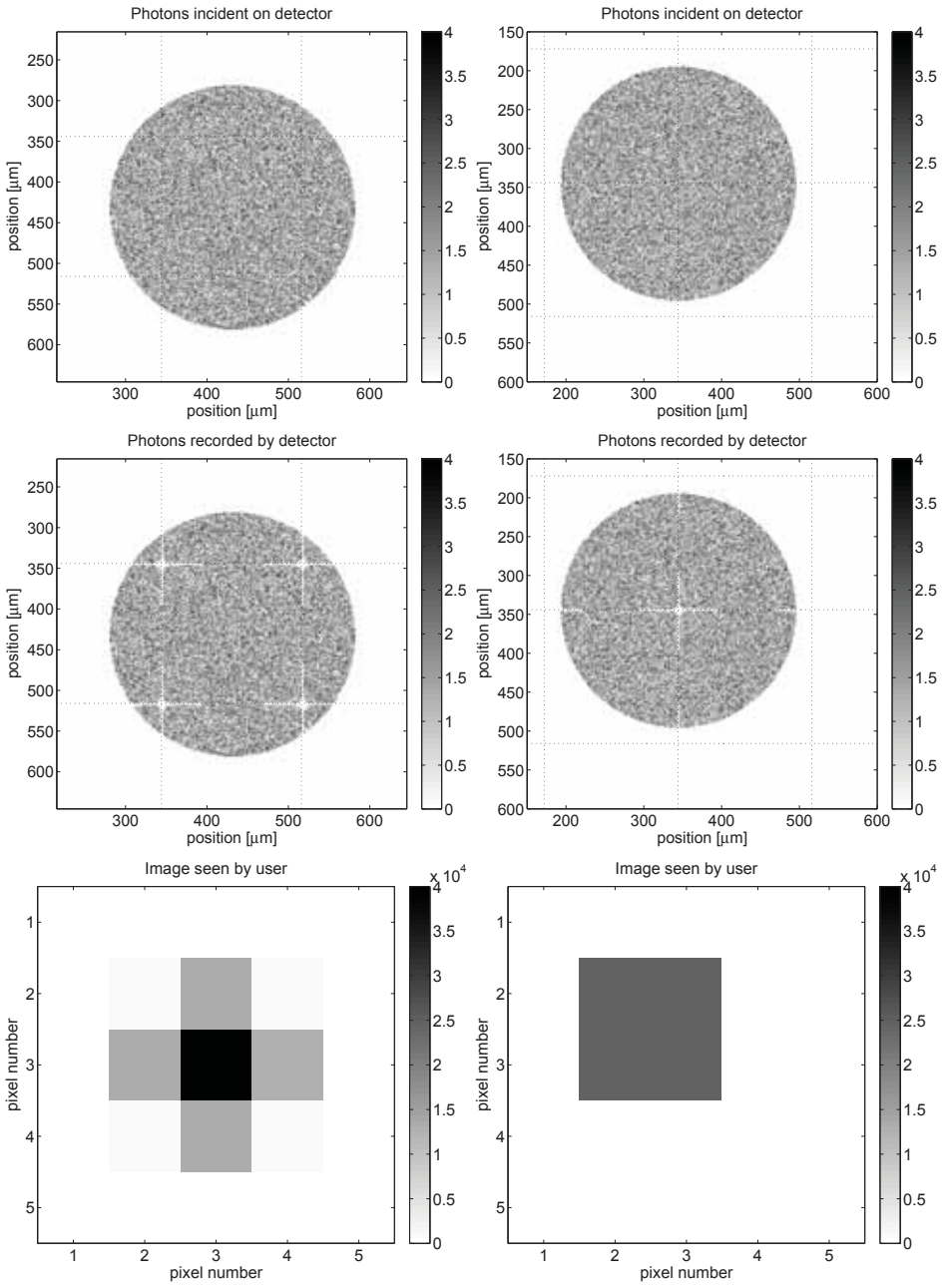

Figure 6.7: Simulated PILATUS performance for a 300 μm spot with 100,000 photons. In each column, the top image shows the photons incident on the detector face, the middle image shows the photons recorded by the detector, and the bottom image shows the pixelated image as seen by the user. The left column shows a spot centered on a pixel and the right column shows a spot centered on a corner. Grayscales are in units of photons. In the top two images in each column, pixel boundaries are indicated by dotted lines.

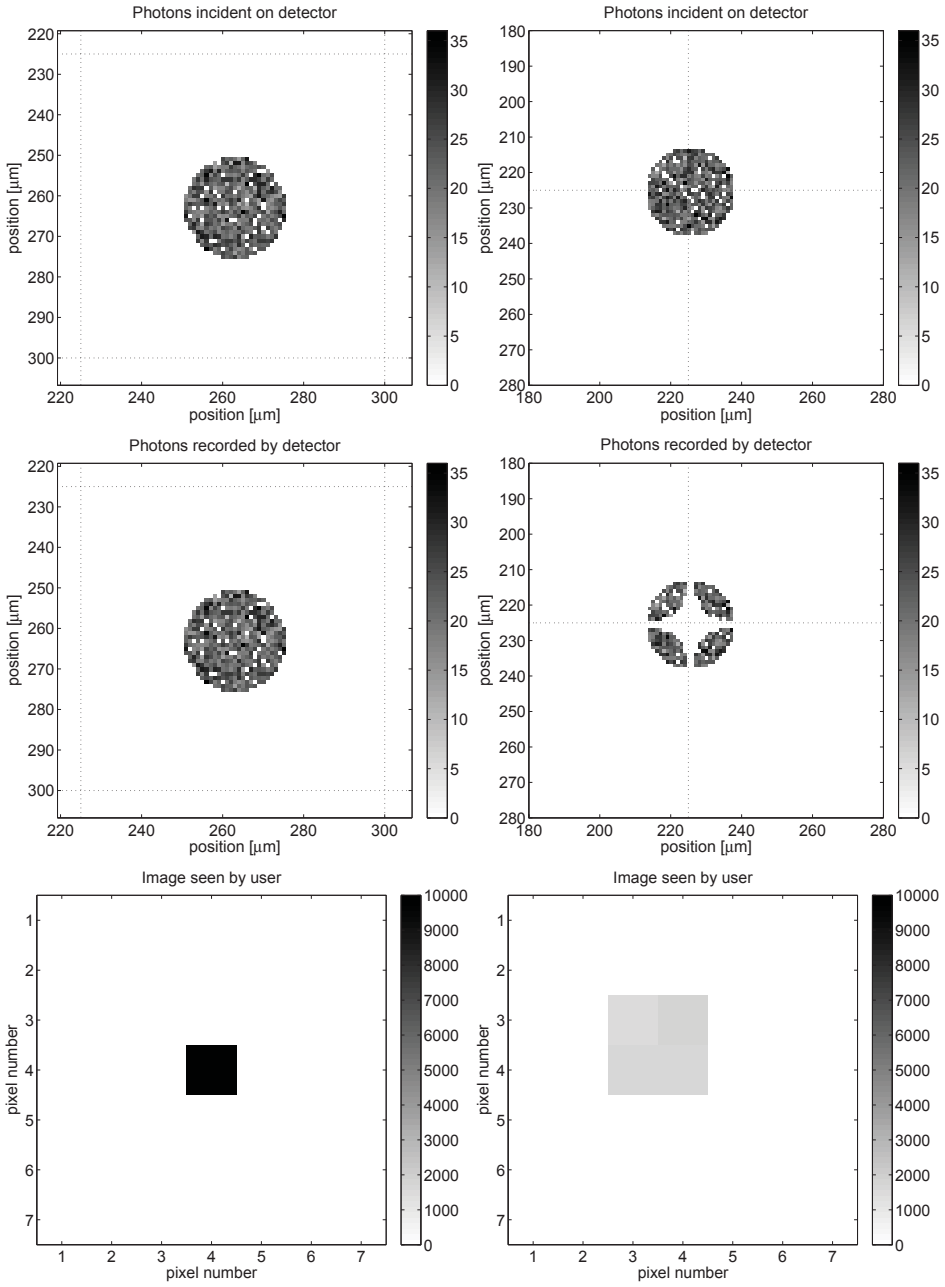

Figure 6.8: Simulated EIGER performance for a 25 μm spot with 10,000 photons. In each column, the top image shows the photons incident on the detector face, the middle image shows the photons recorded by the detector, and the bottom image shows the pixelated image as seen by the user. The left column shows a spot centered on a pixel and the right column shows a spot centered on a corner. Grayscales are in units of photons. In the top two images in each column, pixel boundaries are indicated by dotted lines.

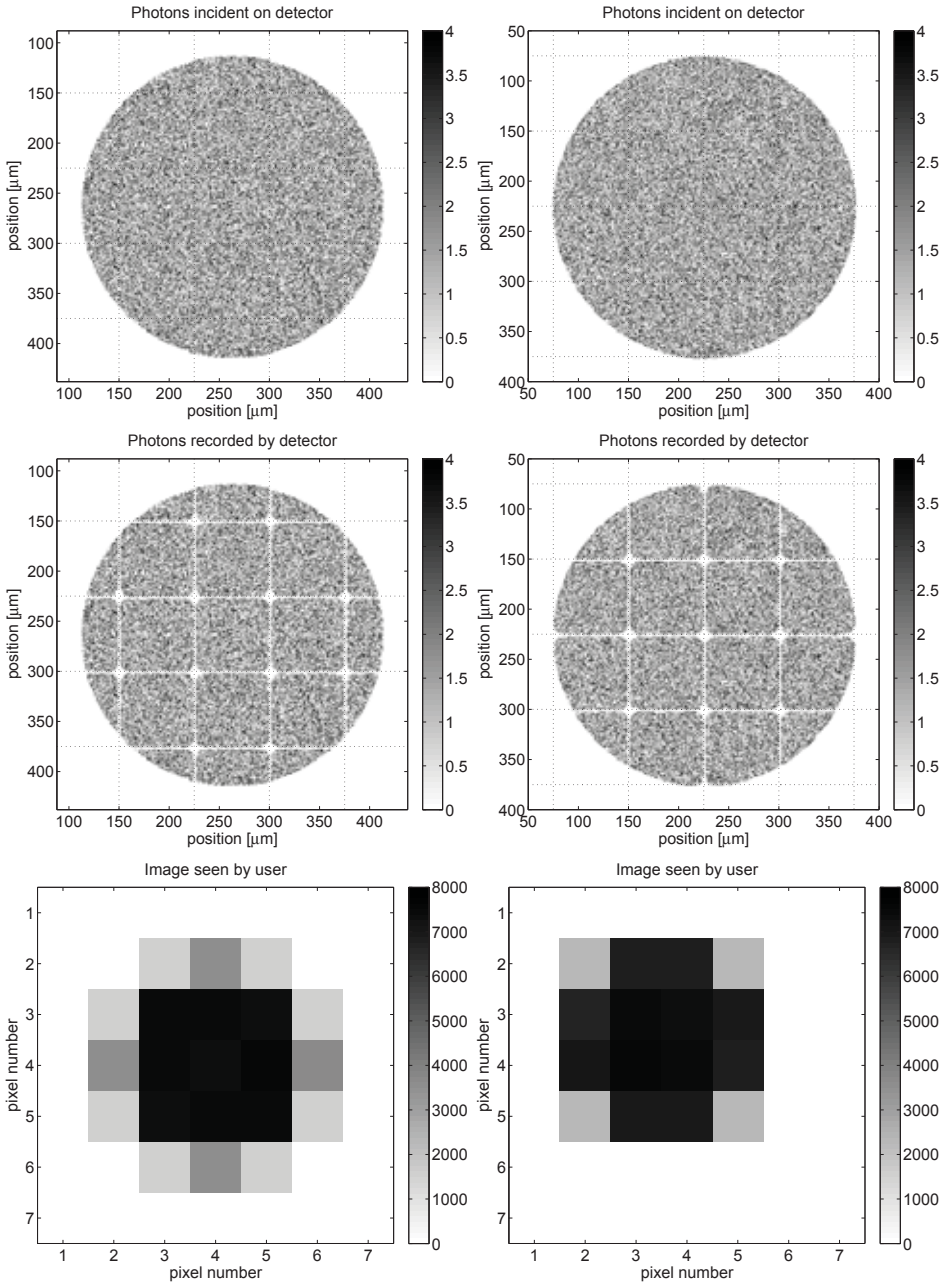

Figure 6.9: Simulated EIGER performance for a 300 μm spot with 100,000 photons. In each column, the top image shows the photons incident on the detector face, the middle image shows the photons recorded by the detector, and the bottom image shows the pixelated image as seen by the user. The left column shows a spot centered on a pixel and the right column shows a spot centered on a corner. Grayscales are in units of photons. In the top two images in each column, pixel boundaries are indicated by dotted lines.

For the CCD, the signal recorded by a pixel is determined by the integrated photo-generated charge and the read noise. Spots incident on the detector face were simulated as described above. The PSF was modeled as a 2D Gaussian and was convolved with the spot image. The resulting image was binned into pixels. The pixels were checked for saturation; if the charge collected by a pixel exceeded the pixel full well, the pixel's value was reset to the full well and the excess charge was shifted to the next pixel down (representing blooming, which occurs in the readout direction in a CCD). Finally, read noise was added to each pixel according to a Gaussian distribution. Examples are shown in Figures 6.10-6.11. The spot intensity was summed over a specified area, as in the pinhole experiment. For 25 μm spots, the recorded signal was summed over a radius of 1.5 pixels; for 150 μm spots, over a radius of 4 pixels; for 300 μm spots, over a radius of 7 pixels.

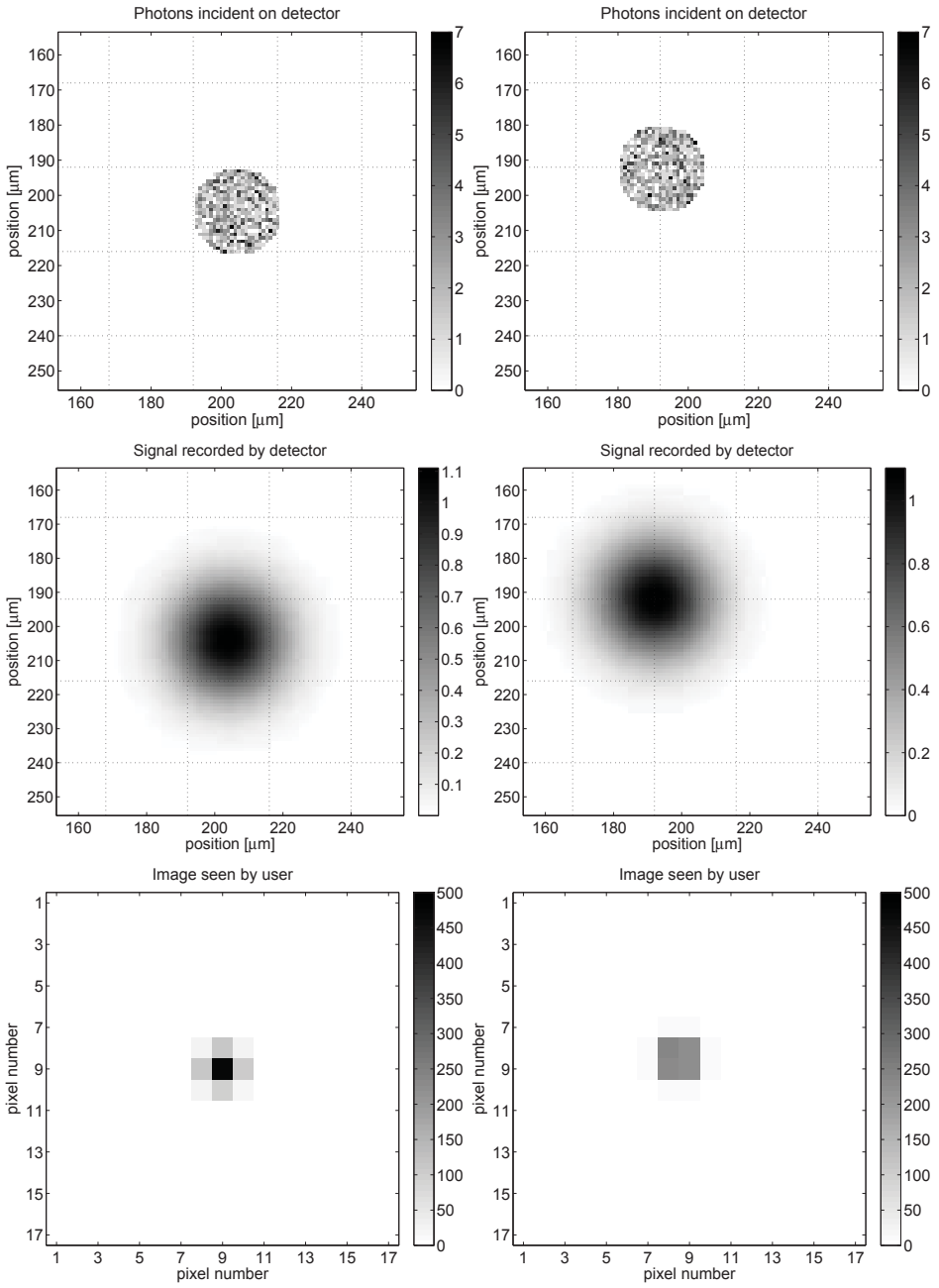

Figure 6.10: Simulated direct-detection CCD performance for a 25 μm spot with 1,000 photons. In each column, the top image shows the photons incident on the detector face, the middle image shows the photons recorded by the detector, and the bottom image shows the pixelated image as seen by the user. The left column shows a spot centered on a pixel and the right column shows a spot centered on a corner. Grayscales are in units of photons. In the top two images in each column, pixel boundaries are indicated by dotted lines.

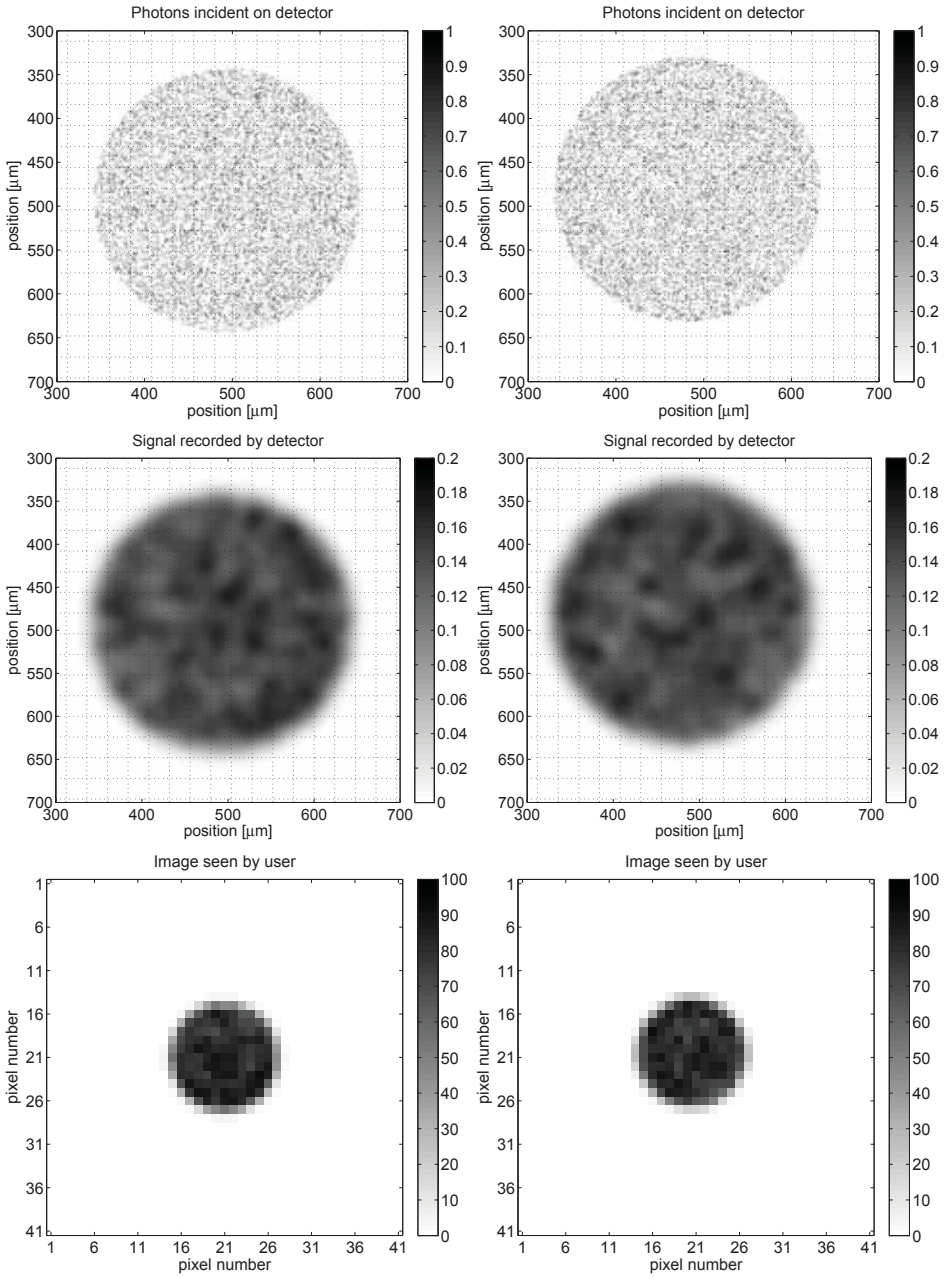

Figure 6.11: Simulated direct-detection CCD performance for a 300 μm spot with 10,000 photons. In each column, the top image shows the photons incident on the detector face, the middle image shows the photons recorded by the detector, and the bottom image shows the pixelated image as seen by the user. The left column shows a spot centered on a pixel and the right column shows a spot centered on a corner. Grayscales are in units of photons. In the top two images in each column, pixel boundaries are indicated by dotted lines.

Finally, the DQE curves were calculated for each detector using the simulated data, and are plotted in Figures 6.12 and 6.13. Note that the CCD saturates at 1000 photons per spot for the 25 μm spots, at 10^4 photons per spot for the 150 μm spots, and at 5×10^4 photons per spot for the 300 μm spots. For a given spot size, once saturation set in, the simulation was halted, since saturated data is not useable in an experimental setting.

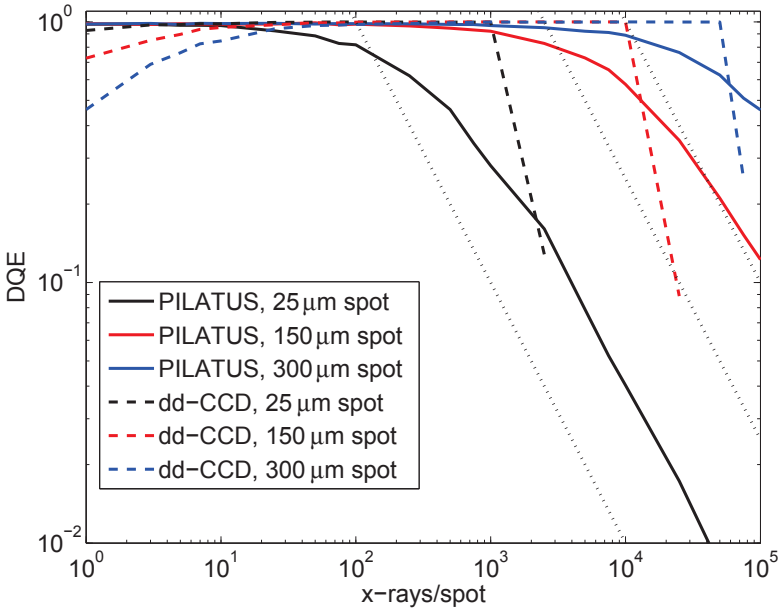

Figure 6.12: Simulated DQE for the PILATUS and the revised direct-detection CCD. The dotted lines are the DQE that would be obtained if the spots were measured to an accuracy of 10%, 2%, and 1%.

For the 300 μm and 150 μm spots, the photon-counting PADs are clearly superior at low intensity due to their suppression of read noise. The direct-detection CCD catches up to the photon-counting PAD performance around 100 photons per spot for the 300 μm spots and around 50 photons per spot for the 150 μm spots. In comparison, for 25 μm spots, at low intensity the CCD and PILATUS have very similar, near-unity DQEs.

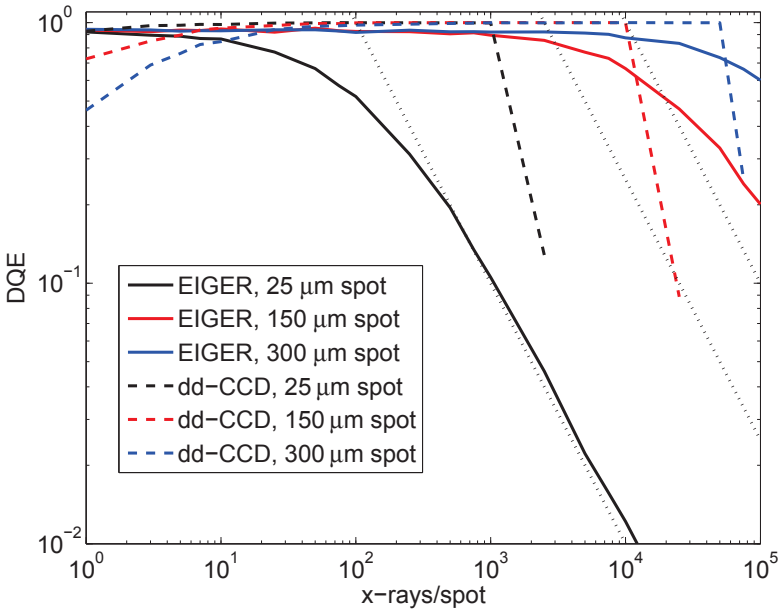

Figure 6.13: Simulated DQE for the EIGER and the revised direct-detection CCD. The dotted lines are the DQE that would be obtained if the spots were measured to an accuracy of 10%, 2%, and 1%.

For 25 μm spots, the DQE of the PILATUS begins to fall around 10 photons per spot, and for the EIGER the DQE begins to fall after 1 photon per spot. This is due to the substantial fraction of the spot that is lost due to the pixel dead areas. For 25 μm spots, the fraction of charge lost ranges from zero, when the spot is centered on a pixel, to 35% for spots falling directly on a pixel corner. As the spots become larger, two things happen. First, the fraction of charge lost decreases simply due to the relative area of the spot compared to the pixel dead regions. Second, the fraction of charge lost becomes less dependent on the location of the spot center of mass, since no matter where the spot is located it is likely to cover multiple pixel corners and edges. This improves the photon-counting PAD DQE for larger spots.

For the PILATUS, the 150 μm curve begins to turn downward around 300 photons per spot and the 300 μm curve begins to turn downward around 1000

photons per spot. For the EIGER, the 150 μm curve turns downward at around 1000 photons per spot, and the 300 μm curve turns downward at around 7,000 photons per spot. Recall from the pinhole data that the sDQE curves for the current prototype CCD begin to turn over at around 2000 photons per spot for 300 and 150 μm spots. Because the revised CCD is expected to have reduced detector systematics, this represents a lower bound on the expected turning point for the re-designed CCD. Therefore, for 150 μm spots, the re-designed direct-detection CCD would marginally outperform the PILATUS when the spot intensity exceeds about 300 photons, until saturation sets in at 10^4 photons per spot. The re-designed CCD could marginally outperform the EIGER over a slimmer range of spot intensities, starting around 1000 photons per spot. It is doubtful, however, if the marginally better performance at higher spot doses would justify the use of the CCD over the commercially available PILATUS or EIGER detectors. Accounting for detector systematics, the CCD would not have a significant edge over either of the photon-counting PADs for 300 μm spots.

6.3.4 On single-photon detection with a CCD

For the simulated CCD data, the spot center of mass was known. This is analagous to what was done in the pinhole experiment, where the pinhole locations were static and were determined using the average of many frames. Using known spot locations lets one assess how the spot statistics themselves are affected by detector systematics. However, it is not necessarily representative of a diffraction experiment, in which the location of spots is not known *a priori*. The simulated single-photon images in Figure 6.14 suggest that the read noise in the proposed re-designed CCD is on the edge of allowing accurate determination

of the location of single photon hits from individual frames.

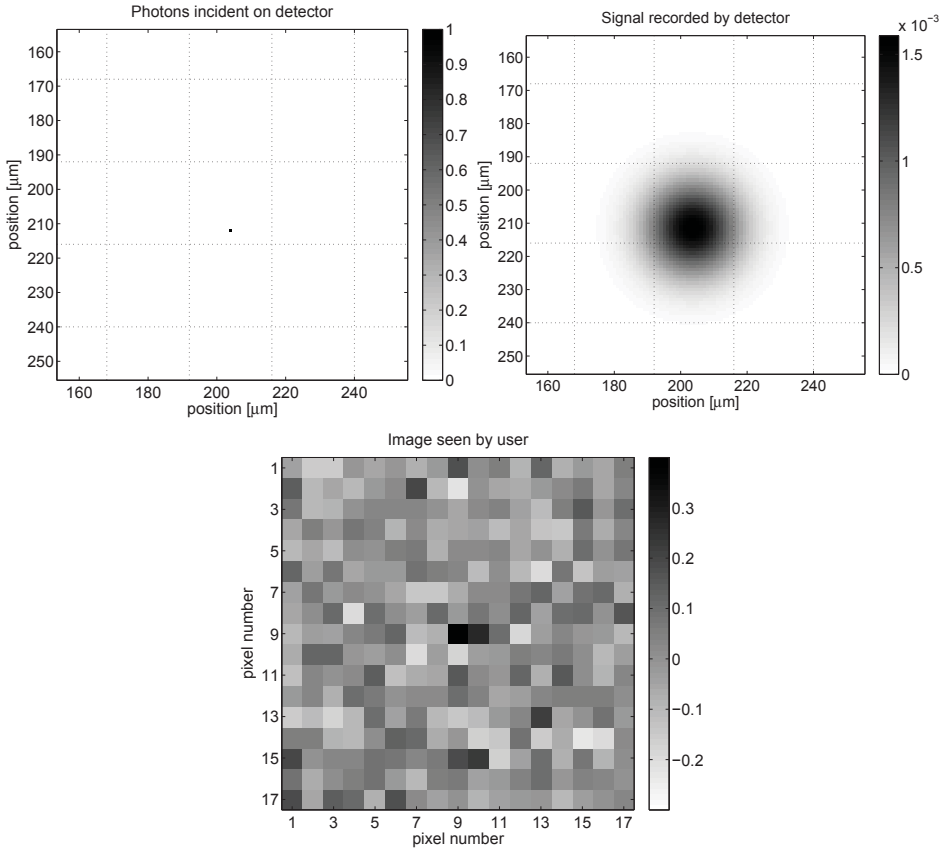

Figure 6.14: Simulated direct-detection CCD performance for a single photon hit. Grayscales are in units of photons. The location of the photon hit can barely be distinguished by eye in the image as seen by the end user.

To estimate the read noise required for reliable detection of a single-photon hit, with no prior knowledge of its location, the simulation was repeated for single-photon hits as the read noise was varied from 20 e- to 380 e-, the read noise in the current prototype. A photon hit was considered to be successfully detected if its location was determined from a single simulated frame to within 1.5 pixels of its true location. 5000 trials were run for each value of read noise. The probability of succesfully locating the single-photon hit was determined and is plotted in Figure 6.15. With the proposed read noise of 256 e-, single

photon hits are succesfully located about with about a 10% success rate. Read noise of 20 e- would lead to an almost 100% success rate, but is not practical if the pixel well depth is to be maintained at a few hundred 10 keV photons per pixel. The read noise would have to be reduced to between 50 and 100 e- to give a 50% probability of accurately detecting single photons in individual frames with no prior knowledge of their location. This is an ambitious goal if the pixel well depth is to be preserved at close to the present value, and would require further design studies.

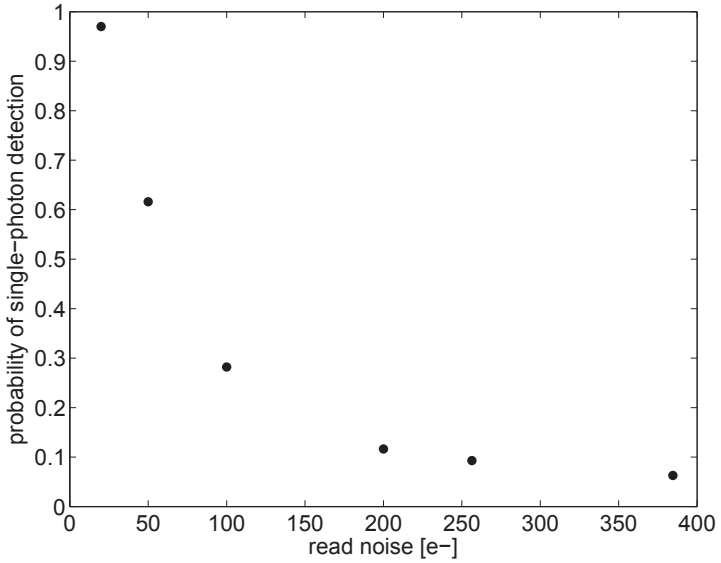

Figure 6.15: Probability of single-photon detection as a function of read noise in the proposed re-designed CCD.

CHAPTER 7

CONCLUSIONS

7.1 Summary

The STA3200, a direct-detection CCD with a 600 μm thick sensor, has been characterized. Electrical damage prevented the CCD from being fully depleted, resulting in a depletion layer extending through only about 2/3 of the sensor, with a significant undepleted layer on the x-ray entrance side. In spite of this defect, a PSF with FWHM $\leq$ 40μm was demonstrated for x-rays in the range of 8-17.5 keV. The read noise, while higher than desired, is equivalent to about one tenth of an x-ray at 13.5 keV. The prototype was successfully used to collect and analyze diffraction patterns from cryocooled thaumatin crystals using both a collimated 100 μm beam and a microfocused 20 μm beam, in most cases with slightly better merging statistics than a conventional phosphor-coupled CCD.

Measurements using pinhole masks and a home laboratory 17.5 keV x-ray source demonstrated improved performance of the prototype for very small spot sizes (down to 25 μm in diameter) compared to spot sizes on the order of 300 μm in diameter. Analysis of a modified form of the DQE indicates that detector systematics in the current prototype degrade the detector performance starting at about 200 photons per spot for 25 μm spots, and at about 2000 photons per spot for 150 and 300 μm spots. Above this level, 300 μm spots were recorded with greater than 1% accuracy.

The simulations in Chapter 6 showed that, compared to the PILATUS photon-counting PAD or its successor the EIGER, a re-designed version of the

STA3200 with moderately improved read noise would not offer a benefit in terms of SNR for detection of x-ray spots on the order of 300 μm in diameter. The CCD would gain an advantage in terms of SNR for spots on the order of 150 μm in diameter for intensities of about 10^3 – 10^4 photons per spot, depending on the pixel size of the photon-counting PAD. For 25 μm spots, the CCD would have a clear advantage after 10 photons per spot. However, even with a 1 μm diameter focused beam and a detector only 100 mm away from the sample, diffraction spots would have to leave the crystal with divergence less than 0.1 mrad in order to arrive at a detector face having spread to only 25 μm in diameter. Since the divergence of the diffracted spots includes contributions from crystal mosaicity as well as the incident beam, this is an unlikely scenario.

The CCD's superior performance for medium-to-small spots at high intensity is a result of the presence of dead areas in the photon-counting PAD pixels, which are a consequence of charge sharing. Because CCDs integrate charge rather than processing individual photons, charge sharing does not lead to dead areas in the sensor. The latest version of the Medipix photon-counting PAD includes circuits that compensate for charge sharing and eliminate the pixel dead areas. If this becomes a standard design in photon-counting PADs, their performance will be greatly enhanced.

A re-designed direct-detection CCD would still offer some benefits for diffraction experiments with large spots. Due to the small pixel sizes available in the CCD fabrication process, the spatial resolution of the CCD is higher than that of currently available PADs. For example, if spatial detail within the diffraction spot is of interest, as in diffraction topography and some XFEL experiments described in Chapter 5, the CCD would resolve finer detail than either

of the photon-counting PADs considered in Chapter 6, due to the difference in pixel size.

In Chapter 3, photon-integrating PADs were used as examples for the development of detector characterization methods including gain calibration through the discrete photon spectrum method and pixel area calibration through pixel boundary scans. Photon-integrating PADs have not explicitly been addressed in this work as candidates for use in protein microcrystallography. In terms of accurately detecting diffraction spots, photon-integrating PADs combine aspects of direct-detection CCDs and photon-counting PADs. They exhibit x-ray-equivalent read noise similar to that demonstrated by the current STA3200 prototype, but have the benefit of larger pixel well depth, typically around 1000 x-rays. The MMPAD is a unique case, where the well depth is extended to 3×10^7 8 keV x-rays per pixel through use of a charge removal circuit and an in-pixel digital counter. Compared to direct-detection CCDs, this significantly extends the accessible range of x-ray spot intensities.

Photon-integrating PADs are subject to the same type of detector systematics as CCDs: amplifier gain variation and pixel-to-pixel sensitivity and area variation. Like CCDs, they do not exhibit dead areas due to charge sharing. However, PADs of either variety (integrating or counting) require more detailed calibration than CCDs simply due to the larger number of readout amplifiers. Because the quality of the detector calibration limits the detector performance at high intensities, simplified calibration can be seen as an advantage for CCDs relative to PADs, especially in experiments where a very large well depth or high frame rate are not necessary.

APPENDIX A

CHARGE CLOUD SPREAD CALCULATIONS

The full calculations for the charge cloud spread for different sensors and experimental conditions are presented.

A.1 STA3200 model

To determine the charge cloud width that can be expected in a fully-depleted version of the STA3200 CCD, we model the charge collection in a p-type diode that is 600 μm thick, with 10 kΩ-cm resistivity, cooled to 205 K. The diode is shown schematically in Figure A.1.

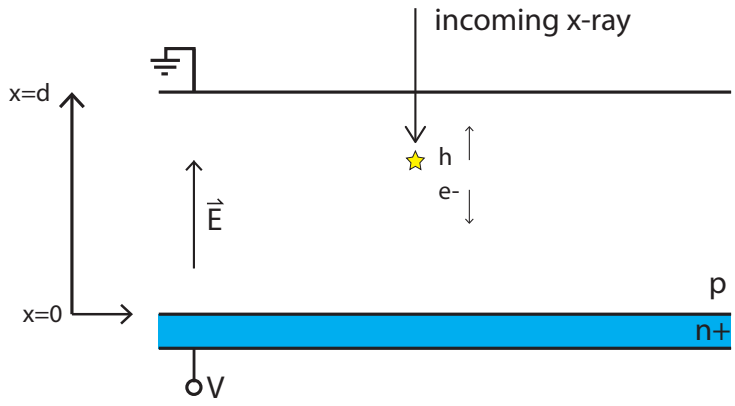

Figure A.1: Charge conversion in the model STA3200.

An external voltage V is applied to the n+ side to overdeplete the diode. This imposes a transverse electric field **E** which points from the n+ channel towards the x-ray entrance side. When the diode is fully depleted, the maximum field is at the junction ($x = 0$):

$$E(x = 0) = E_{max} = \frac{2V_{dep}}{d}. \tag{A.1}$$

If the diode is overdepleted, $V = V_{dep} + V_{ob}$ adds a transverse overbias field with magnitude $E_{ob} = \frac{V_{ob}}{d}$. Thus

$$|E(x)| = \begin{cases} \frac{V_{ob}}{d} & \text{at } x = d \\ \frac{2V_{dep}}{d} + \frac{V_{ob}}{d} & \text{at } x = 0 \end{cases} \tag{A.2}$$

Assuming a linear change between the two endpoints we have

$$|E(x)| = \frac{2V_{dep}}{d}\frac{d-x}{d} + \frac{V_{ob}}{d} \tag{A.3}$$

Now consider the motion of electrons as they move from the photon conversion point to $x = 0$:

$$\begin{aligned} \mathbf{v} = -\mu_n \mathbf{E} \implies \frac{dx}{dt} &= -\mu_n E \\ \implies \frac{dx}{dt} &= -\mu_n \left(\frac{2V_{dep}}{d}\frac{d-x}{d} + \frac{V_{ob}}{d} \right) \\ &= -\mu_n \left(\frac{2V_{dep}d}{d^2} - \frac{2V_{dep}x}{d^2} + \frac{V - V_{dep}}{d} \right) \\ &= -\mu_n \left(\frac{V + V_{dep}}{d} - \frac{2V_{dep}x}{d^2} \right) \\ &= \mu_n \left(\frac{2V_{dep}}{d^2} \right) x - \mu_n \left(\frac{V + V_{dep}}{d} \right). \end{aligned} \tag{A.4}$$

This is an equation of the form

$$\frac{dx}{dt} = abx - ac \tag{A.5}$$

with $a = \mu_n$, $b = \frac{2V_{dep}}{d^2}$ and $c = \frac{V+V_{dep}}{d}$. The solution is given by

$$\begin{aligned}
\int \frac{dx}{abx - ac} &= \int dt \\
\implies \frac{\ln(abx - ac)}{ab} &= t + K_1 \\
\implies \ln(abx - ac) &= abt + \underbrace{abK_1}_{K_2} \\
\implies abx - ac &= e^{abt} \underbrace{e^{K_2}}_{K_3} \\
\implies abx &= K_3 e^{abt} + ac \\
\implies x &= \frac{K_3 e^{abt} + ac}{ab} \\
\implies x &= K_4 e^{abt} + \frac{c}{b} \\
\implies x(t) &= K_4 \exp\left(\mu_n \frac{2V_{dep}}{d^2} t\right) + \frac{d(V + V_{dep})}{2V_{dep}}
\end{aligned} \tag{A.6}$$

where the K's are constants. Now $x(t = 0) = d$ and so

$$\begin{aligned}
d &= K_4 + \left(V + V_{dep}\right) \frac{d}{2V_{dep}} \\
\implies K_4 &= d - \frac{d\left(V + V_{dep}\right)}{2V_{dep}} \\
&= d\left(\frac{2V_{dep} - V - V_{dep}}{2V_{dep}}\right) \\
&= d\left(\frac{V_{dep} - V}{2V_{dep}}\right)
\end{aligned} \tag{A.7}$$

Thus the electron position can be written as

$$\boxed{x(t) = d\left(\frac{V_{dep} - V}{2V_{dep}}\right) e^{\frac{2\mu_n V_{dep} t}{d^2}} + d\frac{V + V_{dep}}{2V_{dep}}} \tag{A.8}$$

These equations provide a starting point for calculating the motion of charges in the diode, but note that velocity saturation must be considered; once velocity saturation is reached, the center of the charge cloud moves at a constant

velocity v_{sat} rather than according to the equation of motion above. The saturation velocity itself scales with temperature, as $T^{-0.87}$ for electrons and $T^{-0.58}$ for holes [78]. To illustrate the effect of temperature, the electron velocity as a function of distance from the diode top surface is plotted, along with values of v_{sat}, for room temperature and $T = 205$ K, for an overbias of 10 V, in Figure A.2.

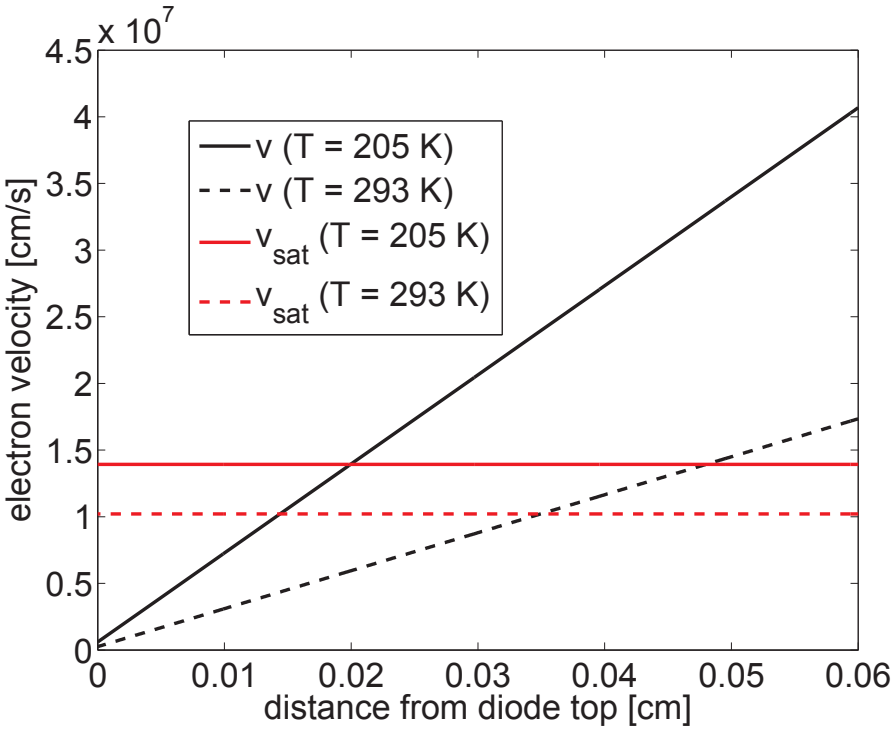

Figure A.2: Electron velocity in 600 μm, 10 kΩ-cm p-type Si with 10 V overbias.

Once the time required for the photo-generated charge to traverse the diode is calculated, Equation 2.5, which describes the lateral diffusion of the charge cloud, can be used to compute the width of the charge cloud. Accounting for velocity saturation and the temperature-dependence of the electron mobility, the charge cloud collection time and width are plotted as a function of overbias in Figure A.3.

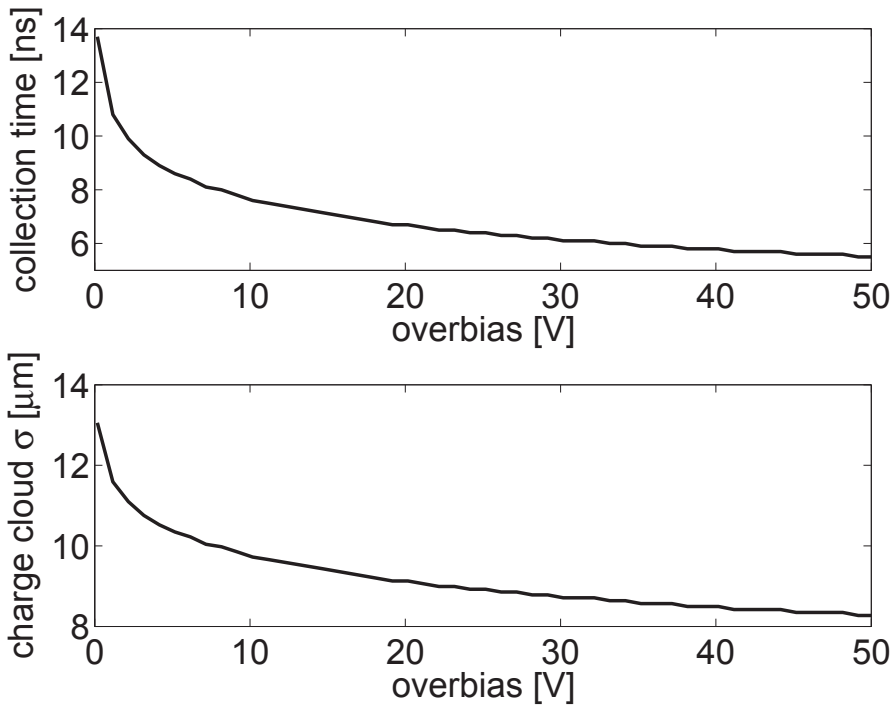

Figure A.3: Charge cloud collection time and width in 600 μm, 10 kΩ-cm p-type Si.

A.2 MMPAD model

Similar calculations can be performed for the MMPAD diode. In this case the diode is n-type with a thickness of 500 μm, held at 253 K. The external voltage V is applied to the x-ray entrance side, creating a transverse electric field pointing from the entrance side to the pixel p+ implant. In contrast to the STA3200 case, holes are collected at the junction. The equation of motion is

$$\mathbf{v} = \mu_p \mathbf{E} \implies \frac{dx}{dt} = -\mu_p E$$

where the minus sign accounts for the direction of $\mathbf{E}$. The magnitude of the electric field has the same form as in the STA3200 example (Equation A.3). The hole position is therefore described by Equation A.8, with the substitution of μ_p for μ_n.

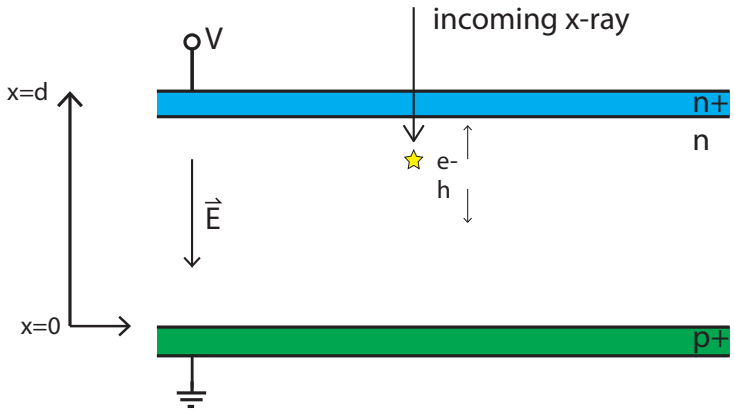

Figure A.4: Charge conversion in the model MMPAD.

Assuming a resistivity of 10 kΩ-cm, the depletion voltage is 80 V. In this scenario, the diode can be more strongly overdepleted with a reasonable applied voltage. In this scenario, even with an overbias of 100 V, the holes do not reach saturation velocity by the time they reach the junction, as shown in Figure A.5. The charge cloud collection time and width are plotted as a function of overbias in Figure A.6.

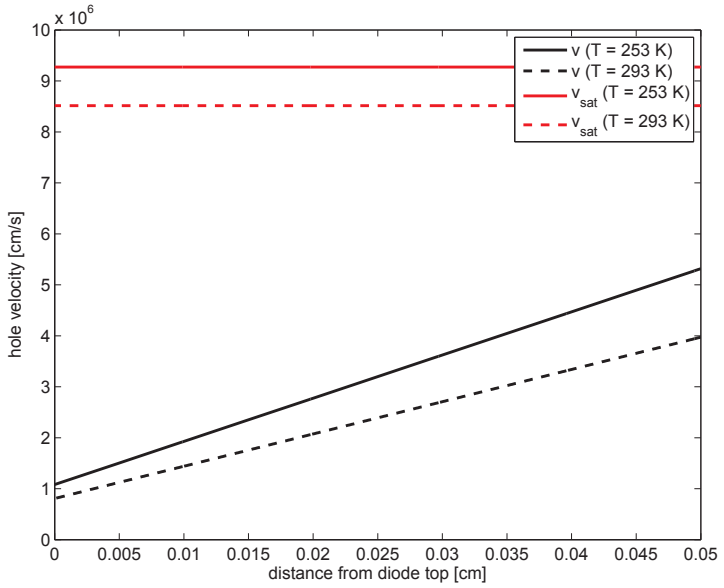

Figure A.5: Hole velocity in 500 μm, 10 kΩ-cm n-type Si with 100 V overbias.

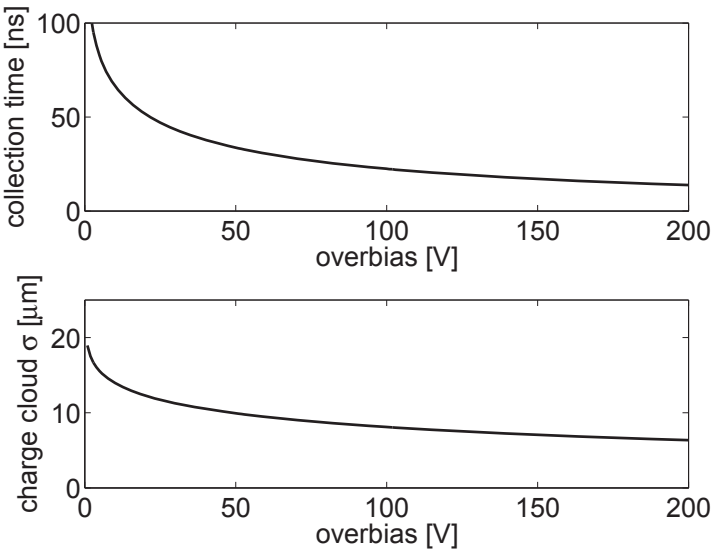

Figure A.6: Charge cloud collection time and width in 500 μm, 10 kΩ-cm n-type Si.

APPENDIX B

SDQE ERROR PROPAGATION

There are three main sources of uncertainty that propagate into the calculated sDQE: the uncertainty in the pinhole size map, the uncertainty in the frame-to-frame source fluctuation, and the uncertainty in the detector gain.

Denote the signal recorded through pinhole i in frame j as S_{ij} (units: ADU). The sDQE is calculated as:

$$\text{sDQE} = \frac{(< S_{norm} > / \sigma_{S_{norm}})^2}{S_{in,stopped}} \tag{B.1}$$

where $< S_{norm} >$ is the average of the pinhole signals S_{ij} after normalization for pinhole size and frame-to-frame source fluctuation (units: ADU); $\sigma_{S_{norm}}$ is the standard deviation of that population (units: ADU); and $S_{in,stopped}$ is the computed stopped signal (units: number of photons). (Through this calculation, standard deviations computed via the definition $\sigma_x = \sqrt{\frac{1}{N}\sum_{i=1}^{N}(x_i - < x >)^2}$ will be denoted by σ's, and uncertainties will be denoted by δ's.) Therefore the uncertainty on the sDQE is:

$$\delta_{sDQE} = \sqrt{\left(\frac{\partial \text{sDQE}}{\partial < S_{norm} >}\right)^2 \delta^2_{<S_{norm}>} + \left(\frac{\partial \text{sDQE}}{\partial \sigma_{S_{norm}}}\right)^2 \delta^2_{\sigma_{S_{norm}}} + \left(\frac{\partial \text{sDQE}}{\partial S_{in,stopped}}\right)^2 \delta^2_{S_{in,stopped}}} \tag{B.2}$$

The partial derivatives are as follows:

$$\frac{\partial \text{sDQE}}{\partial < S_{norm} >} = \frac{2 < S_{norm} >}{\sigma^2_{S_{norm}} S_{in,stopped}} \tag{B.3}$$

$$\frac{\partial \text{sDQE}}{\partial \sigma_{S_{norm}}} = \frac{-2 < S_{norm} >^2}{\sigma^3_{S_{norm}} S_{in,stopped}} \tag{B.4}$$

$$\frac{\partial \text{sDQE}}{\partial S_{in,stopped}} = \frac{- < S_{norm} >^2}{\sigma^2_{S_{norm}} S^2_{in,stopped}} \tag{B.5}$$

I will use the convention that $< S_k >$ denotes the averaging of the S_{ij}'s over the index not inside brackets; that is, $< S_i >$ denotes the average signal in pinhole i

across all frames j. $< S >$ denotes an average over both indices; i.e., the average signal over all pinholes in all frames.

B.1 Uncertainty in the stopped signal

The incoming, stopped signal $S_{in,stopped}$ is computed by dividing the average signal over all pinholes in all frames, corrected for pinhole area variations, by the detector gain g:

$$S_{in,stopped} = \frac{< S_{AC} >}{g} \tag{B.6}$$

where the subscript AC denotes an area correction. The average area-corrected signal in pinhole i over all frames j is given by:

$$S_{i,AC} = \frac{< S_i >}{\alpha_i} \tag{B.7}$$

where the area factor α_i is given by

$$\alpha_i = \frac{< S_i' >}{< S' >}. \tag{B.8}$$

S' denotes measurements in the spot area mapping dataset. This is a separate measurement from that used for the sDQE calculation. The uncertainty on α_i is the standard deviation on the measurement of pinhole i's signal across all frames in the spot-mapping dataset. Therefore $< S_{AC} >$ can be written as

$$< S_{AC} >= \frac{1}{N_{pinholes}} \sum_i \frac{< S_i >}{\alpha_i} \tag{B.9}$$

where $N_{pinholes}$ is the number of pinholes in the mask. The uncertainty on S_{AC} is given by

$$\delta_{<S_{AC}>} = \sqrt{\sum_i \left[\left(\frac{\partial < S_{AC} >}{\partial < S_i >} \right)^2 \delta^2_{<S_i>} \right] + \sum_i \left[\left(\frac{\partial < S_{AC} >}{\partial \alpha_i} \right)^2 \delta^2_{\alpha_i} \right]} \tag{B.10}$$

The partial derivatives are given by

$$\frac{\partial < S_{AC} >}{\partial < S_i >} = \frac{1}{N_{pinhole}} \frac{1}{\alpha_i} \tag{B.11}$$

$$\frac{\partial < S_{AC} >}{\partial \alpha_i} = \frac{- < S_i >}{N_{pinhole} \alpha_i^2} \tag{B.12}$$

Therefore $\delta_{<S_{AC}>}$ can be written as:

$$\delta_{<S_{AC}>} = \frac{1}{N_{pinhole}} \sqrt{\sum_i \left[\frac{\delta^2_{<S_i>}}{\alpha_i^2} + \frac{< S_i >^2}{\alpha_i^4} \delta^2_{\alpha_i} \right]} \tag{B.13}$$

The uncertainty on $S_{in,stopped}$ is then

$$\delta_{S_{in,stopped}} = \sqrt{\left(\frac{\partial S_{in,stopped}}{\partial g} \right)^2 \delta_g^2 + \left(\frac{\partial S_{in,stopped}}{\partial < S_{AC} >} \right)^2 \delta^2_{<S_{AC}>}} \tag{B.14}$$

$$= \sqrt{\frac{< S_{AC} >^2}{g^4} \delta_g^2 + \frac{1}{g^2} \delta^2_{<S_{AC}>}} \tag{B.15}$$

B.2 Uncertainty in the measured signal $< S_{norm} >$

The pinhole signals are normalized by the pinhole size and the frame-by-frame global intensity fluctuations, in order to eliminate these as sources of uncertainty external to the detector. The normalized pinhole signals are given by

$$S_{ij,norm} = \frac{S_{ij}}{\eta_j \alpha_i} \tag{B.16}$$

where η_j is given by

$$\eta_j = < S_j >. \tag{B.17}$$

η_j and α_i have uncertainties that must be propagated through to δ_{sDQE}. The uncertainty on η_j is the standard deviation of the pinhole intensities in frame j: $\delta_{\eta_j} = \sigma_{S_j}$.

The uncertainty on a single normalized pinhole signal, $S_{ij,norm}$, is

$$\delta_{S_{ij,norm}} = \sqrt{\left(\frac{\partial S_{ij,norm}}{\partial \eta_j}\right)^2 \delta_{\eta_j}^2 + \left(\frac{\partial S_{ij,norm}}{\partial \alpha_i}\right)^2 \delta_{\alpha_i}^2} \tag{B.18}$$

The partial derivatives are:

$$\frac{\partial S_{ij,norm}}{\partial \eta_j} = \frac{-S_{ij}}{\eta_j^2 \alpha_i} \tag{B.19}$$

$$\frac{\partial S_{ij,norm}}{\partial \alpha_i} = \frac{-S_{ij}}{\eta_j \alpha_i^2} \tag{B.20}$$

Thus

$$\delta_{S_{ij,norm}} = \sqrt{\left(\frac{S_{ij}}{\eta_j^2 \alpha_i}\right)^2 \delta_{\eta_j}^2 + \left(\frac{S_{ij}}{\eta_j \alpha_i^2}\right)^2 \delta_{\alpha_i}^2} \tag{B.21}$$

and the uncertainty on the average normalized pinhole signal, $< S_{norm} >$ is given by adding the individual uncertainties in quadrature:

$$\delta_{<S_{norm}>} = \frac{1}{N_{pop}} \sqrt{\sum_{ij} \delta_{S_{ij,norm}}^2} \tag{B.22}$$

where N_{pop} is the number of pinhole measurements in the population (across all pinholes and all frames).

B.3 Uncertainty in the measured noise $\sigma_{S_{norm}}$

$\sigma_{S_{norm}}$ is a standard deviation and is therefore given by

$$\sigma_{S_{norm}} = \sqrt{\frac{1}{N_{pop}} \sum_{ij} \left(S_{ij,norm} - < S_{norm} >\right)^2} \tag{B.23}$$

The uncertainty on $\sigma_{S_{norm}}$ is

$$\delta_{\sigma_{S_{norm}}} = \sqrt{\sum_{ij} \left[\left(\frac{\partial \sigma_{S_{norm}}}{\partial S_{ij,norm}}\right)^2 \delta_{S_{ij,norm}}^2\right] + \left(\frac{\partial \sigma_{S_{norm}}}{\partial < S_{norm} >}\right)^2 \delta_{<S_{norm}>}^2} \tag{B.24}$$

The partial derivatives are:

$$\frac{\partial \sigma_{S_{norm}}}{\partial S_{ij,norm}} = \frac{1}{\sqrt{N_{pop}}} \frac{S_{ij,norm} - < S_{norm} >}{\sqrt{\sum_{ij} \left(S_{ij,norm} - < S_{norm} > \right)^2}} \tag{B.25}$$

$$\frac{\partial \sigma_{S_{norm}}}{\partial < S_{norm} >} = \frac{-1}{\sqrt{N_{pop}}} \frac{\sum_{ij} \left(S_{ij,norm} - < S_{norm} > \right)}{\sqrt{\sum_{ij} \left(S_{ij,norm} - < S_{norm} > \right)^2}} \tag{B.26}$$

Note that

$$\frac{1}{\sqrt{\sum_{ij} \left(S_{ij,norm} - < S_{norm} \right)^2}} = \frac{\sqrt{N_{pop}}}{\sqrt{\sum_{ij} \left(S_{ij,norm} - < S_{norm} > \right)^2}} \frac{1}{\sqrt{N_{pop}}} \tag{B.27}$$

$$= \frac{1}{\sigma_{S_{norm}}} \frac{1}{\sqrt{N_{pop}}} \tag{B.28}$$

and therefore the partial derivatives can be written as:

$$\frac{\partial \sigma_{S_{norm}}}{\partial S_{ij,norm}} = \frac{1}{N_{pop}} \frac{S_{ij,norm} - < S_{norm} >}{\sigma_{S_{norm}}} \tag{B.29}$$

$$\frac{\partial \sigma_{S_{norm}}}{\partial < S_{norm} >} = \frac{-1}{N_{pop}} \frac{\sum_{ij} \left(S_{ij,norm} - < S_{norm} > \right)}{\sigma_{S_{norm}}} \tag{B.30}$$

$\delta_{\sigma_{S_{norm}}}$ can now be written as

$$\delta \sigma_{S_{norm}} = \left[\sum_{ij} \left[\left(\frac{S_{ij,norm} - < S_{norm} >}{N_{pop}} \frac{1}{\sigma_{S_{norm}}} \right)^2 \delta^2_{S_{ij,norm}} \right] + \left(\frac{1}{N_{pop}} \frac{\sum_{ij} \left(S_{ij,norm} - < S_{norm} > \right)}{\sigma_{S_{norm}}} \right)^2 \delta^2_{<S_{norm}>} \right]^{1/2} \tag{B.31}$$

BIBLIOGRAPHY

[1] O. J. P., B. Al-Lazikani, and A. L. Hopkins, "How many drug targets are there?" *Nature Reviews*, vol. 5, pp. 993–996, 2006.

[2] J. L. Smith, R. F. Fischetti, and M. Yamamoto, "Micro-crystallography comes of age," *Current Opinion in Structural Biology*, vol. 22, pp. 602–612, 2012.

[3] J. Drenth, *Principles of Protein X-Ray Crystallography*. New York: Springer, 1999.

[4] A. Perrakis, F. Cipriani, J.-C. Castagna, L. Claustre, M. Burghammer, C. Riekel, and S. Cusack, "Protein microcrystals and the design of a microdiffractometer: current experience and plans at EMBL and ESRF/ID13," *Acta Crystallographical Section D*, vol. 55, no. 10, pp. 1765–1770, 1999.

[5] C. U. Kim, R. Kapfer, and S. M. Gruner, "High-pressure cooling of protein crystals without cryoprotectants," *Acta Crystallographical Section D*, vol. 61, pp. 881 – 890, 2005.

[6] G. Hülsen, C. Broennimann, E. F. Eikenberry, and A. Wagner, "Protein crystallography with a novel large-area pixel detector," *Journal of Applied Crystallography*, vol. 39, pp. 550 – 557, 2006.

[7] E. Chiu, F. Coulibaly, and P. Metcalf, "Insect virus polyhedra, infectious protein crystals that contain virus particles," *Current Opinion in Structural Biology*, vol. 22, pp. 234–240, 2012.

[8] R. Nelson, M. R. Sawaya, M. Balbirnie, A. Ø. Madsen, C. Riekel, R. Grothe, and D. Eisenberg, "Structure of the cross-β spine of amyloid-like fibrils," *Nature*, vol. 435, pp. 773–778, 2005.

[9] J. Li, P. C. Edwards, M. Burghammer, C. Villa, and G. F. X. Schertler, "Structure of bovine rhodopsin in a trigonal crystal form," *Journal of Molecular Biology*, vol. 343, pp. 1409–1438, 2004.

[10] S. G. F. Rasmussen, H.-J. Choi, D. M. Rosenbaum, T. S. Kobilka, F. S. Thian, P. C. Edwards, M. Burghammer, V. R. P. Ratnala, R. Sanishvili, R. F. Rischetti, G. F. X. Schertler, W. I. Weis, and B. K. Kobilka, "Crystal structure of the human β_2 adrenergic G-protein-coupled receptor," *Nature*, vol. 450, pp. 383–388, 2007.

[11] J. Hausmann, E. Christodoulou, M. Kasiem, V. De Marco, L. A. van Meeteren, W. H. Moolenaar, D. Axford, R. L. Owen, G. Evans, and A. Perrakis, "Mammalian cell expression, purification, crystallization and microcrystal data collection of autotaxin/ENPP2, a secreted mammalian glycoprotein," *Acta Crystallographica Section F*, vol. 66, pp. 1130–1135, 2010.

[12] J. M. Holton and K. A. Frankel, "The minimum crystal size needed for a complete diffraction data set," *Acta Crystallographica Section D*, vol. 66, pp. 393–408, 2010.

[13] R. E. Thorne, Z. Stum, J. Kmetko, K. ONeill, and R. Gillilan, "Microfabricated mounts for high-throughput macromolecular cryocrystallography," *Journal of Applied Crystallography*, vol. 36, pp. 1455–1460, 2003.

[14] J. L. Wierman, J. S. Alden, C. U. Kim, P. L. McEuen, and S. M. Gruner, "Graphene as a protein crystal mounting material to reduce background scatter," *Journal of Applied Crystallography*, vol. 46, pp. 1501–1507, 2013.

[15] S. W. Cornaby, "A handbook of x-ray single-bounce monocapillary optics, including optical design and synchrotron applications," Ph.D. dissertation, Cornell University, USA, 2008.

[16] J. M. Holton, "A beginner's guide to radiation damage," *Journal of Synchrotron Radiation*, vol. 16, pp. 133–142, 2010.

[17] M. R. Howells, T. Beetz, H. N. Chapman, C. Cui, J. M. Holton, C. J. Jacobsen, J. Kirz, E. Lima, S. Marchesini, H. Miao, D. Sayre, D. A. Shapiro, J. C. H. Spence, and D. Starodub, "An assessment of the resolution limitation due to radiation-damage in x-ray diffraction microscopy," *Journal of Electron Spectroscopy and Related Phenomena*, vol. 170, pp. 4–12, 2005.

[18] R. J. Southworth-Davies, M. A. Medina, I. Carmichael, and E. F. Garman, "Observation of decreased radiation damage at higher dose rates in room temperature protein crystallography," *Structure*, vol. 15, pp. 1531–1541, 2007.

[19] Q. Liu, Z. Zhang, and W. A. Hendrickson, "Multi-crystal anomalous diffraction for low-resolution macromolecular phasing," *Acta Crystallographica Section D*, vol. 67, pp. 45–49, 2011.

[20] H. T. Philipp, K. Ayyer, M. W. Tate, V. Elser, and S. M. Gruner, "Solving structure with sparse randomly-oriented x-ray data," *Optics Express*, vol. 20, pp. 13 129–13 137, 2012.

[21] H. T. Philipp, "Light sources now (storage rings)," March 2009, cornell University Physics 7683.

[22] F. Schotte, M. Lim, T. A. Jackson, A. V. Smirnov, J. Soman, J. S. Olson, G. N. Phillips, M. Wulff, and P. A. Anfinrud, "Watching a protein as it functions with 150-ps time-resolved x-ray crystallography," *Science*, vol. 300, pp. 1944–1947, 2003.

[23] S. M. Gruner, "Synchrotron radiation," January 2009, Cornell University Physics 7683.

[24] F. Capotondi, E. Pedersoli, N. Mahne, R. H. Menk, G. Passos, L. Raimondi, C. Sventina, G. Sandrin, M. Zangrando, M. Kiskinova, S. Bajt, M. Barthelmess, H. Fleckenstein, H. N. Chapman, J. Schulz, J. Bach, R. Fromter, S. Schleitzer, L. Muller, C. Gutt, and G. Grubel, "Coherent imaging using seeded free-electron laser pulses with variable polarization: first results and research opportunities," *Review of Scientific Instruments*, vol. 84, 2013.

[25] G. H. Hoffstaetter, S. M. Gruner, and M. Tigner, "Cornell Energy Recovery Linac science case and project definition design report," 2013.

[26] D. H. Bilderback, G. Hoffstaetter, and S. M. Gruner, "R&D toward an Energy Recovery Linac at synchrotron light source," *Synchrotron Radiation News*, vol. 23, pp. 32–41, 2010.

[27] L. J. Koerner, "X-ray analog pixel array detector for single synchrotron bunch time-resolved imaging," Ph.D. dissertation, Cornell University, USA, 2010.

[28] L. Struder and et al., "Large-format, high-speed, X-ray pnCCDs combined with electron and ion imaging spectrometers in a multipurpose chamber for experiments at 4th generation light sources," *Nuclear Instruments and Methods in Physics Research, Section A*, vol. 614, pp. 483–496, 2010.

[29] D. Doering, N. Andresen, D. Contarato, P. Denes, J. Joseph, P. McVittie, J.-P. Walder, and J. Weizeorick, "A 1MPixel fast CCD sensor for x-ray imaging," *IEEE Nuclear Science Symposium and Medical Imaging Conference Record*, pp. 527–529, 2012.

[30] D. Shapiro, S. Roy, R. Celestre, W. Chao, D. Doering, M. Howells, S. Kevan, D. Kilcoyne, J. Kirz, S. Marchesini, K. A. Seu, A. Schirotzek, J. Spence,

T. Tyliszczak, T. Warwick, D. Voronov, and H. A. Padmore, "Development of coherent scattering and diffractive imaging and the COSMIC facility at the Advanced Light Source," *Journal of Physics: Conference Series*, vol. 425, pp. 192 011–1–192 011–2, 2013.

[31] M. W. Tate, D. Chamberlain, K. S. Green, H. T. Philipp, P. Purohit, C. Strohman, and S. M. Gruner, "A medium-format, mixed-mode pixel array detector for kilohertz x-ray imaging," *Journal of Physics: Conference Series*, vol. 425, no. 062004, 2013.

[32] H. T. Philipp, M. Hromalik, M. W. Tate, L. J. Koerner, and S. M. Gruner, "Pixel array detector for X-ray free electron laser experiments," *Nuclear Instruments and Methods in Physics Research, Section A.*, vol. 649, pp. 67–69, 2011.

[33] A. C. Thompson, J. C. Nix, T. G. Achterkirchen, and E. M. Westbrook, "Large format CMOS-based detectors for diffraction studies," *Journal of Physics: Conference Series*, vol. 425, no. 012018, 2013.

[34] W. Vernon, M. Allin, R. Hamlin, T. Hontz, D. Nguyen, F. Augustine, S. M. Gruner, N. H. Xuong, D. R. Schuette, M. W. Tate, and L. J. Koerner, "First results from the 128x128 pixel mixed-mode Si x-ray detector chip," *SPIE Optics and Photonics*, vol. 6706, 2007.

[35] G. Lutz, *Semiconductor Radiation Detectors*. New York: Springer, 1999.

[36] C. Jacobini, C. Canali, G. Ottaviani, and A. Alberigi Quaranta, "A review of some charge transport properties of silicon," *Solid State Electronics*, vol. 20, pp. 77–89, 1977.

[37] S. Parker, A. Kok, C. Kenney, P. Jarron, J. Hasi, M. Despeisse, C. Da Via, and G. Anelli, "Increased speed: 3D silicon sensors; fast current amplifiers," *IEEE Transactions on Nuclear Science*, vol. 58, no. 2, pp. 404–417, 2011.

[38] P. Dreier, "High resistivity silicon for detector applications," *Nuclear Instruments and Methods in Physics Research, Section A*, vol. 288, pp. 272 – 277, 1990.

[39] J. R. Janesick, *Scientific Charge-Coupled Devices*. Bellingham: SPIE Press, 2001.

[40] G. M. Anelli, "Conception et caracterisation de circuits integres resis- tants

aux radiations pour les detecteurs de particules du LHC en technologies CMOS submicroniques profondes," Ph.D. dissertation, Institut National Polytechnique de Grenoble, 2000.

[41] B. Razavi, *Design of Analog CMOS Integrated Circuits*. McGraw-Hill, 2000.

[42] W. von Ammon and H. Herzer, "The production and availability of high resistivity silicon for detector application," *Nuclear Instruments and Methods in Physics Research*, vol. 226, pp. 94–102, 1984.

[43] S. Holland, "Fabrication of detectors and transistors on high-resistivity silicon," *Nuclear Instruments and Methods in Physics Research, Section A*, vol. 275, pp. 537–541, 1989.

[44] S. Holland and H. Spieler, "A monolithically integrated detector-preamplifier on high-resistivity silicon," *IEEE Transactions on Nuclear Science*, vol. 37, no. 2, 1990.

[45] H. Spieler, *Semiconductor Detector Systems*. Oxford University Press, 2005.

[46] D. R. Schuette, "A mixed analog and digital pixel array detector for synchrotron imaging," Ph.D. dissertation, Cornell University, USA, 2008.

[47] C. Broennimann, E. F. Eikenberry, B. Henrich, R. Horisberger, G. Huelsen, E. Pohl, B. Schmitt, C. Shulze-Briese, M. Suzuki, T. Tomizaki, H. Toyokawa, and A. Wagner, "The PILATUS 1M detector," *Journal of Synchrotron Radiation*, vol. 13, pp. 120–130, 2006.

[48] B. Schmitt, "Jungfrau, Monch and Eiger: detector development at the Swiss Light Source," *Proceedings of SRI2013*, 2013.

[49] P. Trueb, B. A. Sobott, T. Loeliger, M. Schneebeli, M. Kobas, r. P. Rassool, D. J. Peake, and C. Broennimann, "Simulating the counting mechanism of PILATUS2 and PILATUS3 detectors for improved count rate corrections," *Journal of Physics: Conference Series*, vol. 425, pp. 062 002–1 – 062 002–4, 2013.

[50] R. Ballabriga, J. Alozy, G. Blaj, M. Campbell, M. Fiederle, E. Frojdh, E. H. M. Heijne, X. Llopart, M. Pichotka, S. Procz, L. Tlustos, and W. Wong, "The Medipix3RX: a high resolution, zero dead-time pixel detector readout chip allowing spectroscopic imaging," *Journal of Instrumentation*, vol. 8, pp. C02 016–1 – C02 016–15, 2013.

[51] B. Henrich, J. Becker, R. Dinapoli, P. Goettlicher, H. Graafsma, H. Hirsemann, R. Klanner, H. Krueger, R. Mazzocco, A. Mozzanica, H. Perrey, G. Potdevin, B. Schmitt, X. Shi, A. K. Srivastava, U. Trunk, and C. Youngman, "The Adaptive Gain Integrating Pixel Detector AGIPD: a detector for the European XFEL," *Nuclear Instruments and Methods in Physics Research, Section A*, vol. 633, pp. S11–S14, 2011.

[52] S. L. Barna, M. W. Tate, S. M. Gruner, and E. F. Eikenberry, "Calibration procedures for charge-coupled device x-ray detectors," *Review of Scientific Instruments*, vol. 70, no. 7, pp. 2927–2934, 1999.

[53] K. S. Green, H. T. Philipp, M. W. Tate, J. T. Weiss, and S. M. Gruner, "Calibration and post-processing for photon-integrating pixel array detectors," *Journal of Physics Conference Series*, vol. 425, p. 062009, 2013.

[54] P. Kraft, A. Bergamaschi, C. Broennimann, R. Dinapoli, E. F. Eikenberry, B. Henrich, I. Johnson, A. Mozzanica, Schlepütz, P. R. Willmott, and B. Schmitt, "Performance of single-photon-counting PILATUS detector modules," *Journal of Synchrotron Radiation*, vol. 16, pp. 369–375, 2009.

[55] S. E. Reichenbach, S. K. Park, and R. Narayanswamy, "Characterizing digital image acquisition devices," *Optical Engineering*, vol. 30, no. 2, pp. 170–177, 1991.

[56] S. T. Kelly, J. C. Trenkle, L. J. Koerner, S. C. Barron, N. Walker, P. O. Pouliquen, M. W. Tate, S. M. Gruner, E. M. Dufresne, T. P. Weihs, and T. Hufnagel, "Fast x-ray microdiffraction techniques for studying irreversible transformations in materials," *Jounral of Synchrotron Radiation*, vol. 18, pp. 464–474, 2011.

[57] A. Vacchi, A. Castoldi, S. Chinnici, E. Gatti, A. Longoni, F. Palma, M. Sampietro, P. Rehak, and J. Kemmer, "Performance of the UA6 large-area silicon drift chamber prototype," *Nuclear Instruments and Methods in Physics Research Section A*, vol. 306, pp. 187–193, 1991.

[58] D. Nouais, M. Bondila, V. Bonvicini, P. Cerello, E. Crescio, P. Giubellino, R. Hernandez-Montoya, A. Kolojvari, L. M. Montaño, B. S. Nilsen, C. Peimonte, A. Rashevsky, F. Tosello, A. Vacchi, and W. R., "Correction of dopant concentration fluctuation effects in silicon drift detectors," *Nuclear Instruments and Methods in Physics Research Section A*, pp. 222–225, 2001.

[59] E. Crescio, M. Bondila, P. Cerello, P. Giubellino, A. Kolozhvari, S. Kouchpil, G. Mazza, L. M. Montaño, D. Nouais, S. Piano, C. Piemonte, A. Rashevsky,

L. Riccati, A. Rivetti, F. Tosello, A. Vacchi, and R. Wheadon, "Results from beam tests of large area silicon drift detectors," *Nuclear Instruments and Methods in Physics Research Section A*, vol. 539, pp. 250–261, 2005.

[60] G. Batigne, S. Beolé, E. Biolcati, E. Crescio, D. Falchieri, G. Mazza, F. Prino, A. Rashevsky, L. Riccati, A. Rivetti, S. Senyukov, and L. Toscano, "Characterization of the ALICE silicon drift detectors using an infrared laser," *Journal of Instrumentation*, vol. 3, p. P06004, 2008.

[61] L. Tlustos, "Performance and limitations of high granularity single photon processing x-ray imaging detectors," Ph.D. dissertation, Technischen Universit at Wien, Austria, 2005.

[62] I. V. Kotov, A. I. Kotov, J. Frank, P. Kubanek, P. O'Connor, V. Radeka, and P. Takacs, "Lateral diffusion estimation in fully depleted thick CCD using flat field image analysis," *Nuclear Instruments and Methods in Physics Research Section A*, vol. 652, pp. 524–527, 2011.

[63] M. W. Tate, E. F. Eikenberry, S. L. Barna, M. E. Wall, J. L. Lowrance., and S. M. Gruner, "A large-format high-resolution area x-ray detector based on a fiber-otically bonded charge-coupled device (CCD)," *Journal of Applied Crystallography*, vol. 28, pp. 196–205, 1995.

[64] K. Giewekemeyer, H. T. Philipp, R. N. Wilke, A. Aquila, M. Osterhoff, M. Tate, K. S. Shanks, S. M. Gruner, and A. P. Mancuso, "High dynamic range coherent diffractive imaging: ptychography using the Mixed-Mode Pixel Array Detector," In preparation.

[65] H. T. Philipp, K. Ayyer, M. W. Tate, V. Elser, and S. M. Gruner, "Recovering structure from many low-information 2-D images of randomly-oriented samples," *Journal of Physics: Conference Series*, vol. 425, pp. 192 016–1–192 016–4, 2013.

[66] R. Ballabriga, M. Campbell, E. H. M. Heijne, X. Llopart, and L. Tlustos, "The Medipix3 prototype, a pixel readout chip working in single photon counting mode with improved spectrometric performance," *IEEE Transactions on Nuclear Science*, vol. 54, no. 5, pp. 1824–1829, 2007.

[67] P. Denes, D. Doering, H. A. Padmore, J.-P. Walder, and J. Weizeorick, "A fast, direct x-ray detection charge-coupled device," *Review of Scientific Instruments*, vol. 80, pp. 083 302–1–083 302–5, 2009.

[68] A. Kiyomichi, A. Amselem, T. Hironon, T. Ohata, R. Tanaka, and M. Yamaga, "Development of image data acquisition system for 2D detector at SACLA," *Proc. ICALEPCS2011.*, pp. 947–949., 2011.

[69] K. S. Green, D. M. E. Szebenyi, K. Boggs, R. Bredthauer, M. W. Tate, and S. M. Gruner, "A prototype direct-detection CCD for protein crystallography," *Journal of Applied Crystallography*, vol. 46, pp. 1038–1048, 2013.

[70] D. W. Cooke and B. L. Bennett, "Long-lived luminescence from commonly used Apiezon compounds," *Journal of Luminescence*, vol. 65, pp. 283–288, 1996.

[71] T.-P. Ko, J. Day, A. Greenwood, and A. McPherson, "Structures of three crystal forms of the sweet protein thaumatin," *Acta Crystallographica Section D*, vol. 50, pp. 831–825, 1994.

[72] R. Huang and D. H. Bilderback, "Single-bounce monocapillaries for focusing synchrotron radiation: modeling, measurements and theoretical limits," *Journal of Synchrotron Radiation*, vol. 13, pp. 74–84, 2006.

[73] A. G. W. Leslie and H. R. Powell, *Evolving Methods for Macromolecular Crystallography*. Springer, 2007, vol. 245, pp. 41–51.

[74] P. R. Evans, "Scaling and assessment of data quality," *Acta Crystallographica Section D*, vol. 62, pp. 72–82, 2006.

[75] Chapman, H. N., et al., "Femtosecond X-ray protein nanocrystallography," *Nature*, vol. 470, pp. 73–78, 2011.

[76] A. J. Malkin and R. E. Thorne, "Growth and disorder of macromolecular crystals: insights from atomic force microscopy and x-ray diffraction studies," *Methods*, vol. 34, pp. 273–299, 2004.

[77] R. Dinapoli, A. Bergamaschi, B. Henrich, R. Horisberger, I. Johnson, A. Mozzanica, E. Schmid, B. Schmitt, A. Schreiber, X. Shi, and G. Theidel, "EIGER: next generation single photon counting detector for x-ray applications," *Nuclear Instruments and Methods in Physics Research A*, vol. 650, pp. 79–83, 2011.

[78] C. Canali, G. Majni, R. Minder, and G. Ottaviani, "Electron and hole drift velocity measurements in silicon and their empirical relation to electric

field and temperature," *IEEE Transactions on electron devices*, vol. 22, no. 11, pp. 1045–1047, 1975.